

Readout circuits for hot-wire carbon dioxide sensors in CMOS technology

Cai, Zeyu

DOI

[10.4233/uuid:aaf9a28c-0926-41ab-a125-72f59d7937fe](https://doi.org/10.4233/uuid:aaf9a28c-0926-41ab-a125-72f59d7937fe)

Publication date

2020

Document Version

Final published version

Citation (APA)

Cai, Z. (2020). *Readout circuits for hot-wire carbon dioxide sensors in CMOS technology*. [Dissertation (TU Delft), Delft University of Technology]. <https://doi.org/10.4233/uuid:aaf9a28c-0926-41ab-a125-72f59d7937fe>

Important note

To cite this publication, please use the final published version (if applicable).
Please check the document version above.

Copyright

Other than for strictly personal use, it is not permitted to download, forward or distribute the text or part of it, without the consent of the author(s) and/or copyright holder(s), unless the work is under an open content license such as Creative Commons.

Takedown policy

Please contact us and provide details if you believe this document breaches copyrights.
We will remove access to the work immediately and investigate your claim.

READOUT CIRCUITS FOR HOT-WIRE CARBON DIOXIDE SENSORS IN CMOS TECHNOLOGY

Zeyu Cai

Readout Circuits for Hot-Wire Carbon Dioxide Sensors in CMOS Technology

Dissertation

for the purpose of obtaining the degree of doctor

at Delft University of Technology

by the authority of the Rector Magnificus Prof.dr.ir. T.H.J.J. van der Hagen

Chair of the Board for Doctorates

to be defended publicly on

Monday 23, March 2020 at

12:30 o'clock

by

Zeyu CAI

Master of Science in Electronics, The University of Edinburgh, UK

born in Nei Mongol, P.R. China

This dissertation has been approved by the promotor.

Composition of the doctoral committee:

Rector Magnificus,	chairperson
Dr. ir. M.A.P. Pertijs	Delft University of Technology, promotor
Prof. dr. K.A.A. Makinwa	Delft University of Technology, promotor

Independent members:

Prof. dr. ir. W.A. Serdijn	Delft University of Technology
Prof. dr. R.K. Henderson	The University of Edinburgh
Prof. dr. ing. L.C.N. de Vreede	Delft University of Technology
Dr. ir. P.J.A. Harpe	Eindhoven University of Technology
Dr. ir. R.H.M. van Veldhoven	NXP Semiconductors, The Netherlands

This work was supported by NXP Semiconductors, The Netherlands, and by ams AG, The Netherlands.

Printed by Proefschrift Maken | www.proefschriftmaken.nl

ISBN: 978-94-6380-676-3

Copyright © 2020 by Zeyu CAI

All rights reserved. No part of this publication may be reproduced or distributed in any form or by any other means, or stored in a database or retrieval system, without the prior written permission of the author.

Printed in The Netherlands

For Zhuoling

TABLE OF CONTENTS

TABLE OF FIGURES.....	I
LIST OF ABBREVIATIONS	V
1 INTRODUCTION.....	1
1.1 Background to the Problem.....	1
1.2 Literature Review	3
1.3 Organization of the Thesis.....	10
References.....	11
2 SYSTEM-LEVEL ANALYSIS OF THERMAL-CONDUCTIVITY-BASED SENSING.....	13
2.1 Operating Principle.....	13
2.2 System-Level Modeling	17
2.3 Design Challenges and Solutions	20
References.....	23
3 RATIOMETRIC AMPLITUDE-DOMAIN READOUT.....	25
3.1 Introduction	25
3.2 Operating Principle.....	27
3.2.1 Thermal Resistance Measurement using a Resistive Transducer ...	27
3.2.2 Ratiometric Thermal Resistance Measurement	30
3.2.3 Ratiometric Readout with Transducer Pairs	31
3.3 Circuit Implementation.....	32
3.3.1 Charge-Balancing Incremental Delta-Sigma Modulator	32
3.3.2 Switched-Capacitor Circuit in Temperature Mode.....	34
3.3.3 Switched-Capacitor Circuit in Power Mode.....	35
3.3.4 Dynamically-Matched Current Sources	36
3.3.5 Current-Trimming DACs	37

3.4	Experimental Results and Discussion.....	38
3.4.1	Electrical measurements.....	39
3.4.2	CO ₂ measurements	44
3.5	Conclusions	50
	References.....	51
4	ALGORITHMIC AMPLITUDE-DOMAIN READOUT	53
4.1	Introduction	53
4.2	Operating Principle.....	56
4.2.1	Algorithmic Resistance and Power Measurement.....	56
4.2.2	An Algorithmic Bandgap Voltage Reference.....	58
4.2.3	Algorithmic Temperature Measurement.....	60
4.2.4	Compensation of BJT Non-Idealities	61
4.3	Circuit Implementation.....	63
4.3.1	Circuit Implementation of the Transducer Front-End	64
4.3.2	Circuit Implementation of the BJT Front-End.....	66
4.4	Experimental Results and Discussion.....	67
4.4.1	Voltage Reference	69
4.4.2	Temperature Measurement.....	72
4.4.3	Resistance Measurement	73
4.4.4	Power Measurement	76
4.4.5	Equivalent Error in Thermal Resistance.....	78
4.5	Conclusions	78
	References.....	79
5	TIME-DOMAIN READOUT	81
5.1	Introduction	81
5.2	Operating Principle.....	82
5.2.1	Time-Domain Thermal-Conductivity Sensing.....	82
5.2.2	Phase-Domain Delta-Sigma Modulator.....	84
5.3	Circuit Implementation.....	85

5.3.1	Front-End Dynamic Range Reduction Technique.....	85
5.3.2	Current Trimming DACs.....	87
5.3.3	Phase-Domain Delta-Sigma Modulator.....	90
5.3.4	Noise Analysis.....	91
5.4	Experimental Results and Discussion.....	93
5.5	Conclusions	99
	References.....	99
6	CONCLUSIONS	101
6.1	Main Contributions.....	101
6.2	Main Findings.....	102
6.3	Future Work.....	104
	References.....	107
	SUMMARY	109
	SAMENVATTING.....	115
	LIST OF PUBLICATIONS.....	121
	ACKNOWLEDGMENT	123
	ABOUT THE AUTHOR.....	125

TABLE OF FIGURES

Figure 1.1. CO ₂ sensing based on non-dispersive infrared absorption (NDIR).....	3
Figure 1.2. Electrochemical CO ₂ sensing using solid electrolyte.....	4
Figure 1.3. Thermal-conductivity-based CO ₂ sensing.....	5
Figure 1.4. The freestanding resistive transducer in CMOS technology by an etching step.....	7
Figure 1.5. Organization of the thesis.....	10
Figure 2.1. Thermal conduction of a resistive heater placed in ambient air.....	14
Figure 2.2. Influences of environmental variations on the TC of air (data from transducer characterization).....	16
Figure 2.3. Electrical and thermal behavior of the TC-based transducer.	17
Figure 2.4. Equivalent circuit model for the TC-based CO ₂ sensor.	19
Figure 2.5. Typical outputs of the model with step-wise changes in CO ₂ concentrations.....	19
Figure 2.6. Cross-sectional view of the CO ₂ transducer.....	20
Figure 2.7. System-level architecture of the ratiometric approach.....	21
Figure 2.8. System-level architecture of the algorithmic approach.	22
Figure 2.9. System-level architecture of the time-domain approach.....	23
Figure 3.1. Steady-state thermal resistance measurement principle; (a) cross-sectional view of a suspended hot-wire resistive transducer and its heat-loss paths and (b) the equivalent model in both electrical and thermal domains.	28
Figure 3.2. (a) CO ₂ -sensitive and (b) reference transducer alternately biased at two different current levels.....	29
Figure 3.3. Block diagram of the ratiometric thermal-conductivity sensor readout with transducer pairs for baseline-resistance cancellation.....	31
Figure 3.4. Simplified circuit diagram of the switched-capacitor delta-sigma modulator in both temperature and power modes.	33
Figure 3.5. Dynamically-matched current sources and associated timing diagram (same algorithm applies to the current sources for the reference transducers).....	36
Figure 3.6. Circuit diagram of the current sources with a 6-bit current trimming DAC (LSB current = 0.5% × I _c ; the current sources as well as the current trimming	

TABLE OF FIGURES

DAC for the reference transducers are identical, not shown here; cascode transistors omitted for simplicity)..... 37

Figure 3.7. (a) Layout plot, (b) micrograph of the integrated readout circuit and (c) micrograph of a CMOS-compatible tungsten-wire transducer (using Kelvin connections, two wide tracks for current driving and two narrow tracks for voltage sensing)..... 39

Figure 3.8. Measured current ratios of the dynamically-matched current sources on 4 samples of the chip (initial mismatch is about 0.2%; after DEM the inaccuracies are -0.01%, 0.02%, -0.02% and -0.03% respectively)..... 40

Figure 3.9. Equivalent CO₂ resolution (1σ) derived from the standard deviation of the measured thermal-resistance ratio at ambient conditions (solid curves) and at different controlled CO₂ levels, using the first version (single-sampling) and the second version (double-sampling) of the readout circuit in combination with Figaro micro-heaters, along with the calculated resolution of the double-sampling scheme. 41

Figure 3.10. Variations in temperature, power and thermal-resistance ratios between the sensitive and reference transducers as a function of the bias current at ‘cold’ state (I_c). 42

Figure 3.11. Temperature, power, thermal-resistance ratios and the (peak-peak) voltage at the output of the integrator as a function of the current trimming level (in LSB steps of the trimming DAC). 43

Figure 3.12. Thermal-resistance ratio measured using the first version of the readout circuit with a 70 s measurement time, in combination with tungsten-wire transducers, for step-wise changing CO₂ concentration, without (a) and with (b) compensation for temperature and pressure cross-sensitivity, along with CO₂ concentration measured using an accurate reference NDIR sensor..... 45

Figure 3.13. Thermal-resistance ratio measured using the first (a) and second (b) version of the readout circuit, both with a 30 s measurement time, in combination with Figaro TGS 8100 transducers, with compensation for temperature and pressure cross-sensitivity, for step-wise changing CO₂ concentration, along with CO₂ concentration measured using an accurate reference NDIR sensor. 47

Figure 3.14. Feedback loop in the heating of the TC-based transducer. 48

Figure 4.1. Transducer front-end for resistance and power measurement..... 56

Figure 4.2. BJT front-end for algorithmic voltage measurement. 58

Figure 4.3. Temperature dependency of the key voltages for constructing a bandgap reference..... 59

Figure 4.4. (a) BJT front-end with series resistance R_s and leakage current I_{leak} ; (b) temperature errors due to I_{leak} ; (c) temperature errors due to R_s 62

Figure 4.5. Block diagram of the entire readout circuit (on-chip and off-chip).	63
Figure 4.6. Circuit diagram of the transducer front-end.	64
Figure 4.7. Schematic of the operational transconductance amplifier (OTA) used in both bandgap core and transducer front-end.	65
Figure 4.8. Circuit diagram of the proposed bandgap core including bias generation.	66
Figure 4.9. DEM algorithm ($p = 3$ current sources are selected in this example). .	67
Figure 4.10. Chip layout and micrograph.	68
Figure 4.11. Experimental setup.	69
Figure 4.12. Measured voltage error of the transducer by the algorithmic reference voltage (compared with the measurements by the multimeter).	70
Figure 4.13. Algorithmic reference voltage (a) without and with compensation and correction for series resistance and leakage; (b) with compensation and correction for series resistance and leakage as well as curvature.	71
Figure 4.14. Measured temperature error of the algorithmic temperature sensor (a) without and (b) with correction for leakage and series resistance.	72
Figure 4.15. Measured resistance error of a precision resistor as a function of temperature; (a) without calibration; (b) with calibration and correction at one-temperature point (27°C).	74
Figure 4.16. Measured resistance error of the Pt100 sensor resistor as a function of temperature; (a) with calibration and correction at one-temperature point (27°C); (b) with calibration and correction at two-temperature points (27°C and 100°C).	75
Figure 4.17. Measured power error as a function of temperature; (a) without calibration; (b) with 1-point calibration and correction of the resistance measurement; (c) with 2-point calibration and correction of the resistance measurement.	77
Figure 5.1. Transient thermal-resistance (thermal delay) measurement principle.	83
Figure 5.2. (a) Phase detection by means of synchronous detection. (b) Phase detection using a delta-sigma feedback loop.	84
Figure 5.3. Sensing the temperature-induced resistance changes using (a) current modulation, (b) differential sensing, and (c) baseline cancellation.	86
Figure 5.4. Current trimming DACs to compensate for the mismatch between the resistive transducers as well as the poly resistors (one of the total three DACs is shown as example).	88
Figure 5.5. Procedure to find the proper settings for the current trimming DACs.	89

TABLE OF FIGURES

Figure 5.6. Circuit diagram of the proposed readout circuit.....	90
Figure 5.7. Micrograph of the readout circuit and the transducer.	93
Figure 5.8. Measured spectrum of the bitstream (FFT of 2^{14} points).	94
Figure 5.9. Measured resolution (standard deviation of 20 consecutive measurements) and energy per measurement as a function of OSR.....	95
Figure 5.10. Measured phase shift as a function of the drive frequency.	96
Figure 5.11. Relative changes in the decimated results as well as in power consumption as a function of drive current.	96
Figure 5.12. Transient CO ₂ response of the CO ₂ sensor and an NDIR-based reference sensor (K30).	98
Table 1.1. Thermal conductivities (k) of some gases at 0 °C and 25 °C (pressure = 1013 mbar).....	6
Table 1.2. Performance of the prior TC-based CO ₂ sensors.....	6
Table 2.1. Cross-sensitivities to ambient variables and the requirements for the ambient sensors	16
Table 3.1. Performance of the proposed sensor compared to the prior art.....	49
Table 4.1. Performance Summary	78
Table 5.1. Performance summary and benchmarking	98

LIST OF ABBREVIATIONS

AC	Alternating Current
ADC	Analog-to-Digital Converter
ASHRAE	American Society of Heating, Refrigerating and Air-conditioning Engineers
BJT	Bipolar Junction Transistor
CMOS	Complementary Metal Oxide Semiconductor
CO₂	Carbon Dioxide
CTAT	Complementary To Absolute Temperature
DAC	Digital-to-Analog Converter
dB	Decibel
DC	Direct Current
DCV	Demand-Controlled Ventilation
DEM	Dynamic Element Matching
DIL	Dual-In-Line Package
DR	Dynamic Range
DUT	Device Under Test
ENOB	Effective Number of Bits
FPGA	Field-Programmable Gate Array
HABA	Home And Building Automation
IAQ	Indoor Air Quality
IC	Integrated Circuit
INL	Integral Non-Linearity
IoT	Internet of Things
IR	Infrared

LIST OF ABBREVIATIONS

LSB	Least Significant Bit
MEMS	Microelectromechanical System
MOSFET	Metal Oxide Semiconductor Field Effect Transistor
MUX	Multiplexer
NASICON	Sodium Super Ionic Conductor ($\text{Na}_3\text{Zr}_2\text{Si}_2\text{PO}_{12}$)
NDIR	Non-Dispersive Infrared Absorption
NMOS	N-type Metal Oxide Semiconductor
OSR	Oversampling Ratio
OTA	Operational Transconductance Amplifier
PCB	Printed Circuit Board
PDAΣM	Phase-Domain Delta-Sigma Modulator
PMOS	P-type Metal Oxide Semiconductor
ppm	Parts Per Million
PTAT	Proportional To Absolute Temperature
RH	Relative Humidity
TC	Thermal Conductivity
TCR	Temperature Coefficient of Resistance
XOR	Exclusive OR
$\Delta\Sigma$	Delta-Sigma

Chapter 1

INTRODUCTION

This thesis discusses the advantages and limitations of the carbon dioxide (CO₂) sensors based on thermal conductivity (TC) measurement, and describes how they can be implemented and subsequently read out using standard integrated circuit (IC) technology.

This chapter is organized into three sections. The first describes the background of the problem that motivated the work done in this thesis—the lack of cost effective and energy efficient CO₂ sensors for air-quality monitoring in home and building automation. The second is a literature review of various existing methods of sensing CO₂, which reveals that the transducers needed for thermal-conductivity-based CO₂ sensors can be realized in standard IC technology, thus enabling a significant reduction in their cost and size. The limitations of prior thermal-conductivity-based sensors are then discussed, and three readout approaches are proposed to address them. Finally, the organization of the thesis is presented.

1.1 Background to the Problem

The expansion of the Internet of Things (IoT) is generating new applications and increasing the level of automation and intelligence of existing environmental control systems. For example, IoT technologies have enabled the next-generation of home and building automation (HABA) systems which are incorporated in *Smart Building* designs [1]. The HABA systems rely on the integration of all kinds of environmental sensors (e.g., temperature, humidity, light, gas) to accurately monitor and automatically adjust real-time ambient conditions, targeting optimal occupant satisfaction and productivity with the best energy efficiency.

Indoor air quality (IAQ) is closely related to the health and productivity of a building's occupants, and thus is an essential metric of Smart Buildings. As the occupancy of a building increases, human-related pollutants, such as bacteria,

INTRODUCTION

molds, and volatile organic compounds increase, posing an increased risk for the health of the occupants. As a by-product of human respiration, CO₂ concentration also increases with occupancy. Recent research indicates that elevated CO₂ levels impair human productivity [2]. Therefore, CO₂ concentration is an important parameter for assessing indoor air quality. Integrating accurate CO₂ sensors into the ventilation systems of smart buildings will enable Demand-Controlled Ventilation (DCV), which will be more effective than ventilation systems that operate constantly or are based on prediction. DCV systems work harder when occupancy increases, and less when it decreases, resulting in significant energy savings. Analysis shows that the application of CO₂-based DCV systems results in substantial decreases in energy consumption, and in most cases, leads to significant reductions in the corresponding annual energy load, which ranges from 10% to 80% depending on the space type, climate, occupancy schedule, and ventilation strategy [3].

The existing CO₂ sensors using non-dispersive infrared absorption (NDIR) [4] or solid-state electrolytes [5] approaches are however, bulky and expensive. Furthermore, their power consumption typically exceeds what is needed in battery-powered wireless sensor nodes for HABA systems. Sensors based on solid-state electrolytes also rely on electrochemical reactions, which limits the long-term stability of the sensors and requires frequent recalibrations. Given such limitations, this project aims to propose an alternative sensing solution that not only meets the resolution requirement, but is also cost-effective and energy efficient; suitable for HABA application.

In the following section, the three main CO₂ sensing methods will be reviewed— (1) NDIR, (2) Electrochemical, and (3) Thermal-conductivity-based.

1.2 Literature Review

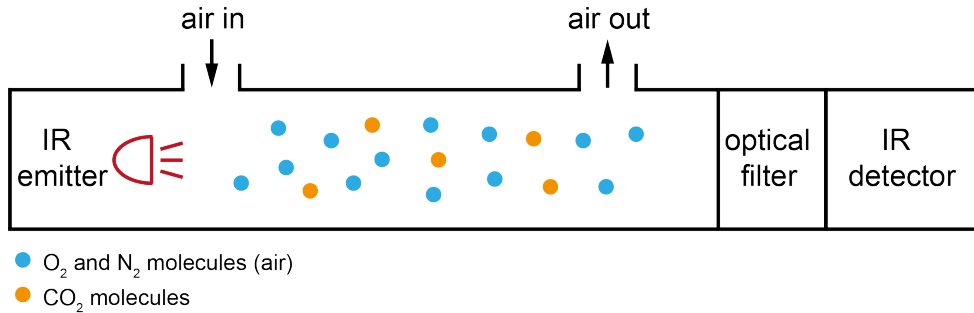


Figure 1.1. CO_2 sensing based on non-dispersive infrared absorption (NDIR)

Since the 1980s, the development and application of CO_2 sensors has been the subject of much industrial research and development [6]. Initially, CO_2 sensors were mainly based on non-dispersive infrared absorption (NDIR). The simplified operation of an NDIR sensor is shown in Figure 1.1. It is based on the fact that gas molecules absorb infrared (IR) light at certain wavelengths (e.g., $4.26\ \mu\text{m}$ for CO_2), and that the amount of absorption is proportional to the concentration of the gas [4][7]. Thus, by measuring the difference between the amount of IR radiation generated by the emitter and that received by the detector, CO_2 level can be calculated. NDIR-based CO_2 sensing has several advantages. Firstly, it is an intrinsically selective method, as the absorption wavelength is unique for CO_2 . Secondly, the amount of absorbed IR light is proportional to the amount of CO_2 in the sensing path. Thus, the sensitivity can be adjusted by changing the effective length of the IR light tube [8]. Thirdly, NDIR-based CO_2 sensors have good long-term stability. This is an important advantage as it reduces the cost of maintenance or replacement, especially when a large number of sensors are needed as in a HABA system. However, such sensors are expensive and difficult to miniaturize because of the long optical path required (i.e., typically $> 100\ \text{mm}$). In addition, their power consumption is rather high (typically $> 100\ \text{mW}$) [4][7]. Recently, efforts have been made to realize IR emitters in semiconductor technology [9]. Micro-hotplate IR emitters realized with MEMS technology have been reported [10]. These show improvements in reliability, response time, and physical size compared with traditional micro-bulb-based IR emitters. However, there is still

INTRODUCTION

significant room for improvement; low-cost, low-power, miniaturized optical CO₂ sensors are yet developed.

Electrochemical CO₂ sensors using solid-state electrolyte technology emerged later than NDIR CO₂ sensors [6]. Sensors based on solid-state electrolytes exploit the electrochemical reaction between CO₂ and specific compounds, generating an electromotive force (emf) that is a function of CO₂ concentration [11][12][13], as shown in Figure 1.2. These sensors commonly use the compound Na₃Zr₂Si₂PO₁₂ (NASICON) as the solid electrolyte and use two electrodes, of which the CO₂-sensing electrode is pasted with lithium carbonate. CO₂ reacts with the carbonate at the sensing electrode, and the (lithium) cations are replaced by sodium ions (in NASICON) which drift to the reference electrode, resulting in a CO₂-sensitive emf between the electrodes [11]. Sensors based on solid-state electrolytes are generally less expensive than optical sensors. However, their accuracy and long-term stability are usually inferior to that of their NDIR counterparts, and they usually need to operate at an elevated temperature.

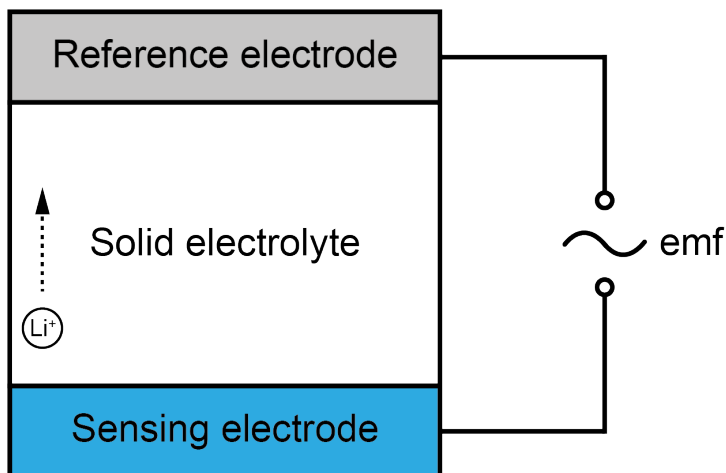


Figure 1.2. Electrochemical CO₂ sensing using solid electrolyte

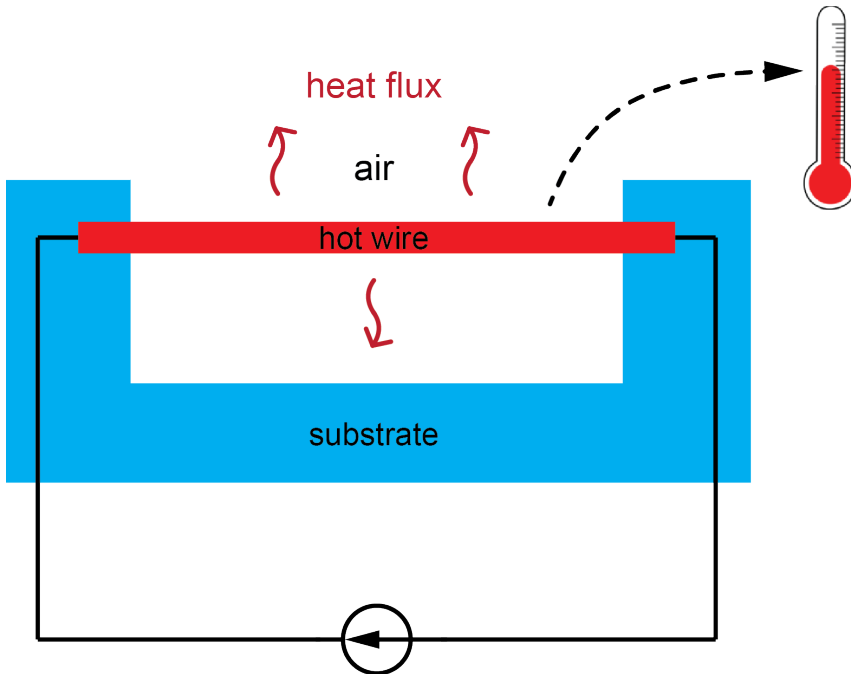


Figure 1.3. Thermal-conductivity-based CO₂ sensing

Another way of measuring CO₂ concentration is by measuring the thermal conductivity of air [14]. This exploits the fact that the thermal conductivity of different gases varies significantly. Since this is a fundamental property of each type of gas, changes in the composition of a gas mixture will manifest themselves in changes in its thermal conductivity, and thus in the temperature of a hot-wire transducer, as shown in Figure 1.3.

Table 1.1 shows the thermal conductivities (k) of some common gases. As shown in Table 1.1, compared to other gases such as hydrogen and helium, the thermal conductivity of CO₂ is much closer to that of air. This poses a challenge in realizing high-resolution CO₂ sensors, as the resulting changes in k can be very small (e.g., a 100-ppm change in CO₂ concentration will only result in a 37-ppm change in the TC of air). In addition, the thermal conductivity of air is also a parameter sensitive to environmental factors, such as ambient temperature, humidity and pressure, the impact of which also poses a challenge to the accurate measurement of the CO₂ concentration (as will be detailed in Chapter 2). Thus, thermal conductivity sensors have traditionally been restricted to measuring the concentration of hydrogen or helium in the air [15]. It is only in recent years that

INTRODUCTION

thermal-conductivity-based sensors with CO₂ resolution below the percentage range have appeared in literature and in industry [16][17][18]. The performance of these sensors is summarized in Table 1.2.

Table 1.1. Thermal conductivities (k) of some gases at 0 °C and 25 °C (pressure = 1013 mbar)

Gas type	k (0 °C) [mW/K·m]	k (25 °C) [mW/K·m]
Air (typical)	24.0	26.0
Carbon dioxide	14.0	16.4
Water vapor	16	19.9
Nitrogen	24.0	25.7
Oxygen	25.0	26.2
Helium	144.0	151.0
Hydrogen	174.0	180.0

Table 1.2. Performance of the prior TC-based CO₂ sensors

Parameter	[16]	[17]	[18]
Method	TC	TC	TC
Technology	MEMS	MEMS	MEMS
On-chip readout	No	No	No
Supply voltage	-	-	5 V
Power	3 mW	7 mW	100 mW
Measurement time	60 s	-	1 s
Energy per measurement	180 mJ	-	100 mJ
CO ₂ resolution (1σ)	456 ppm	<1%	1000 ppm

For use in air quality monitoring, the performances of these sensors falls short in three respects. Firstly, their CO₂ resolution is insufficient. According to ASHRAE (the American Society of Heating, Refrigerating and Air-conditioning Engineers), the suggested indoor CO₂ concentration should be below 5000 ppm [19]. However, adverse effects on productivity have been reported for average CO₂ concentrations as low as 1000 ppm. As such, to effectively monitor indoor CO₂ concentrations, much lower CO₂ sensing resolution is required, for example, 100 ppm. Secondly, the energy consumption of these sensors is too high for HABA application. Lastly, these sensors do not have co-integrated readout electronics. This means that they are not only bulky, they are also expensive solutions.

Given the existing shortcomings, TC-based CO₂ sensors have the potential to address the issues of NDIR or electrochemical CO₂ sensors. To measure the thermal conductivity of air, a resistive heater with defined thermal properties is needed, and this can be realized in Complementary Metal Oxide Semiconductor (CMOS) technology, in which standard methods of realizing metal or polysilicon resistors already exist [20]. For higher thermal resistance (thus higher sensitivity), the resistive transducer can be released by an additional etching step, as shown in Figure 1.4.

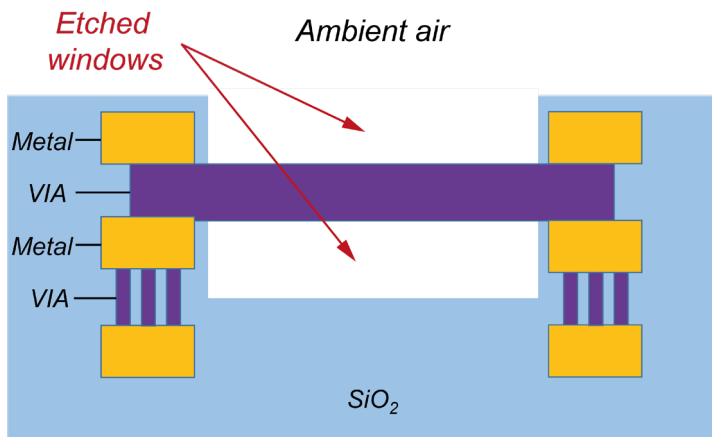


Figure 1.4. The freestanding resistive transducer in CMOS technology by an etching step

The compatibility of TC-based sensors with standard CMOS processes should result in low-cost and miniaturized systems [21]. Their power consumption will be

INTRODUCTION

dominated by the power needed to heat the transducer, but this is relatively low compared to the power consumed by an IR source. However, because of the very small signals involved, measuring indoor CO₂ levels with a 100-ppm level resolution represents a significant challenge for TC-based sensors [16]. In addition, TC sensing inherently means sensing power and temperature, and on-chip references for power and temperature are not sufficiently stable for CO₂ measurement at this level. Temperature compensation and trimming are thus required.

To address these challenges, three different solutions are proposed in this thesis:

- Solution I: use a TC reference in the form of a “capped” transducer (i.e., its TC is independent of the changes of CO₂ in ambient air) and measure TC ratiometrically;
- Solution II: use an algorithmic architecture to enable accurate temperature compensation and trimming;
- Solution III: measure the thermal time constant (instead of the TC) relative to a time reference (clock), which essentially means that the combination of the thermal capacitance of the sensor and the time reference is now used as an indirect TC reference.

Three different readout architectures based on these solutions have been designed and realized. Their effectiveness has been confirmed by the realization of prototype sensors in a standard 0.16 μm CMOS technology, in which the tungsten VIA layer is used to realize a CMOS-compatible hotwire transducer. Note that the presented readout architectures are not limited to this specific technology. Since Tungsten is a standard material in most of the CMOS processes, the designs can be migrated to other standard processes [22].

The first approach is based on a ratiometric TC measurement, which obviates the need for an accurate power reference by using a second transducer (isolated from the air) as a thermal-conductivity reference. The readout circuit ratiometrically digitizes the sensor’s thermal conductivity relative to that of the reference, without relying on accurate voltage, power, or temperature references. To prove the concept with simplified post processing, the sensor and reference transducers are kept on separate dice and the sealing of the reference transducer is done at package-level (Chapter 3).

In contrast with the ratiometric approach, the second approach does not employ a capped reference transducer, but instead, explores the use of accurate

temperature compensation and correction. The idea is to successively measure the voltage, current and ambient temperature of a resistive transducer, and then to process them algorithmically in a digital backend to obtain “temperature-compensated” readings of resistance and power dissipation, from which the thermal conductivity for CO₂ sensing can be calculated (Chapter 4).

The third approach moves the measurement from the amplitude domain to the time domain. The required reference is also in the time domain, which typically incurs no additional cost since a stable clock is available in most electronic systems. The design uses a high-resolution phase-domain delta-sigma ($\Delta\Sigma$) modulator to sense the thermal time constant of a hot-wire transducer and applies differential sensing and baseline compensation to reduce the required dynamic range (Chapter 5).

To obtain an accurate CO₂ measurement, the impact of humidity and temperature also needs to be quantified and removed. For the CO₂ measurements described in this thesis, we monitored the temperature (T) and relative humidity (RH) using a separate humidity sensor and used this information to obtain the final results. Although we conceptually demonstrate the calibration and correction process for cross-sensitivities to humidity, temperature, and pressure, it should be noted that the implementation of a complete cross-sensitivity compensation scheme is quite complex and requires much more thought and design work. It is beyond the scope of this thesis, but would be a necessary step in the development of a commercial product.

1.3 Organization of the Thesis

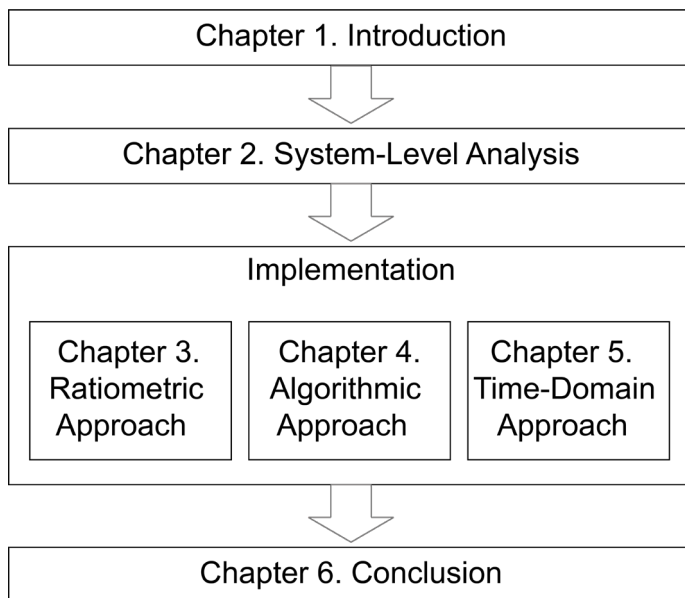


Figure 1.5. Organization of the thesis

The organization of the thesis is shown in Figure 1.5. Chapter 2 provides a system-level analysis of thermal-conductivity-based sensing, including the operating principle of thermal-conductivity-based sensors, an electro-thermal model for system-level analysis, and qualitative and quantitative explanations of the challenges in designing a thermal-conductivity-based CO₂ sensor. Chapter 3 introduces the first approach to solve the reference problem, which is a prototype sensor based on ratiometric thermal-conductivity measurement. Chapter 4 presents a different approach to solve the problem by using an algorithmic readout to accurately measure the absolute values of the resistance, temperature, and power dissipation of a resistive transducer. Chapter 5 presents the third approach, which involves measuring the transient thermal delay of a hot-wire using a phase-domain $\Delta\Sigma$ modulator, instead of by measuring thermal conductivity in the amplitude domain. The thesis ends with conclusions and a summary in Chapter 6. Suggestions for future work are also provided.

References

- [1] Zanella, N. Bui, A. Castellani, L. Vangelista and M. Zorzi, “Internet of Things for Smart Cities,” in *IEEE Internet of Things Journal*, vol. 1, no. 1, pp. 22-32, Feb. 2014.
- [2] U. Satish et al., “Is CO₂ an indoor pollutant? Direct effects of low-to-moderate CO₂ concentrations on human decision-making performance,” *Environ. Health Perspect.*, vol. 120, no. 12, pp. 1671–1677, 2014.
- [3] A. K. Persily, A. Musser, S. J. Emmerich, and M. Taylor, “Simulations of Indoor Air Quality and Ventilation Impacts of Demand Controlled Ventilation in Commercial and Institutional Buildings,” NISTIR 7042, National Institute of Standards and Technology, Aug. 2003.
- [4] SenseAir. SenseAir K30 Datasheet. [Online]. Available: <http://www.senseair.com/>.
- [5] FIGARO TGS4161 datasheet (REV: 12/05), FIGARO [Online]. Available: <http://www.figaro.co.jp/>.
- [6] S. J. Emmerich and A. K. Persily, “State-of-the-Art Review of CO₂ Demand Controlled Ventilation Technology and Application,” NISTIR 6729, National Institute of Standards and Technology.
- [7] SGX Sensortech. SGX IR11BD Datasheet. [Online]. Available: <http://www.sgxsensortech.com/>.
- [8] S. Yi, Y. Park, S. Han, N. Min, E. Kim, and T. Ahn, “Novel NDIR CO₂ sensor for indoor air quality monitoring,” in *Proc. IEEE Int. Conf. Solid-State Sens., Actuators Microsyst. (TRANSDUCERS)*, Jun. 2005, pp. 1211–1214.
- [9] S. Z. Ali, A. De Luca, R. Hopper, S. Boual, J. Gardner and F. Udrea, “A low-power, low-cost infra-red emitter in CMOS technology,” *IEEE Sensors J.*, vol. 15, no. 12, pp. 6775-6782, Dec. 2015.
- [10] T.A. Vincent, J.W. Gardner, “A low cost MEMS based NDIR system for the monitoring of carbon dioxide in breath analysis at ppm levels,” *Sens. and Actuators B, Chem.*, vol. 236, pp. 954-964, Nov. 2016.
- [11] K. Kaneyasu et al., “A carbon dioxide gas sensor based on solid electrolyte for air quality control,” *Sens. Actuators B, Chem.*, vol. 66, nos. 1–3, pp. 56–58, Jul. 2000.
- [12] W. Y. Chuang, C. C. Wu, S. S. Lu and C. T. Lin, “A printable conductive polymer CO₂ sensor with high selectivity to humidity,” in *Proc. IEEE Int. Conf. Solid-State Sens., Actuators Microsyst. (TRANSDUCERS)*, Jun. 2017, pp. 1501-1503.
- [13] L. Satyanarayana, W. S. Noh, G. H. Jin, W. Y. Lee and J. S. Park, “A potentiometric CO₂ sensor combined with composite metal oxide and DOP plasticizer operative at low temperature,” *IEEE Sensors J.*, vol. 8, no. 9, pp. 1565-1570, Sept. 2008.
- [14] N. B. Vargaftik, *Handbook of Thermal Conductivity of Liquids and Gases*, 1st ed. CRC Press, Boca Raton, 1993.

INTRODUCTION

- [15] I. Simon and M. Arndt, “Thermal and gas-sensing properties of a micromachined thermal conductivity sensor for the detection of hydrogen in automotive applications,” *Sens. Actuators A, Phys.*, vols. 97–98, pp. 104–108, Apr. 2002.
- [16] K. Kliche, G. Kattinger, S. Billat, L. Shen, S. Messner, and R. Zengerle, “Sensor for thermal gas analysis based on micromachined siliconmicrowires,” *IEEE Sensors J.*, vol. 13, no. 7, pp. 2626–2635, Jul. 2013.
- [17] K. Kliche, S. Billat, F. Hedrich, C. Ziegler, and R. Zengerle, “Sensor for gas analysis based on thermal conductivity, specific heat capacity and thermal diffusivity,” in *Proc. IEEE Int. Conf. MEMS*, Jan. 2011, pp. 1189–1192.
- [18] XEN-5310 datasheet. Xensor Integration [Online]. Available: <http://www.xensor.nl/>.
- [19] “Ventilation for Acceptable Indoor Air Quality,” ANSI/ASHRAE Standard 62.1, 2016.
- [20] A. Hastings, *The art of analog layout*. New Jersey: Prentice Hall, 2001.
- [21] H. Baltes, O. Paul and O. Brand, “Micromachined thermally based CMOS microsensors,” in *Proceedings of the IEEE*, vol. 86, no. 8, pp. 1660-1678, Aug. 1998.
- [22] M. Riverola et al., “Dynamic properties of three-terminal tungsten CMOS-NEM relays under nonlinear tapping mode,” *IEEE Sensors J.*, vol. 16, no. 13, pp. 5283-5291, Jul. 1, 2016.

Chapter 2

SYSTEM-LEVEL ANALYSIS OF THERMAL-CONDUCTIVITY-BASED SENSING

In this chapter, a system-level analysis of the operation of thermal-conductivity (TC)-based CO₂ sensors will be presented. This serves as the basis for the design and implementation of the readout circuits that will be detailed in the following chapters. To provide a system-level overview, the operating principle of TC-based sensors will be explained first, followed by the introduction of a simplified circuit model of their electrical and thermal behavior. System-level nonidealities and their impact can then be evaluated using this model. Finally, key challenges in the design of the readout circuit will be reviewed and a number of solutions will be proposed and discussed.

2.1 Operating Principle

Thermal conductivity (TC) quantifies the ability of a material to conduct heat [1]. Changes in the concentration of a gas in a mixture of gases with different TCs will result in changes in the overall TC. As a result, changes in TC can be used to quantify changes in gas concentration, provided that it is the sole varying parameter in the gas mixture [2]. This is applicable to the measurement of CO₂ concentration in ambient air at indoor conditions, where CO₂ concentration rises as a by-product of human respiration. Thus, CO₂ concentration can be used as an indicator of indoor air quality.

When a resistive heater is placed in ambient air, as shown in Figure 2.1, its temperature depends on the thermal resistance between it and ambient, indicated by the following expression:

$$T_{heater} = PR_{th} + T_{ambient} \quad (2.1)$$

where T_{heater} is the temperature of the heater, P is the power dissipated in the heater, R_{th} is the thermal resistance, and $T_{ambient}$ is the ambient temperature. It should be

noted that the thermal resistance R_{th} here refers to the net thermal resistance between the heater and its surroundings (i.e., ambient air, mechanical support, etc.), and it is only partially due to the conductive loss to the ambient air. This part is inversely proportional to the thermal conductivity of the air. Clearly, in order to determine changes in gas concentration through the thermal resistance R_{th} , the temperature rise of the heater relative to ambient and the power dissipation of the heater must be known. The accuracy with which these two parameters can be measured is directly related to the accuracy of the resulting gas concentration measurement. As will be discussed later in this chapter, this becomes the main challenge in making a CO₂ sensor in standard CMOS.

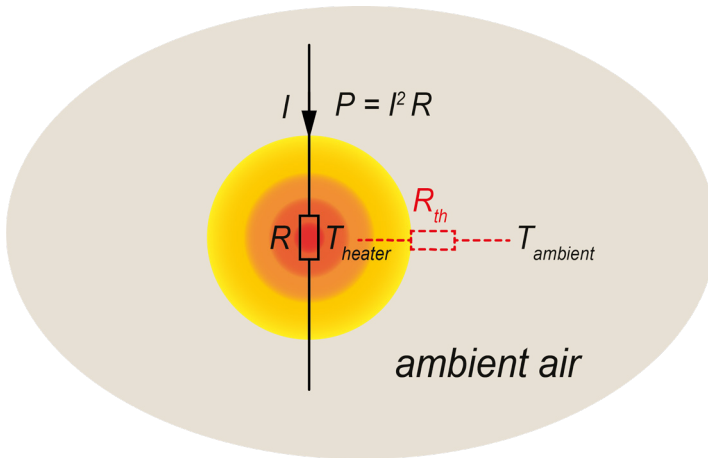


Figure 2.1. Thermal conduction of a resistive heater placed in ambient air.

One limitation of a TC-based gas sensor is that it cannot distinguish between different gases, as it only measures the overall TC of the gas mixture [1][2]. If another gas component, apart from the targeted gas in the gas mixture changes, a TC-based sensor will not be able to accurately determine the changes in the concentration of the targeted gas. This lack of selectivity must be taken into account when using TC-based sensors in specific applications. For determining the CO₂ concentration in indoor air, however, this lack of selectivity is not an issue since the composition of indoor air is relatively well-defined and the main source of dynamic variations are changes in CO₂ concentration due to exhalation [3].

TC-based gas sensors are also sensitive to environmental changes, such as ambient temperature, humidity, pressure, and flow [4][5][6]. This can be expressed as follows:

$$\Delta R_{th} = S_{CO_2} \cdot \Delta CO_2 + S_T \cdot \Delta T + S_{RH} \cdot \Delta RH + S_p \cdot \Delta p + S_F \cdot \Delta F \quad (2.2)$$

where ΔR_{th} is the change in thermal resistance, S_{CO_2} , S_T , S_{RH} , S_p , and S_F are the sensitivities to CO_2 , temperature, relative humidity (RH), pressure and flow, respectively. To determine the changes in thermal resistance due to CO_2 , changes due to temperature, humidity, pressure, and flow must be compensated for. The influence of such ambient variations on the thermal conductivity of air was quantified by characterizing a prototype transducer (a tungsten wire, realized in the VIA layer of a standard CMOS technology [7]). The experimental results have been expressed in terms of equivalent changes in CO_2 concentration, as illustrated in Figure 2.2. This can be used as a reference for the specifications of the auxiliary ambient sensors for cross-sensitivity compensation. The cross-sensitivities to ambient variations and the requirements for the ambient sensors are listed in Table 2.1 (the cross-sensitivity to flow is not included here, as this can be made negligible by using the appropriate packaging).

The errors due to cross-sensitivity can be compensated by integrating environmental sensors with the CO_2 sensor. The stability requirements shown in Table 2.1 are relatively high, but these are requirements for a limited range of variations under the indoor conditions. For instance, the range of indoor relative humidity in air-conditioned buildings is generally about 30-60%, and the indoor temperature range is generally about 10-40°C. A state-of-the-art CMOS temperature sensor achieves an inaccuracy of ± 60 mK over a temperature range from -55°C to +125°C [8]. Over the narrower indoor range, its inaccuracy can be reduced to about 10 mK, which is equivalent to 67 ppm CO_2 . Similarly, a state-of-the-art CMOS humidity sensor [9] can achieve an inaccuracy of less than 0.3% over the indoor range, which is equivalent to 120 ppm CO_2 . Therefore, the total impact on the CO_2 measurement accuracy due to the cross-sensitivity from temperature and humidity can be reduced to <200 ppm when compensated by CMOS-compatible sensors.

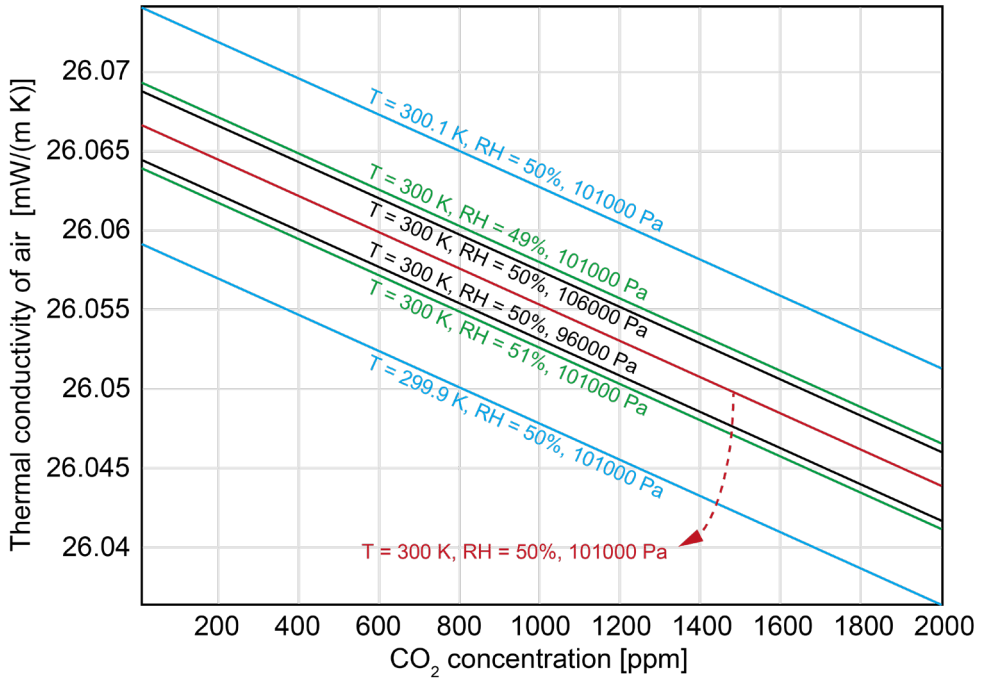


Figure 2.2. Influences of environmental variations on the TC of air (data from transducer characterization).

Table 2.1. Cross-sensitivities to ambient variables and the requirements for the ambient sensors

(Cross-) Sensitivity	Value	Stability requirement*
CO ₂ concentration S_{CO_2}	0.4 ppm / ppm	
Temperature S_T	2.7 ppm / mK	< 30 mK
Relative Humidity S_{RH}	160 ppm / % RH	< 0.5%
Pressure S_p	800 ppm / mbar	< 0.1 mbar

*for reduction of errors due to cross-sensitivity to < 200 ppm CO₂

2.2 System-Level Modeling

Consider the case in which a resistor is used as the heater. If the resistor is biased by a constant current source, then due to Joule heating, its temperature increases. Assuming the resistance depends on temperature, this will lead to a change in its electrical resistance. This can be expressed as:

$$R = R_0 \cdot (1 + \alpha(T - T_0)) = R_0 + R_0 \cdot \alpha \cdot P \cdot R_{th} \quad (2.3)$$

where R is the electrical resistance at temperature T , R_0 is the nominal resistance at temperature T_0 , α is the temperature coefficient of the resistance, P is the power dissipation in the resistor, and R_{th} is the thermal resistance between the resistor and its surroundings. This means that a resistive heater with a defined temperature dependency can also be used as a temperature sensor in order to measure changes in thermal resistance [4]. The electrical and thermal behavior of such a resistive transducer is shown in Figure 2.3. A thermal capacitor C_{th} is also included in order to model its transient behavior. The thermal time constant τ_{th} determines the rate of heating (i.e. the rate of change of temperature).

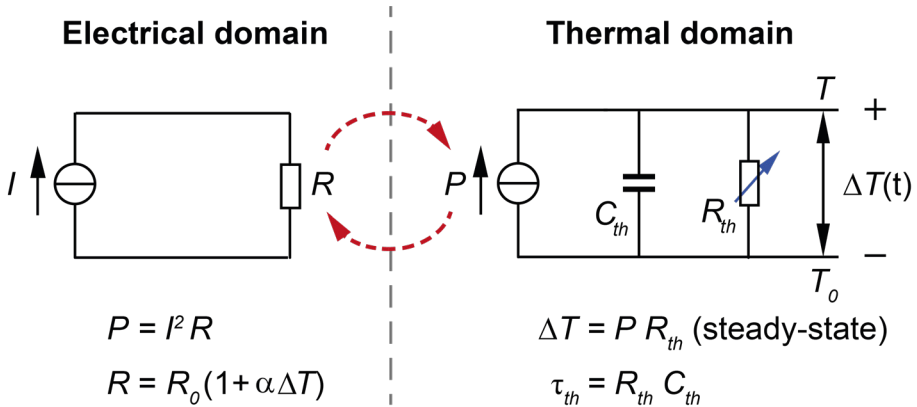


Figure 2.3. Electrical and thermal behavior of the TC-based transducer.

To capture the interaction between the electrical and the thermal domains, an equivalent circuit model for a TC-based CO_2 sensor has been implemented, as shown in Figure 2.4. It is an exact implementation of the behavioral model shown in Figure 2.3., with the following input parameters:

- Bias current I [mA]
- Electrical baseline resistance R_0 [Ω]
- Temperature coefficient of the resistor α [K^{-1}]
- Ambient temperature T_0 [K]
- CO₂ concentration CO_2 [ppm]
- Thermal capacitance C_{th} [J/K]
- Thermal baseline resistance R_{th0} [K/W]
- Sensitivity to CO₂ concentration S_{CO_2} [K/W/ppm]

In this circuit model, the variables of Eq. 2.3 are represented either by voltage sources or current sources. The outputs of the model are the power dissipation P and temperature T of the transducer. In the electrical domain, the sensor is just a temperature-dependent resistor. This is modeled by a sensing resistor $R_1 = 1 \Omega$ (negligible compared to that of the transducer), which senses the bias current I , in series with a voltage-controlled resistor R_2 . The voltage-controlled resistor R_2 models the resistance of the sensor, which is equal to $R_0 (1 + \alpha(T - T_0))$. This equation is implemented by a multiplier *Mult1* driven by the voltage sources $V3$, $V4$, $V5$ and $V6$, which model I , R_0 , α , and T_0 , respectively. The voltages across R_1 and R_2 are applied to unity-gain voltage-controlled voltage sources $V1$ and $V2$, whose outputs model the current and voltage of the sensor resistor, respectively. These are then multiplied by *Mult2* (port C), to model the power dissipation (P) in the sensor.

As in Figure 2.3, power is modeled in the thermal domain as a voltage-controlled current source II (with a gain of minus one for correct polarity) whose control voltage is equal to the value of the power dissipation. The transducer's thermal capacitance is modeled by a capacitor C , and its thermal resistance is modelled by another voltage-controlled resistor R_3 , whose value is a combination of a baseline (R_{th0}) and a CO₂-dependent part ($S_{CO_2} * CO_2$ [ppm]), realized by voltage sources $V7$ and $V8$, respectively. The temperature T is obtained from the thermal-domain part of the circuit model (reference to ambient temperature T_0), representing the temperature of the TC sensor. With a first-order approximation of the electrical and thermal behavior, this circuit model can then be used for system-level analysis and to derive the specifications of the readout circuit. The output of the model for step-wise CO₂ inputs is shown in Figure 2.5.

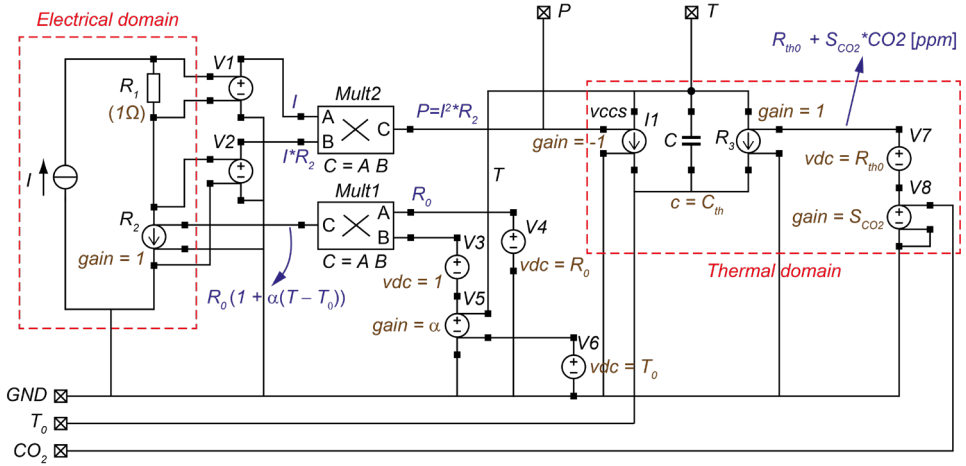


Figure 2.4. Equivalent circuit model for the TC-based CO₂ sensor.

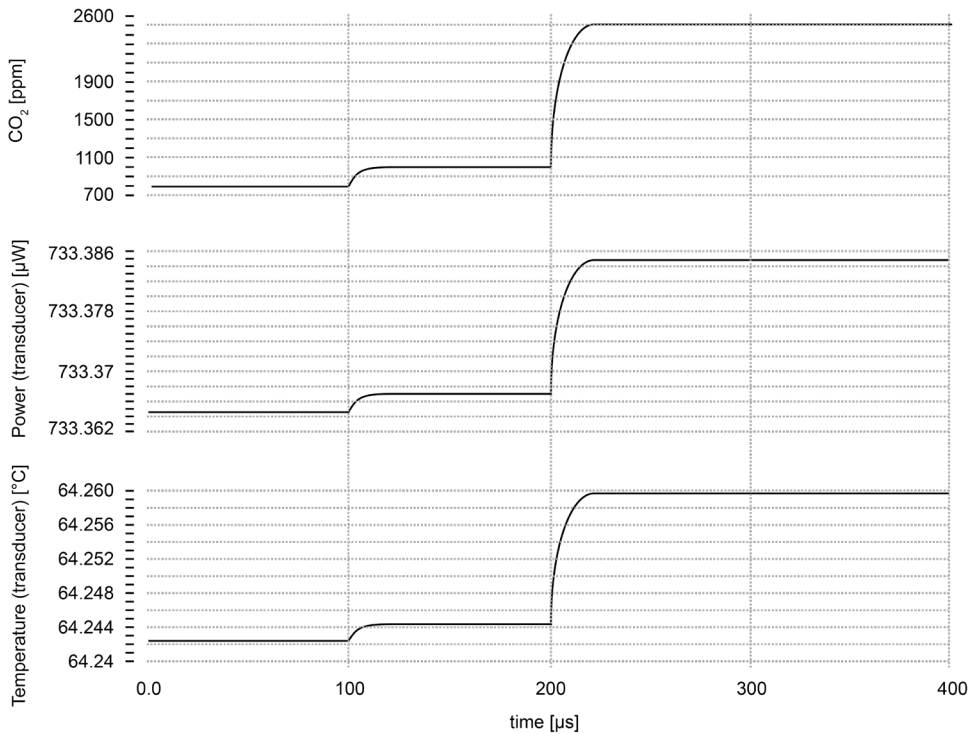


Figure 2.5. Typical outputs of the model with step-wise changes in CO₂ concentrations.

2.3 Design Challenges and Solutions

In this project, the resistive heater was realized in the (tungsten) VIA layer of a standard $0.16\ \mu\text{m}$ CMOS technology C14 at NXP Semiconductors, as shown in Figure 2.6 [7]. The nominal resistance R_0 is about $110\ \Omega$, and the temperature coefficient α is $0.0017/\text{K}$. By characterizing the transducer chips, the thermal resistance R_{th} of the tungsten transducer is found to be about $53500\ \text{K/W}$, and its sensitivity to CO_2 is about $0.013\ \text{K/W}$ per ppm CO_2 (i.e., about 50 ppm per 200 ppm change in CO_2 concentration). When biased with a DC current of $2.5\ \text{mA}$, this translates into a change of merely $1.5\ \mu\Omega$ per ppm change in CO_2 concentration [10]. For indoor air-quality sensing, CO_2 concentration needs to be measured with a resolution of 100 to 200 ppm in a full scale of up to 2500 ppm [11][12]. This translates into a resistance change of about $150\ \mu\Omega$ in a total resistance of $110\ \Omega$. This directly requires a resolution of >19.5 bits for the analog-to-digital converter (ADC) in the readout circuit, which, in turn, leads to challenging requirements in terms of noise and circuit performance.

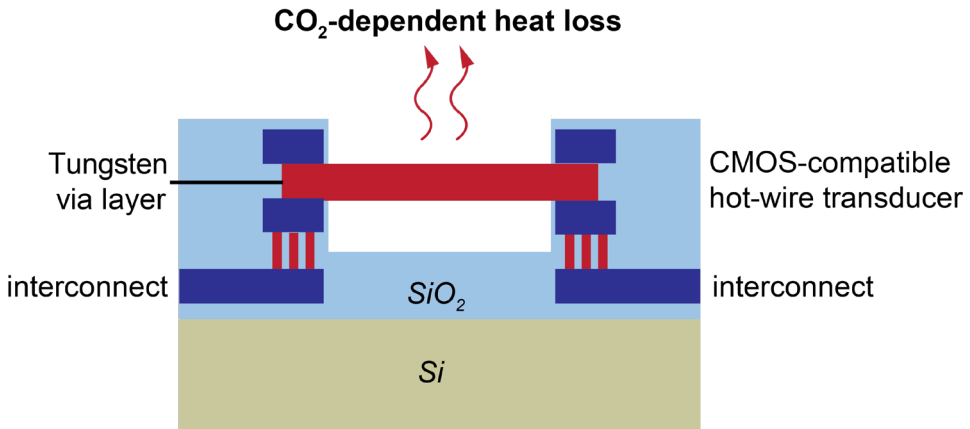


Figure 2.6. Cross-sectional view of the CO_2 transducer.

The low sensitivity of thermal resistance to CO_2 (i.e., about 50 ppm per 200 ppm change in CO_2 concentration) also poses a challenge in terms of the stability of the transducer's power dissipation. Equation (2.1) implies that the power dissipation should be known accurately, since any error in the power dissipation

leads to an equivalent error in the measured thermal resistance, and hence to an error in the detected CO₂ concentration. In order to measure a 200-ppm change in CO₂, errors in power dissipation should be less than 50 ppm, leading to a significant challenge in the design of the readout circuit.

In addition, since the TC-based sensor is also sensitive to ambient variations, auxiliary environmental sensors for cross-sensitivity compensation must also be included [4][5][7][10]. This will inevitably complicate the design of the entire sensor system and the implementation of the measurement setup.

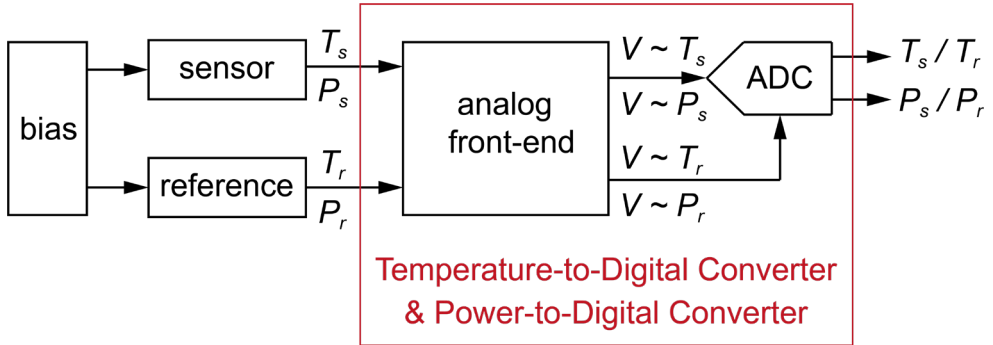


Figure 2.7. System-level architecture of the ratiometric approach.

These challenges have been taken into account in the design of the readout circuits that will be presented in this thesis. For use in the readout circuit, an incremental delta-sigma ($\Delta\Sigma$) ADC is a good candidate as it can trade resolution with conversion time [13]. This is particularly suitable for CO₂ sensing, as changes in the CO₂ concentration of indoor air are relatively slow [14]. To reduce the required dynamic range for the readout circuit, the constant baseline value of the resistor can be removed by circuit techniques.

To circumvent the stringent requirement on the stability of the transducer's power dissipation, as shown in Figure 2.7, the first prototype uses a ratiometric approach in which a reference transducer is biased by the same bias circuit as the sensor. The ratios of the temperature and power of the CO₂-sensing transducer (T_s , P_s) and those of the reference transducer (T_r , P_r) are measured by a reconfigurable physical-to-digital converter which can perform temperature-to-digital and power-to-digital conversions. As a result, the stability requirement in power dissipation is

translated into a matching requirement between the CO₂-sensing transducer and the reference transducer [4].

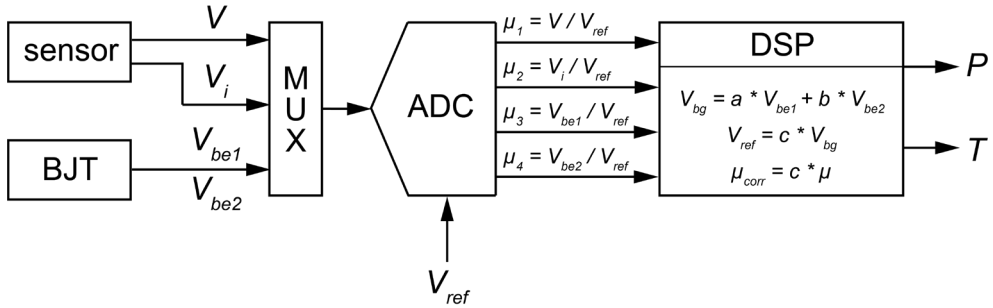


Figure 2.8. System-level architecture of the algorithmic approach.

The second prototype, as shown in Figure 2.8, enables accurate measurements of voltage and resistance (thus power) of the sensor and temperature by using a single shared high-resolution ADC. This is achieved by measuring a number of signals separately, including the voltage and current of the sensor (V and V_i), as well as the base-emitter voltages (V_{be1} and V_{be2}) of a substrate parasitic PNP transistor. The signal processing, including the construction of an accurate bandgap reference voltage V_{bg} , and the correction of ADC errors, can then be done entirely in the digital domain. This “algorithmic” architecture enables flexible temperature compensation and trimming, resulting in the accurate power (P) and temperature (T) measurements required for high-precision TC sensing.

The third prototype moves the measurement of thermal conductivity from the amplitude domain to the time domain [10], as shown in Figure 2.9. This replaces the power reference in the amplitude domain by a reference clock in the time domain, which may be more favorable in many ICs, thus simplifying the integration of the sensor to an existing system. The heating and sensing functions are both realized by the same transducer, which further simplifies the sensor system. This approach will be described in more detail in Chapter 5.

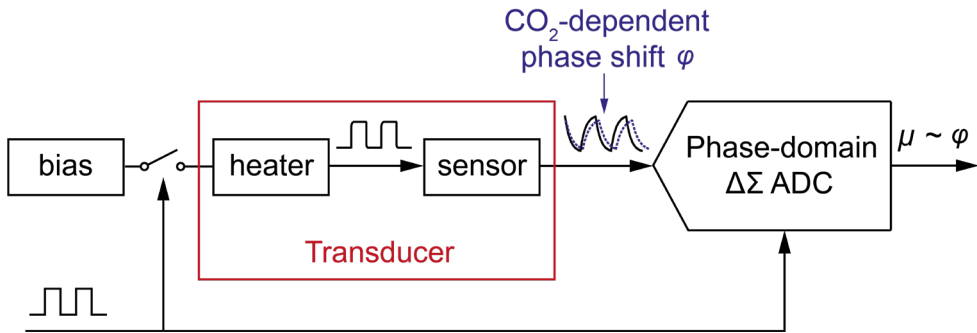


Figure 2.9. System-level architecture of the time-domain approach.

For cross-sensitivity compensation, additional temperature, humidity, pressure sensors have been included in the experiment to prove the concept [15][16]. The environmental sensors for cross-sensitivity compensation can eventually be integrated on-chip together with the CO₂ sensor in the next generation. The detailed design and measurement results of these prototype sensors will be covered in the following chapters.

References

- [1] W. M. Rohsenow, J. P. Hartnett and Y. I. Cho, Handbook of Heat Transfer, 3rd edition. New York. McGraw-Hill, 1998.
- [2] S. C. Terry, J. H. Jerman and J. B. Angell, "A gas chromatographic air analyzer fabricated on a silicon wafer," IEEE Trans. Electron Devices, vol. 26, no. 12, pp. 1880-1886, Dec 1979.
- [3] R. J. Heinsohn and J. M. Cimbala, Indoor Air Quality Engineering: Environmental Health and Control of Indoor Pollutants. New York, USA: CRC Press.
- [4] Z. Cai et al., "A ratiometric readout circuit for thermal-conductivity-based resistive CO₂ sensors," IEEE J. Solid-State Circuits, vol. 51, no. 10, pp. 2463-2474, Oct. 2016.
- [5] K. Kliche et al., "Sensor for thermal gas analysis based on micromachined silicon-microwires," IEEE Sensors J., vol. 13, no. 7, pp. 2626-2635, Jul. 2013.
- [6] G. de Graaf et al., "Micro thermal conductivity detector with flow compensation using a dual MEMS device," Sens. Actuators A: Phys., vol. 249, pp. 186-198, Oct. 2016.
- [7] Z. Cai et al., "An integrated carbon dioxide sensor based on ratiometric thermal-conductivity measurement," in Proc. IEEE Int. Conf. Solid-State Sens., Actuators Microsyst. (TRANSDUCERS), Jun. 2015, pp. 622-625.

- [8] B. Yousefzadeh, S. Heidary Shalmany and K. A. A. Makinwa, "A BJT-based temperature-to-digital converter with ± 60 mK (3σ) inaccuracy from -55 °C to $+125$ °C in $0.16\text{-}\mu\text{m}$ CMOS," *IEEE J. Solid-State Circuits*, vol. 52, no. 4, pp. 1044-1052, Apr. 2017.
- [9] Z. Tan, R. Daamen, A. Humbert, Y. V. Ponomarev, Y. Chae, and M. A. P. Pertijs, "A 1.2-V 8.3-nJ CMOS humidity sensor for RFID applications," *IEEE J. Solid-State Circuits*, vol. 48, no. 10, pp. 2469–2477, Oct. 2013.
- [10] Z. Cai et al., "A phase-domain readout circuit for a CMOS-compatible thermal-conductivity-based carbon dioxide sensor," in *Dig. Techn. Papers ISSCC Feb. 2018*, pp. 332-334.
- [11] N. Nassif, "A robust CO₂-based demand-controlled ventilation control strategy for multi-zone HVAC systems," *Energy and Buildings*, 45, pp. 72–81, 2012.
- [12] V. Congradac and F. Kulic, "HVAC system optimization with CO₂ concentration control using genetic algorithms," *Energy and Buildings*, 41, pp. 571–577, 2009.
- [13] J. Markus, J. Silva, and G. C. Temes, "Theory and applications of incremental $\Delta\Sigma$ converters," *IEEE Trans. Circuits Syst. I, Fundam. Theory Appl.*, vol. 51, no. 4, pp. 678–690, Apr. 2004.
- [14] S.J. Emmerich, A.K. Persily, "Literature review on CO₂-based demand-controlled ventilation," *ASHRAE Transaction*, vol. 103, pp. 229–243, 1997.
- [15] Sensirion SHT25 datasheet, Sensirion [Online]. Available: <http://www.sensirion.com/>.
- [16] NXP MPL3115A2 datasheet, NXP Semiconductors [Online]. Available: <http://www.nxp.com/>.

Chapter 3

RATIOMETRIC AMPLITUDE-DOMAIN READOUT

This chapter is based on the publication “A Ratiometric Readout Circuit for Thermal-Conductivity-Based Resistive CO₂ Sensors,” in IEEE Journal of Solid State Circuits, vol. 51, no. 10, pp. 2463-2474, Oct. 2016.

3.1 Introduction

As discussed in Chapter 1, gas sensors based on thermal-conductivity (TC) measurement rely on the fact that the heat loss of a suspended hot-wire depends on the composition of the surrounding gas. Changes in gas composition can therefore be detected via changes in the wire’s temperature. This principle forms the basis of low-cost sensors for the detection of gases such as Hydrogen and Helium, as the required heaters and sensors can be realized in IC technology [1][2]. However, realizing TC-based CO₂ sensors for monitoring indoor CO₂ levels is very challenging, as extremely small changes in thermal conductivity need to be measured. Based on the thermal conductivities of air and CO₂ at 25°C (26 mW/K·m and 16.4 mW/K·m, respectively), a 200 ppm change in CO₂ concentration causes sub-80 ppm changes in thermal conductivity, thus requiring a high-resolution temperature measurement, and, more critically, an extremely stable power reference (because any changes in heater power will lead to errors in the measured temperature and thus to errors in the measured thermal conductivity). As will be explained in Section 3.2, for our CO₂ sensor, a 50 ppm change of power corresponds to a 200 ppm error in CO₂ concentration. Unfortunately, the stability of on-chip power references is typically not better than 4000 ppm [4][5][6], which would be equivalent to a 1.6% error in CO₂ concentration. Prior TC-based CO₂ sensors employ expensive off-chip circuits to control the heating power [2][3]. In addition, such sensors typically employ micro-machined structures with separate transducers for heating and temperature sensing [7][8], requiring relatively

complex and costly processing steps. Using a suspended resistor as both a heating and sensing element significantly simplifies the fabrication process [9], but requires a readout circuit that is capable of accurately measuring both power dissipation and temperature.

This chapter presents an integrated readout circuit capable of measuring the power dissipated in a resistive transducer, as well as its temperature. It is designed for use with the CMOS-compatible tungsten-wire transducer reported in [9], but it has also been characterized in combination with a more robust commercial resistive micro-heater (Figaro TGS-8100 [10]) to evaluate the performance at power levels higher than those CMOS-compatible transducers can handle. To obviate the need to stabilize or accurately measure the transducer's power dissipation, we adopt an alternative approach in which a second transducer acts as a thermal-conductivity reference. Its thermal properties are similar to those of the sensor, but it is shielded from the ambient air by the appropriate packaging. Our readout circuit ratiometrically digitizes the sensor's thermal conductivity relative to that of the reference, without relying on accurate voltage, power or temperature references [11].

Measuring CO₂ variation through the change of the transducer's resistance is very challenging. Measurements of our tungsten-wire transducers show that a 200 ppm CO₂ variation causes a mere 0.3 mΩ variation in a baseline resistance of 110 Ω. The measurement can be relaxed by canceling the baseline resistance, as only the change in resistance is of interest. Many approaches have been reported to cancel baseline resistance [12][13][14][15]. They either rely on a 'dummy' passive element but assume negligible mismatch errors introduced by manufacturing tolerances [12][13], or require a dedicated calibration phase involving extra analog-to-digital conversion steps before measurements commence [14][15].

To cancel the baseline resistance, this work adopts a two-state measurement. The transducers in our self-referenced system are operated alternately in 'hot' and 'cold' states by switching their bias-current levels, allowing the change in resistance between the two states to be measured directly. To avoid imposing a challenging requirement on the dynamic range (DR) of the readout circuit due to the switching between 'hot' and 'cold' states, this chapter presents a novel structure employing pairs of dynamically-swapped transducers to cancel baseline resistance, thus enabling the accurate measurement of their resistance changes without increasing the DR requirement for the readout. In addition, dynamically-matched current sources are used to generate accurate current ratios for the 'hot' and 'cold' states, and the paired transducers are themselves periodically swapped to

cancel errors due to transducer mismatch. Lastly, current-trimming DACs are used to further suppress mismatch errors.

Experimental results from a prototype implemented in a standard 0.16 μm CMOS process demonstrate the effectiveness of these techniques. In combination with the tungsten-wire transducers, the readout circuit achieves 14-bit resolution in the measured thermal resistance ratio, which corresponds to 228 ppm in CO_2 resolution (1σ) in a 70 s measurement time, while consuming 11.2 mW from a 1.8 V supply. An improved version of the design, in combination with the commercial micro-heaters, achieves 202 ppm CO_2 resolution in a measurement time of 30 s for the same power consumption.

The chapter is organized as follows. In Section 3.2, the operating principle of TC-based gas sensors and the proposed ratiometric readout circuit is presented. Section 3.3 is devoted to the circuit implementation of the readout circuit, including a switched-capacitor delta-sigma ADC, dynamically-matched current sources, and current-trimming DACs. Experimental results and discussions are presented in Section 3.4, and the chapter concludes in Section 3.5.

3.2 Operating Principle

3.2.1 Thermal Resistance Measurement using a Resistive Transducer

A hot-wire transducer loses heat via two main paths, both of which can be modelled as thermal resistances. As shown in Figure 3.1: one resistance is to the surrounding air (R_{th_air}), while the other is to the substrate via the anchor points (R_{th_sub}). The transducer's temperature rise relative to its ambient (ΔT) caused by the power dissipated in the transducer (P) is directly proportional to the parallel combination R_{th} of R_{th_air} and R_{th_sub} :

$$\Delta T = P \times R_{th} = P \times (R_{th_air} \parallel R_{th_sub}) \quad (3.1)$$

Since the different components of air have different thermal conductivities, R_{th_air} is a function of gas composition, and hence ΔT can be used to determine the CO_2 concentration in air. Since CO_2 is a better thermal insulator than air, higher CO_2 concentrations will lead to (slightly) higher values of ΔT . To maximize sensitivity, the heat loss to the substrate must be minimized. This is typically done by using suspended transducers [1][8].

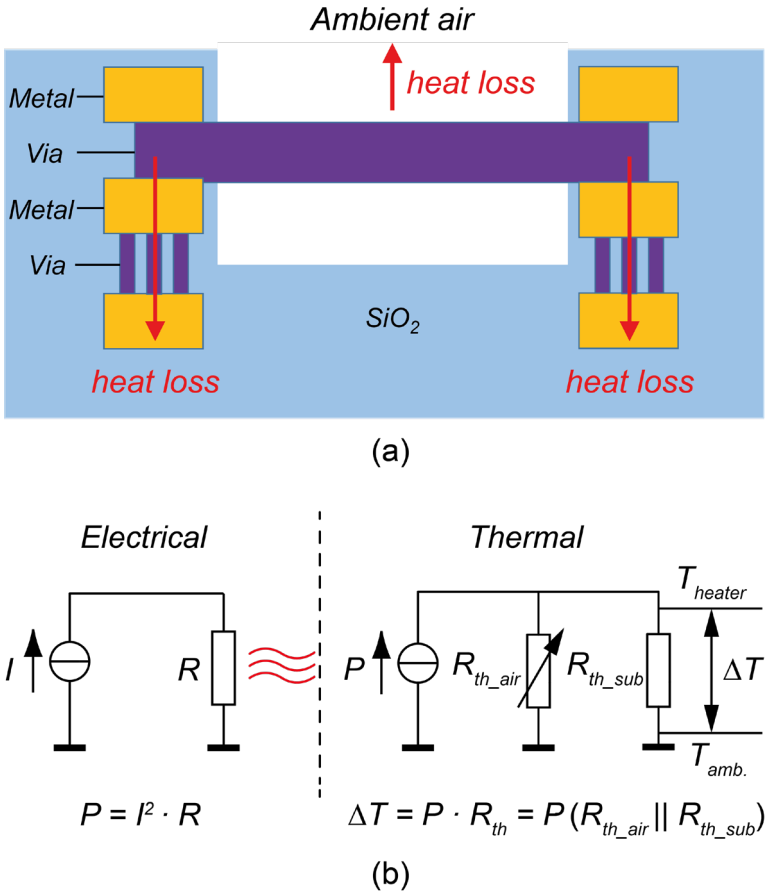


Figure 3.1. Steady-state thermal resistance measurement principle; (a) cross-sectional view of a suspended hot-wire resistive transducer and its heat-loss paths and (b) the equivalent model in both electrical and thermal domains.

While ΔT in (3.1) can be measured using a dedicated temperature sensor (e.g., thermopiles [2]), the use of the electrical resistance of the heater to measure its temperature greatly simplifies the fabrication process, allowing the tungsten via material of a CMOS metal stack to be used as a heater, as shown in Figure 3.1a [9]. Tungsten is preferred over aluminium as a heater for the following reasons. First, aluminium is more difficult to process due to stiction in the wet release etch step [16]. Second, the strength of an aluminium wire is lower due to its grainy structure. Lastly, aluminium is more susceptible to electromigration [17].

The resistance of a tungsten transducers can be approximated by a linear function of temperature:

$$R = R_0 \cdot (1 + \alpha \cdot (T - T_0)) \quad (3.2)$$

where R_0 is the nominal electrical resistance of the transducer at room temperature T_0 , and α its temperature coefficient. For our tungsten transducers, R_0 is 110 Ω and α is 0.0017/K. The nominal resistance R_0 is set by the aspect ratio of the resistor, and was designed to allow sufficient power to be dissipated in the resistor with the available supply voltages.

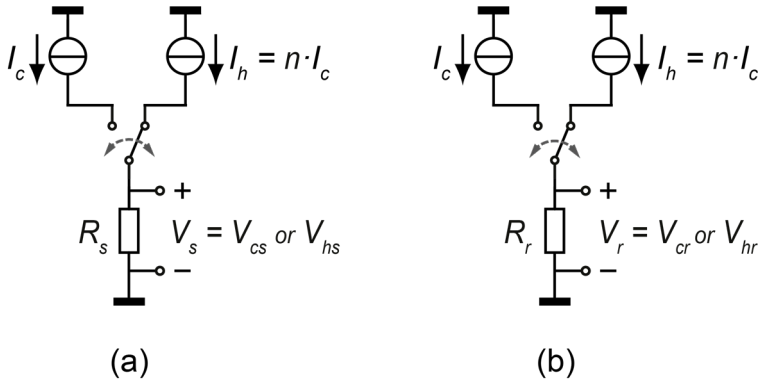


Figure 3.2. (a) CO_2 -sensitive and (b) reference transducer alternately biased at two different current levels.

To measure ΔT , the transducer is alternately biased at a low current I_c and a high current I_h (Figure 3.2a), corresponding to a ‘cold’ and a ‘hot’ state. The power dissipation in (3.1) then becomes the difference in power dissipation between these two states (ΔP), and R_{th} becomes:

$$R_{th} = \frac{\Delta T}{\Delta P} = \frac{T_h - T_c}{P_h - P_c} = \frac{R_h - R_c}{R_0 \alpha (I_h^2 R_h - I_c^2 R_c)} \quad (3.3)$$

In order to accurately measure R_{th} , both ΔT and ΔP need to be accurately measured. The nominal R_{th} of our tungsten transducer (at 400 ppm CO_2 and 25°C) is about 53,500 K/W. A change of 200 ppm CO_2 results in about 80 ppm change in the thermal resistance of air. For our transducers, the thermal resistance to the substrate (R_{th_sub}), which does not depend on the CO_2 concentration, is about two

times larger than the thermal resistance to the surrounding air (R_{th_air}). Since the measured thermal resistance R_{th} is the parallel combination of R_{th_sub} and R_{th_air} , the relative sensitivity of R_{th} to CO_2 is reduced by a factor 2/3 compared to that of R_{th_air} . Therefore, a CO_2 change of 200 ppm corresponds to a relative change of R_{th} of about 50 ppm. This implies that the power levels and temperature measurement should be stable to within ± 25 ppm, making the measurement very challenging.

3.2.2 Ratiometric Thermal Resistance Measurement

Instead of measuring the absolute thermal resistance of one transducer, measuring the thermal resistance of a CO_2 -sensitive transducer relative to that of a (CO_2 -insensitive) reference transducer greatly relaxes the power stability and temperature measurement requirements, as the absolute accuracy requirement is replaced by a matching requirement on the CO_2 -sensitive and reference transducers. The reference transducer is biased in the same way as the sensitive transducer (Figure 3.2b). Their thermal-resistance ratio can be derived from (3.3) and expressed as a multiplication of two ratios: the ratio of the temperature-difference of the sensitive transducer (ΔT_s) and the temperature-difference of the reference transducer (ΔT_r), and the ratio of their power differences ($\Delta P_r / \Delta P_s$):

$$\frac{R_{th,s}}{R_{th,r}} = \left(\frac{\Delta T_s}{\Delta T_r} \right) \left(\frac{\Delta P_r}{\Delta P_s} \right) = \left(\frac{R_{hs} - R_{cs}}{R_{hr} - R_{cr}} \right) \left(\frac{n^2 I_c^2 R_{hr} - I_c^2 R_{cr}}{n^2 I_c^2 R_{hs} - I_c^2 R_{cs}} \right) = \left(\frac{V_{hs} - nV_{cs}}{V_{hr} - nV_{cr}} \right) \left(\frac{nV_{hr} - V_{cr}}{nV_{hs} - V_{cs}} \right) \quad (3.4)$$

where $n = I_h / I_c$, $V_{hs} = n \cdot I_c \cdot R_{hs}$, $V_{cs} = I_c \cdot R_{cs}$, $V_{hr} = n \cdot I_c \cdot R_{hr}$, $V_{cr} = I_c \cdot R_{cr}$, and the transducers are assumed to have identical R_0 and α , which therefore cancel out. The last term in (3.4) shows that the thermal-resistance ratio can be written as a product of two voltage-difference ratios, which in this work are digitized sequentially by a dual-mode switched-capacitor incremental $\Delta\Sigma$ ADC and multiplied in the digital backend.

Note that, while the ratiometric measurement relaxes the power and temperature measurement requirements, calibration and correction will still be needed due to device-to-device variation of the thermal resistance of the transducers and of their sensitivity. This calibration will involve exposing the sensor to one or more well-defined CO_2 levels and measuring the ratiometric output. Also note that compensation for cross-sensitivity will be needed, since the transducers are also sensitive to e.g. temperature, humidity and pressure. This will involve co-integration of sensors for these parameters and correcting the output

based on their readings. The implementation of this cross-sensitivity compensation is beyond the scope of this thesis.

3.2.3 Ratiometric Readout with Transducer Pairs

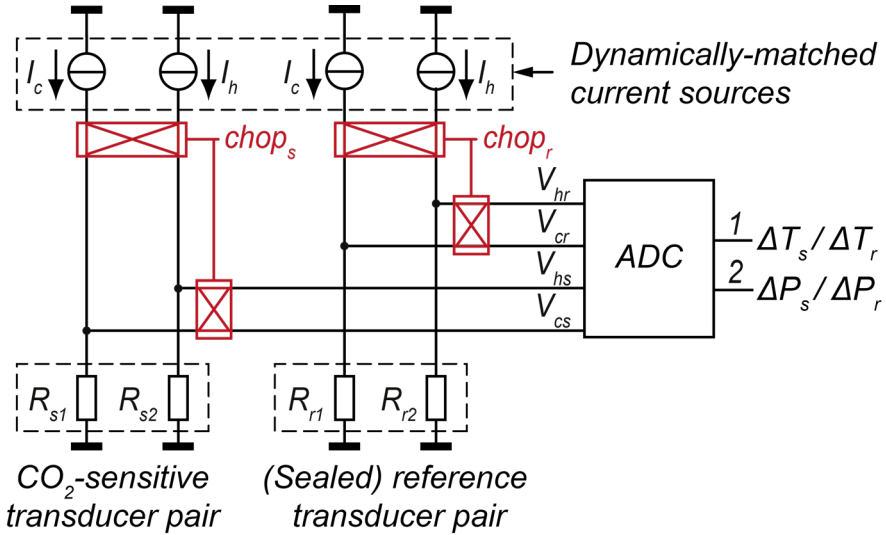


Figure 3.3. Block diagram of the ratiometric thermal-conductivity sensor readout with transducer pairs for baseline-resistance cancellation.

A challenge associated with the sequential readout of hot and cold states is that the voltage drop across the transducers varies significantly between the two states, which means that the following ADC must have a large dynamic range to avoid clipping. To relax the dynamic range, a pair of CO₂-sensitive transducers (R_{s1} , R_{s2}) and a pair of reference transducers (R_{r1} , R_{r2}) are used (Figure 3.3). Both reference transducers are isolated from the ambient air by package-level sealing. In each pair, the transducers are alternately biased at I_c and $I_h = n \cdot I_c$, generating simultaneously ‘hot’ and ‘cold’ voltages for both sensitive (V_{hs} , V_{cs}) and reference transducers (V_{hr} , V_{cr}). The current ratio n is chosen so as to optimize the signal-to-noise ratio (SNR). For a given power consumed in biasing the transducers, a smaller n gives a smaller signal amplitude, while a larger n reduces the current in the ‘cold’ state, and, as a result, increases the noise level associated with that state. Therefore, SNR degrades for small and large values of n , and an optimum can be found for which the SNR is maximized. A parametric simulation of our design shows that this optimum is

reached at a ratio of $n = 5$. The transducers in each pair are periodically swapped by the chopper switches around them, causing mismatches to be averaged out. To prevent the switching transients from affecting the measurement accuracy, a settling time is included after swapping during which the ADC does not sample the voltages across the transducers. Since the thermal time constant of the transducers is relatively long (measured to be about 40 μs for our tungsten-wire transducers), the swapping is done at a relatively low rate (approximately once every 24 ms) to prevent the accumulated thermal settling time from significantly adding to the total measurement time. The ‘hot’ and ‘cold’ voltages are simultaneously sampled by scaled switched-capacitor circuits and merged together, as will be detailed in Section 3.3. Note that, while package-level sealing of the reference transducers has been used for flexibility, a similar approach can be applied if the transducers are integrated on the same chip using wafer-level or chip-scale capping (see also Section 3.4.2).

3.3 Circuit Implementation

3.3.1 Charge-Balancing Incremental Delta-Sigma Modulator

To obtain a CO_2 -sensing resolution on the order of 200 ppm (corresponding to 50 ppm or 14.3 bits resolution in the R_{th} ratio), we digitize each of the voltage ratios in (3.4) with a resolution better than 15.3 bits (equivalent to 100 ppm CO_2). Since CO_2 concentration tends to change relatively slowly, an incremental delta-sigma ADC is a suitable choice. A charge-balancing delta-sigma modulator is used that operates in two modes: temperature mode and power mode. First, in temperature mode, it produces a bitstream bs proportional to the first voltage ratio in (3.4), which equals the temperature-difference ratio. Then, in power mode, it produces a bitstream proportional to the second voltage ratio in (3.4), which equals the power-difference ratio. These bitstreams are decimated by an (off-chip) decimation filter, and the results are multiplied in the digital domain to obtain the thermal-resistance ratio.

Figure 3.4 shows the switched-capacitor implementation of the modulator. It consists of a switched-capacitor integrator, with four parallel input branches connecting to the four transducers, and a clocked comparator. To ensure accurate settling and to prevent integrator leakage from limiting the resolution, the integrator employs a gain-booster folded-cascode OTA with a unity-gain

bandwidth of about 2.5 MHz and a nominal DC gain of 140 dB [18]. The comparator is a latched comparator using a pre-amplifier to reduce kick-back effect of the positive-feedback latch [19]. Minimum-size switches ($W/L = 0.8 \mu\text{m}/0.16 \mu\text{m}$) are used to minimize charge injection.

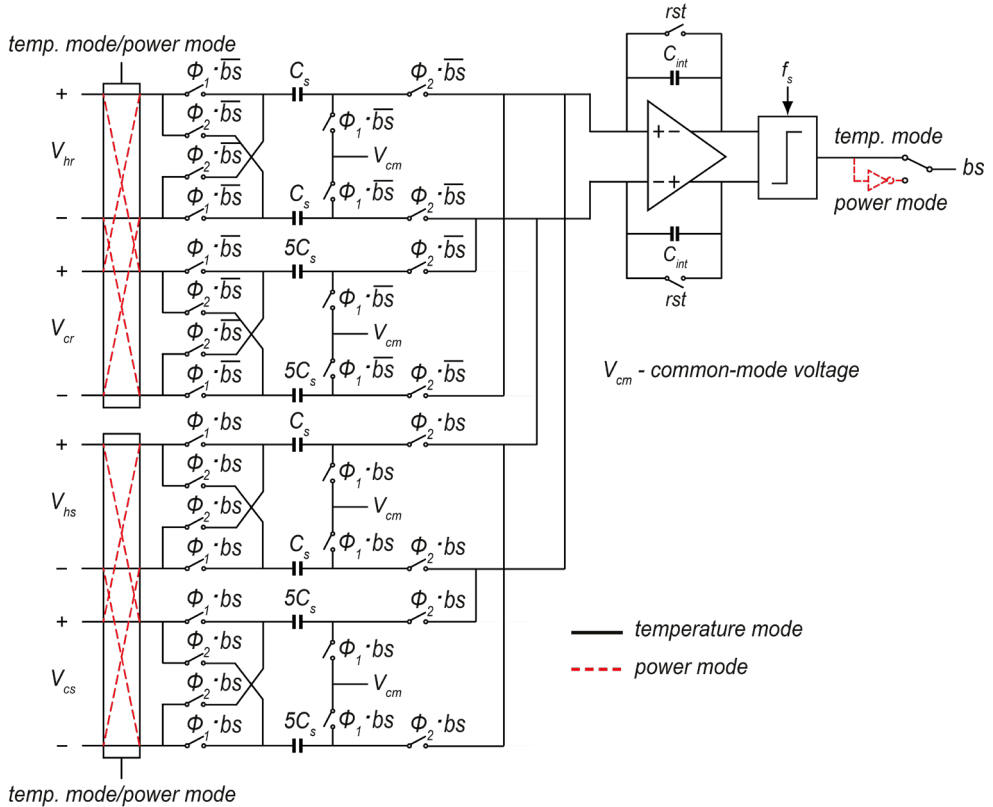


Figure 3.4. Simplified circuit diagram of the switched-capacitor delta-sigma modulator in both temperature and power modes.

To quantify the impact of various error sources from the circuit (e.g., the error in current ratio and the mismatch in capacitors) on the ADC's output, we designed a behavioral model for the transducer and the ADC based on a Verilog-A script and analyzed the sensitivities of the measured R_{th} ratio to all the error sources. This analysis shows that accurate matching is required for the capacitors, and especially for the current sources in order to obtain accurate CO_2 measurements.

3.3.2 Switched-Capacitor Circuit in Temperature Mode

In temperature mode, the first voltage ratio in (3.4), which equals the temperature-difference ratio, is digitized. As shown in Figure 3.4, the ‘hot’ voltages (V_{hs} , V_{hr}) are sampled by unit capacitors C_s while the ‘cold’ voltages (V_{cs} , V_{cr}) are sampled by scaled capacitors $5C_s$, to generate the ‘ n ’ factor in (3.4). The inaccuracy of this capacitor ratio gives an error in the measurement of the thermal-resistance ratio. Simulations show that 0.1% mismatch leads to a measurement error equivalent to 200 ppm CO₂. An accurate common-centroid layout is used to achieve this level of matching. Each transducer uses Kelvin connections to eliminate errors due to contact resistance. During phase ϕ_1 , the ‘hot’ and ‘cold’ voltages are connected to one plate of the sampling capacitors, while their other plate is connected to the common-mode voltage V_{cm} . During the subsequent phase ϕ_2 , the connections to the transducers are reversed, while the capacitors are connected to the virtual ground of the integrator. This double-sampling scheme causes a charge proportional to two times the voltage drop across the transducer to be transferred to the integrator. The switches associated with the pair of sensitive transducers are gated by the bitstream, causing a charge proportional to $(V_{hs} - nV_{cs})$ to be integrated when $b_S = 1$. Similarly, the switches associated with the reference transducers are gated by the inverse of the bitstream, causing a charge proportional to $-(V_{hr} - nV_{cr})$ to be integrated when $b_S = 0$. Since the negative feedback in the modulator ensures that the average integrated charge tends to zero, the following charge-balancing equation applies:

$$\mu(V_{hs} - nV_{cs}) - (1 - \mu)(V_{hr} - nV_{cr}) = 0 \quad \Rightarrow \quad \frac{1}{\mu} - 1 = \frac{V_{hs} - nV_{cs}}{V_{hr} - nV_{cr}} = \frac{R_{hs} - R_{cs}}{R_{hr} - R_{cr}} = \frac{\Delta T_s}{\Delta T_r} \quad (3.5)$$

where μ is the fraction of ones in the bitstream, as determined by the decimation filter, which is a simple counter in this first-order modulator. This shows that the temperature-difference ratio can be readily derived from the decimated value.

The signal corresponding to CO₂ variations is extremely small. When the heating currents are 2.5 mA and 0.5 mA for the hot and cold states, respectively, the resulting resistance difference between the hot and cold states is about 5.8 Ω , while a 100 ppm increase in CO₂ concentration will only add 0.15 m Ω . This corresponds to the resistance resolution mentioned earlier of about 15.3 bits relative to the resistance difference (equivalent to about 19.5 bits relative to the total nominal resistance of 110 Ω).

To achieve this resolution, the noise in the system needs to be sufficiently small, including the quantization noise of the $\Delta\Sigma$ ADC and the thermal noise contributed by the transducers, the bias currents, and the switched-capacitor circuit. These thermal noise sources manifest themselves as kT/C noise in the charge-balancing process, and can be reduced by increasing the unit-capacitor size C_s or by increasing the over-sampling ratio (OSR) of the modulator [20]. At $C_s = 1$ pF, chosen to limit the total die area, an over-sampling ratio (OSR) of at least 2^{18} is required. At this OSR, the modulator is limited by kT/C noise, since the quantization noise is well below the required level. Note that this implies that at the chosen capacitor sizing, there is no benefit in going for a higher-order modulator. The capacitors are implemented using stacked metal fringe capacitors (finger capacitors). The total capacitance, including all the sampling capacitors and the integration capacitors, is about 50 pF, which accounts for about 1/3 of the area of the readout electronics. The modulator is operated at a clock frequency of 83.3 kHz (one delta-sigma clock period is 12 μ s), leading to a modulator-operating time of about 3.2 s. Including additional time for thermal settling of about 1.3 s, a total time of 4.5 s is needed to determine the temperature-difference ratio. This time can be reduced by increasing the capacitor sizes, or by increasing the clock frequency, both of which will translate into an increase in the power consumption of the modulator, but will help to reduce the energy consumed per measurement, because the overall power consumption is dominated by the transducers.

3.3.3 Switched-Capacitor Circuit in Power Mode

In power mode, the voltage ratio proportional to the power-difference ratio in (3.4) is digitized. This is implemented by reconfiguring the switched-capacitor circuit with a reversed bs polarity (which is implemented, as shown in Figure 3.4, by inverting bs after the quantizer). Moreover, the input voltages are connected through the cross-connections, so that the ‘hot’ voltages (V_{hs} , V_{hr}) are now sampled by the scaled capacitors $5C_s$, while the ‘cold’ voltages (V_{cs} , V_{cr}) are sampled by the unit capacitors C_s , thus realizing the ‘ n ’ factor in the second voltage ratio of (3.4). Thus, a charge proportional to $(nV_{hs} - V_{cs})$ from the sensitive transducers is continuously balanced by a charge proportional to $-(nV_{hr} - V_{cr})$ from the reference transducers, leading to a decimated output μ that is a function of the second voltage ratio in (3.4), similar to the relation given in (3.5) for temperature mode. An important difference with temperature mode is that the signal charge that is processed is substantially larger, as is evident from (3.4). As a result, the OSR

needed to reduce the thermal noise to the desired 15.3-bit level is much lower than the OSR needed in temperature mode. At this lower OSR, the first-order $\Delta\Sigma$ ADC becomes quantization-noise limited. Since the conversion during power mode takes only a fraction of the overall conversion time, a slightly higher OSR of 2^{16} is used than what is strictly required, to obtain a quantization-noise that meets the target with margin [21]. At a clock frequency of 83.3 kHz, this leads to a modulator-operating time of 0.8 s. Including additional time for thermal settling of about 0.7 s, a total time of 1.5 s is needed to determine the power-difference ratio. For a complete ratiometric thermal-resistance measurement, the modulator first spends 4.5 s in temperature mode and then 1.5 s in power mode, giving a total measurement time of 6 s.

3.3.4 Dynamically-Matched Current Sources

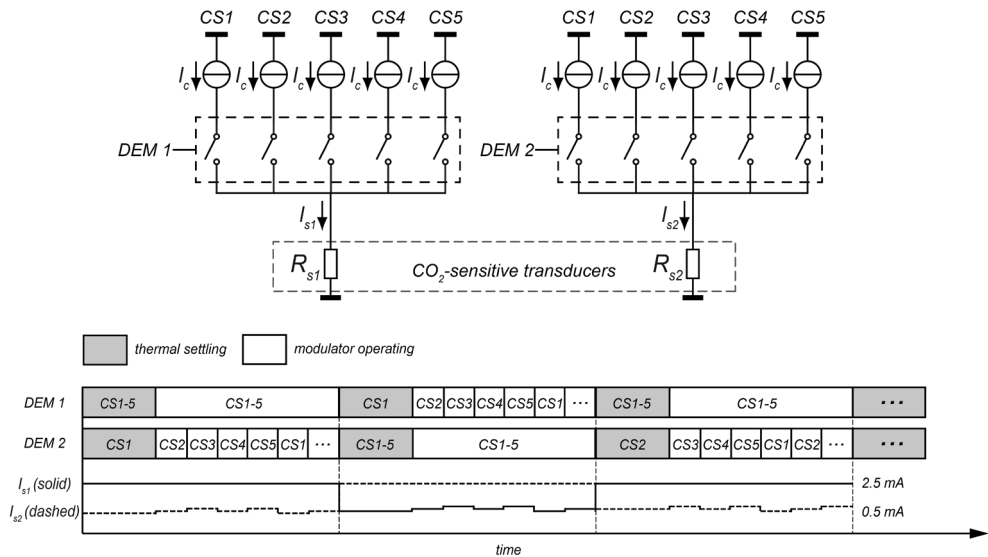


Figure 3.5. Dynamically-matched current sources and associated timing diagram (same algorithm applies to the current sources for the reference transducers).

Errors in the 1 : n bias current ratio lead to errors in the measured θ ratio. System-level simulations have shown that to reduce the resulting error in the measured CO_2 concentration to less than 200 ppm after a one-point offset trim, the current ratio should be accurate to 0.06%. To achieve this, dynamic element matching (DEM) is used (Figure 3.5). Each transducer is associated with a set of 5 unit-current sources,

each of which can be connected to the transducer via a switch. These switches are digitally controlled according to the DEM timing diagram shown in Figure 3.5. When one sensitive transducer is biased by all five unit current sources (in the hot state), the other sensitive transducer is sequentially biased by one unit current source (in the cold state), generating an accurate average current ratio of five. The same biasing approach is applied to the reference transducers. It should be noted that the current-domain chopping (indicated in Figure 3.3) is also implemented by this switching scheme (switching between I_c and $5I_c$). The reason for not physically swapping the two current outputs is that we include a current-trimming function to compensate for the mismatch of the transducers, as described in the next section.

3.3.5 Current-Trimming DACs

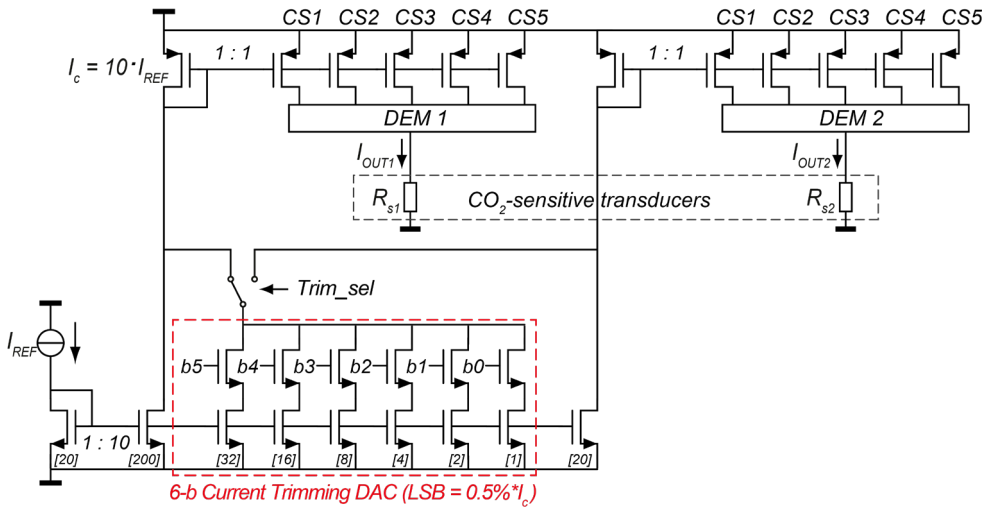


Figure 3.6. Circuit diagram of the current sources with a 6-bit current trimming DAC (LSB current = $0.5\% \times I_c$; the current sources as well as the current trimming DAC for the reference transducers are identical, not shown here; cascode transistors omitted for simplicity).

In principle, the errors due to transducer mismatch are modulated to an AC signal by the periodic chopping of the transducers. However, it may still be necessary to trim the initial mismatch so that the ripple caused by the mismatch at the output of the first integrator will not overload the $\Delta\Sigma$ modulator. As shown in Figure 3.6, the two currents I_{OUT1} and I_{OUT2} , biasing the sensitive transducers R_{s1} and R_{s2} are

generated using PMOS current mirrors (an identical circuit, not shown, is used for the reference transducers). A 6-bit binary-weighted current DAC (LSB current = $0.5\% \times I_c$), embedded in the current source circuit, is used to trim the input current of these current mirrors, thus effectively compensating for the resistance mismatch between R_{s1} and R_{s2} . Note that the current ratio between I_{OUT1} and I_{OUT2} does not need to be accurate, as long as both I_{OUT1} and I_{OUT2} provide an accurate $1 : n$ current ratio sequentially to the individual transducers, which is ensured by the current-source DEM (Figure 3.5). In this way, the measured thermal-resistance ratio is a ratio between the averaged thermal resistances of the two sensitive transducers and that of the two reference transducers.

3.4 Experimental Results and Discussion

The readout circuit as well as the tungsten-wire transducers have been designed and fabricated in a $0.16 \mu\text{m}$ CMOS technology. Figure 3.7 shows the layout plot and micrographs of the integrated readout circuit and one of the transducers. The active die area of the circuit amounts to 0.7 mm^2 , of which 0.37 mm^2 is occupied by the current sources and 0.33 mm^2 by the switched-capacitor $\Delta\Sigma$ modulator. The transducers are on another chip, fabricated using the same CMOS process followed by an etch step to release the wires, so as to be able to test different implementations of the transducers. To investigate the behavior at higher heating power levels, a commercial micro-heater was also used (Figaro TGS-8100, a metal-oxide-semiconductor gas sensor of which we use the integrated micro-heater) [10], which can withstand higher power and has similar electrical and thermal characteristics as the CMOS tungsten transducers. Four micro-heaters from four Figaro devices were connected to our readout circuits, two of which were sealed at the package to act as reference devices. For electrical measurements, the readout IC has been characterized in combination with this commercial micro-heater. Both the commercial heaters and the CMOS tungsten transducers have been used for CO_2 measurements.

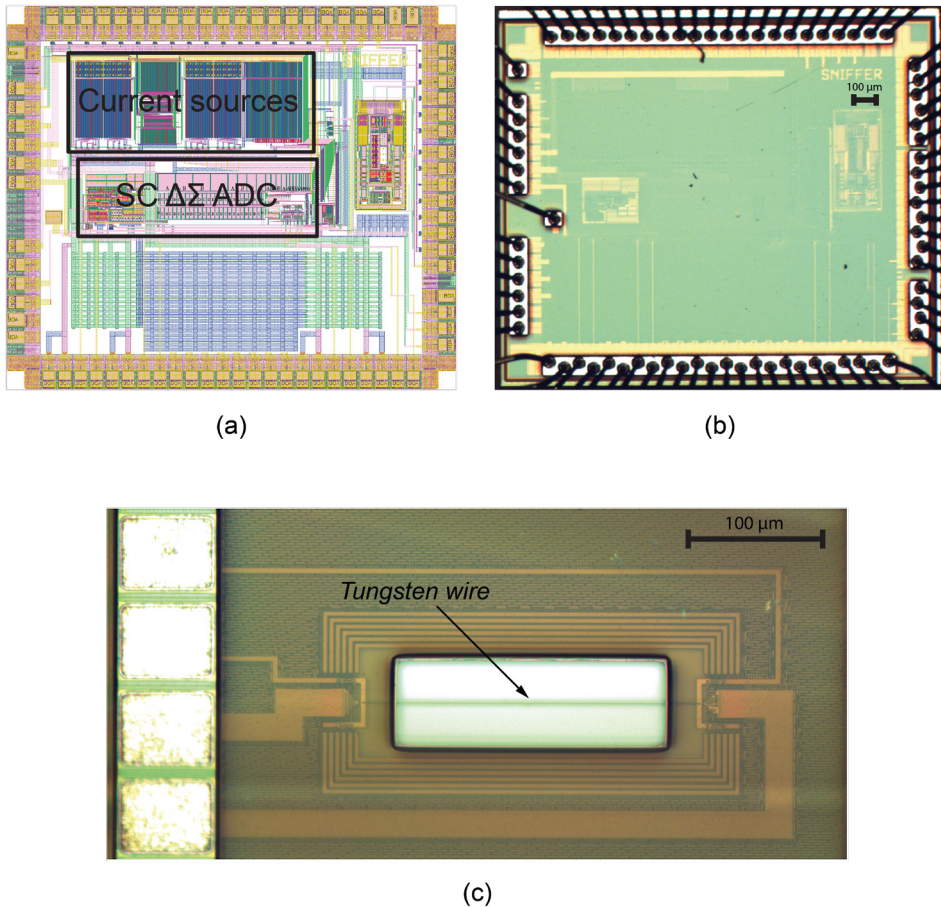


Figure 3.7. (a) Layout plot, (b) micrograph of the integrated readout circuit and (c) micrograph of a CMOS-compatible tungsten-wire transducer (using Kelvin connections, two wide tracks for current driving and two narrow tracks for voltage sensing).

3.4.1 Electrical measurements

Figure 3.8 shows the measured current ratios of the dynamically-matched current sources for 4 samples of the readout IC. The initial mismatch of about $\pm 0.2\%$ is improved by an order of magnitude with DEM (better than the required 0.06% error budget). This proves that DEM effectively averages out the variations due to mismatch and thus improves the accuracy of thermal-resistance measurement.

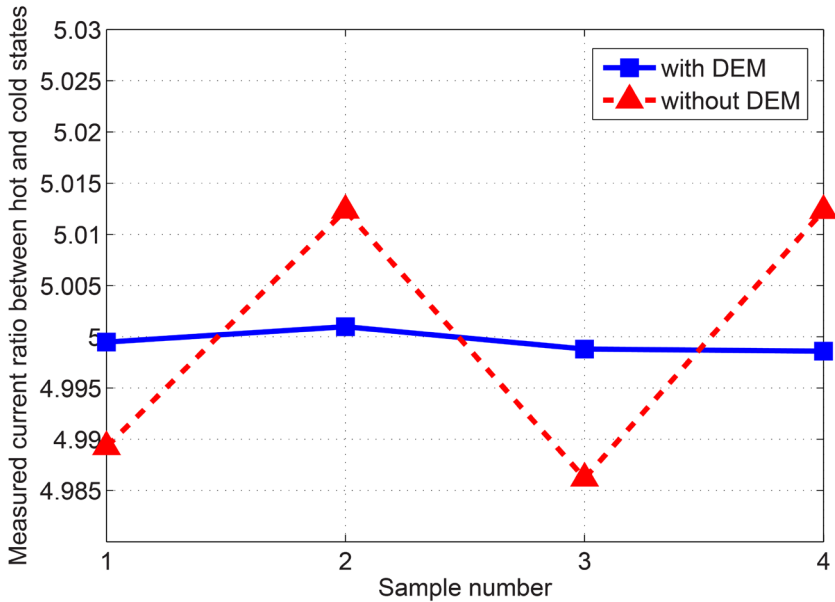


Figure 3.8. Measured current ratios of the dynamically-matched current sources on 4 samples of the chip (initial mismatch is about 0.2%; after DEM the inaccuracies are -0.01%, 0.02%, -0.02% and -0.03% respectively).

Figure 3.9 shows how the resolution of the thermal-resistance measurement (and hence the equivalent CO_2 resolution) varies as a function of the measurement time. Results of two versions of the circuit are shown. The first version employs a switched-capacitor circuit that samples the transducer voltage on only one of the two clock phases [9]. The second version corresponds to the implementation discussed in Section 3.3, employing the double-sampling scheme shown in Figure 3.4. This scheme doubles the signal amplitude compared to the single-sampling scheme, while the noise level remains the same. Therefore, for the same measurement time, the SNR increases by 6 dB. The $2\times$ improvement in CO_2 resolution observed in the experiment matches well with this expectation. At the targeted measurement time of 6 s, the second version of the readout circuit achieves an equivalent CO_2 resolution of 250 ppm (1σ) at ambient conditions in the lab. This is in reasonable agreement with the expectation based on a calculation of the input-referred signal-to-noise ratio as a function of OSR (dashed curve in Figure 3.9). To achieve the targeted resolution of 200 ppm, a measurement time of 9 s is needed. For comparison, Figure 3.9 also shows the measured CO_2 resolution

at different controlled CO₂ levels (at 500 ppm, 2500 ppm, 4500 ppm, 9000 ppm), obtained from measurements performed in a climate chamber. These results will be discussed further in Section 3.4.2.

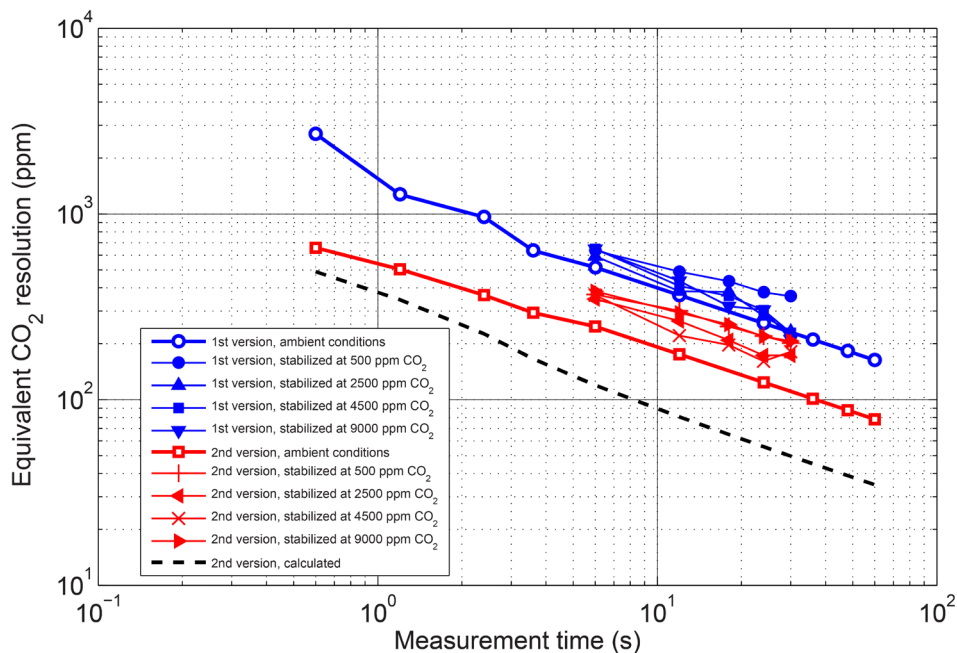


Figure 3.9. Equivalent CO₂ resolution (1σ) derived from the standard deviation of the measured thermal-resistance ratio at ambient conditions (solid curves) and at different controlled CO₂ levels, using the first version (single-sampling) and the second version (double-sampling) of the readout circuit in combination with Figaro micro-heaters, along with the calculated resolution of the double-sampling scheme.

To demonstrate the insensitivity of the ratiometric measurement to the absolute current and power levels, Figure 3.10 shows the measured temperature, power and thermal-resistance ratios as a function of I_c (the bias current at the ‘cold’ state). For a $\pm 10\%$ change in I_c , the power ratio only changes by about ± 10 ppm. For our CO₂ sensor, 200 ppm change in CO₂ will result in about 50 ppm change in thermal-resistance ratio, which requires the errors of power ratio to be within 25 ppm. Thus, the measured results indicate that the ratiometric measurement effectively alleviates the dependence on the stability of the power dissipation. The

measured thermal-resistance ratio also varies by about ± 10 ppm, which could be due to the secondary temperature dependence of the thermal conductivity of air.

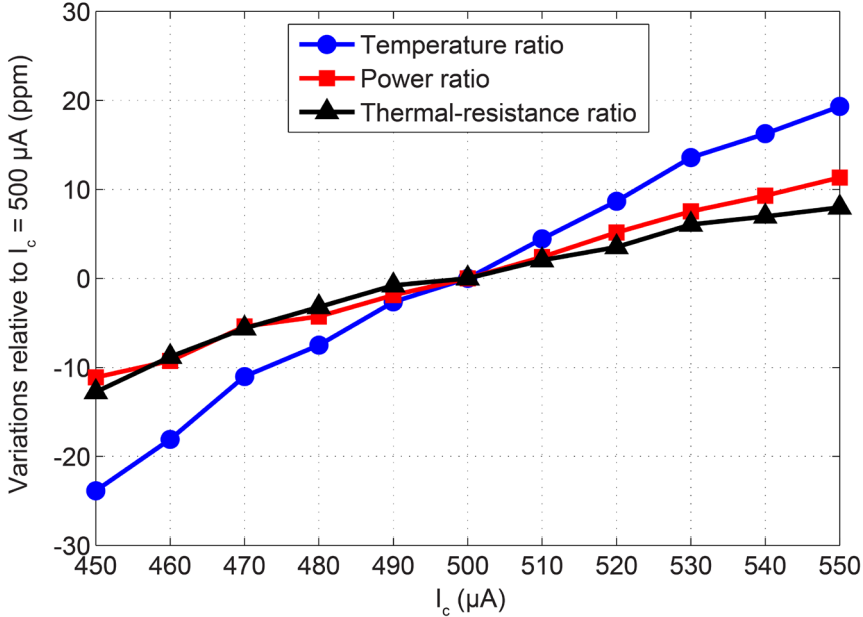


Figure 3.10. Variations in temperature, power and thermal-resistance ratios between the sensitive and reference transducers as a function of the bias current at ‘cold’ state (I_c).

To demonstrate the effectiveness of the trimming scheme, Figure 3.11 shows the measured temperature, power and thermal-resistance ratios, as well as the peak-to-peak voltage at the output of the integrator, for different current-trimming levels of the current sources that bias the sensitive transducers. The current trimming levels are indicated in LSB steps of the current DAC, where a negative number indicates the trimming current is added to one of the sensitive transducers (R_{s1}) and a positive number indicates the trimming current is added to the other sensitive transducer (R_{s2}). When the trimming level is less than 4 LSBs, the integrator’s output swing is limited. For trimming levels above 8 LSBs, the integrator starts to clip, leading to large errors in the measured ratios. Note that in this particular case, the transducers are quite well matched, leading to an optimum for trimming level 0. In the case where transducers have larger mismatch, this current trimming function will suppress the initial mismatch between the transducers and thus prevent the

modulator from clipping. Note that there is still some variation in the measured ratios when the trimming level is less than 4 LSBs. This is to be expected, since the trimming scheme always adds current to either of the two transducers and hence increases the power dissipation of the sensitive transducers. This will lead to a gain error in (3.4). In practice, such a gain error will be compensated for by the overall calibration of the sensor, along with the gain errors due to the tolerances on the nominal thermal resistances of the transducers.

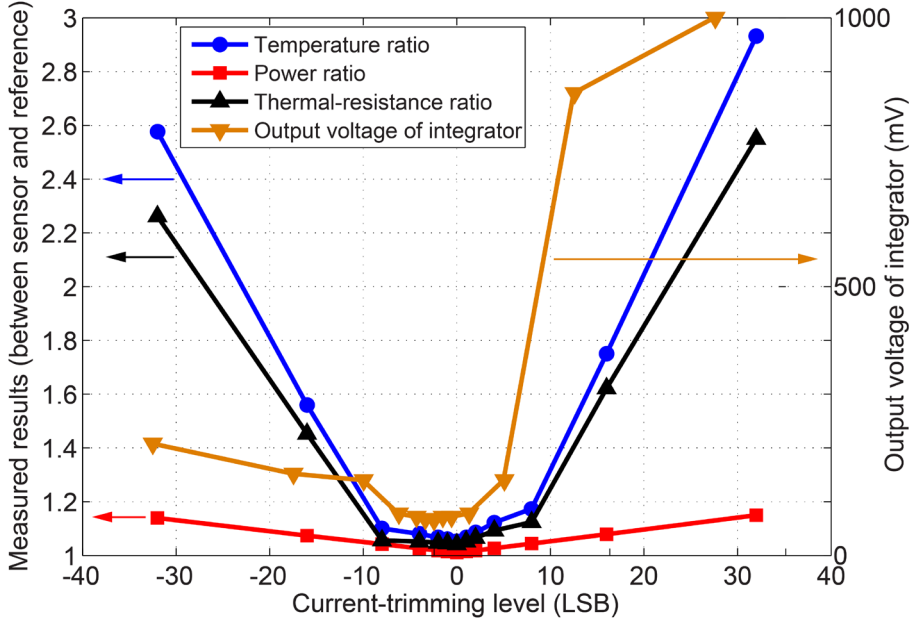


Figure 3.11. Temperature, power, thermal-resistance ratios and the (peak-peak) voltage at the output of the integrator as a function of the current trimming level (in LSB steps of the trimming DAC).

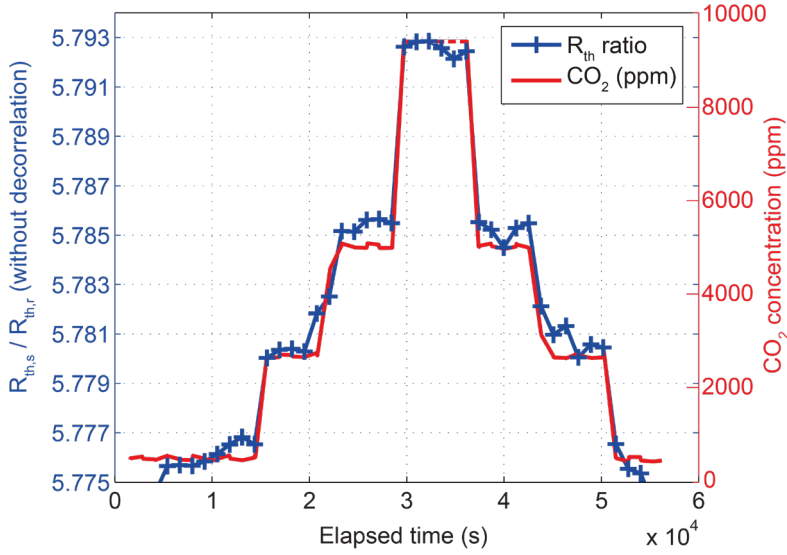
To quantify the chip-to-chip variation introduced by the readout circuit, 18 samples of the chip have been measured in combination with the same set of off-chip fixed resistors. To exclude the effect of ambient variations, non-suspended resistors with a low temperature coefficient were used. To allow the circuit to operate with these resistors, the dynamic switching of the current level was disabled, i.e. two resistors emulated a ‘hot’ resistance of about $120\ \Omega$ and two a ‘cold’ resistance of about $100\ \Omega$. Since this mode of operation precludes the use of dynamic element matching, the measured spread includes the effect of current-source mismatch. In spite of this, the measured standard deviation of the decimated

output is less than 0.6%. This is much less than the expected processing spread of the tungsten transducers, indicating that the spread due to the readout circuit is non-dominant and can be corrected for in the calibration procedure that will be needed for the transducers.

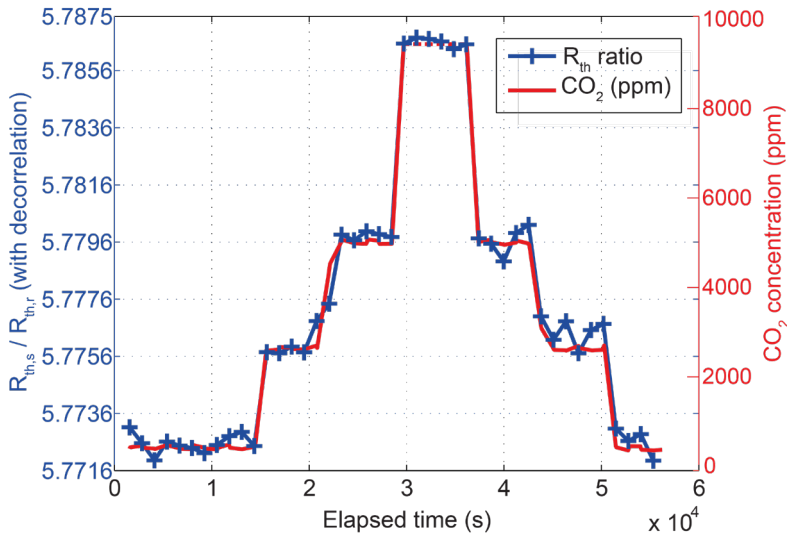
3.4.2 CO₂ measurements

The first version of the readout circuit has been measured in combination with tungsten-wire transducers implemented in the back-end of a standard 0.16 μm CMOS process [9]. The sensitive and reference wires have a length of 250 μm . The cavity opening of the sensitive transducer is 200 μm , while that of the reference transducers is 50 μm . Both the approach of using a narrower etch window and the approach of package-level sealing to achieve a lower sensitivity of the thermal resistance to CO₂ in the reference device have been explored. Two transducer chips, each with a pair of transducers, were used. One chip, with the sensitive transducers, was packaged in a ceramic dual-in-line (DIL) package of which the cavity is exposed to the ambient air, and the other, with the reference transducers, was packaged in a DIL package of which the cavity is sealed. Note that there are potential solutions for sealing the reference transducers at the wafer-level, such as wafer-to-wafer capping, die-to-wafer bonding and wafer-level thin-film capping [22]. In this way, both types of transducers can in the future be integrated in the same package.

Figure 3.12 shows the thermal-resistance ratio measured using the first version of the readout circuit while the CO₂ concentration was changed step-wise from 500 ppm to 9000 ppm. To reduce the noise level, which, as mentioned, is relatively high for the first version of the circuit, the measurement time was increased to 70 s for this experiment, at which the measured resolution is equivalent to 228 ppm CO₂ (1σ). The thermal-resistance ratio measured using the readout circuit has a sensitivity of 0.29 ppm/ppm CO₂, and shows good correlation with the CO₂ level measured using an NDIR-based reference sensor (Figure 3.12a). Note that at the highest CO₂ level, this reference sensor was operated just beyond its full scale, causing its output to clip, but the parameters of the mass flow controllers that set the CO₂ concentration were correct.



(a)



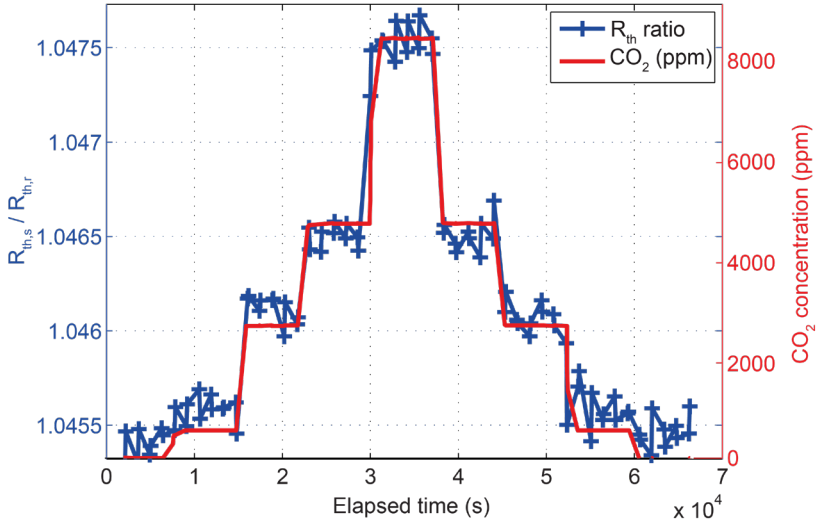
(b)

Figure 3.12. Thermal-resistance ratio measured using the first version of the readout circuit with a 70 s measurement time, in combination with tungsten-wire transducers, for step-wise changing CO_2 concentration, without (a) and with (b) compensation for temperature and pressure cross-sensitivity, along with CO_2 concentration measured using an accurate reference NDIR sensor.

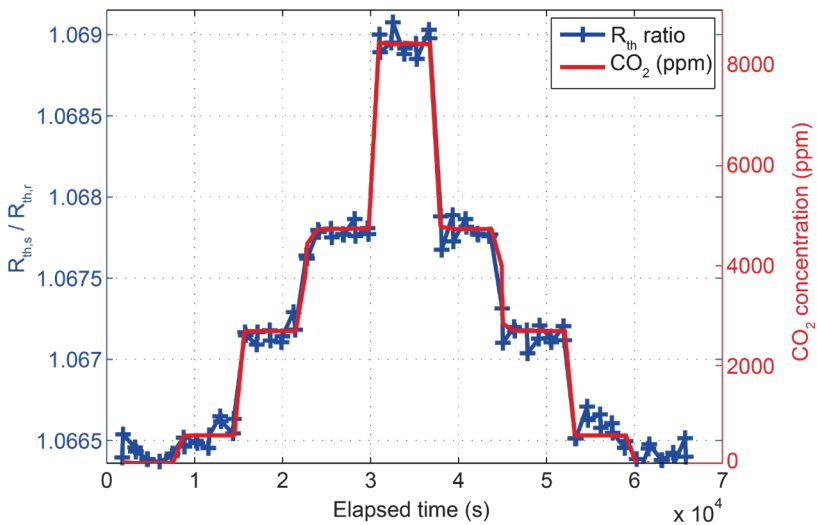
As thermal-conductivity is not only sensitive to the change of CO₂, but is also highly influenced by environmental variations, we use reference temperature, humidity and pressure sensors to accurately measure the changes in ambient conditions, and determine the cross-sensitivities and then de-correlate the influences of these ambient variations by least-square curve fitting on the measurement results. The results after de-correlation are shown in Figure 3.12b. These measurements were performed using a 2.5 mA bias current (hot state), at which the temperature rise of the tungsten transducer (ΔT) is about 35°C above ambient temperature. When the bias current was increased to 5 mA ($\Delta T > 100^\circ\text{C}$), a drifting behavior was observed.

The readout circuit has also been tested with discrete heaters: the micro-heaters in Figaro TGS-8100. The results are shown in Figure 3.13, for both versions of the readout circuit. Four different CO₂ levels (500 ppm, 2500 ppm, 4500 ppm, 9000 ppm) and a baseline (pure air) were used in this experiment. The thermal-resistance ratio measured has a sensitivity of 0.27 ppm/ppm CO₂, and shows good correlation with the reference CO₂ measurements.

In these experiments, a measurement time of 30 s was used, at which the second version of the readout circuit meets the targeted resolution of 200 ppm (Figure 3.13b). As shown in Figure 3.9, the CO₂ resolution measured at controlled CO₂ levels is about 370 ppm in a measurement time of 6 s, which is worse than the previous measurement at (uncontrolled) ambient conditions (250 ppm). This difference could be due to noise associated with airflow in the setup. As a result, a measurement time of 30 s is needed to meet the targeted resolution of 200 ppm. As expected, the resolution obtained with the first version of the circuit is approximately two times worse.



(a)



(b)

Figure 3.13. Thermal-resistance ratio measured using the first (a) and second (b) version of the readout circuit, both with a 30 s measurement time, in combination with Figaro TGS 8100 transducers, with compensation for temperature and pressure cross-sensitivity, for step-wise changing CO_2 concentration, along with CO_2 concentration measured using an accurate reference NDIR sensor.

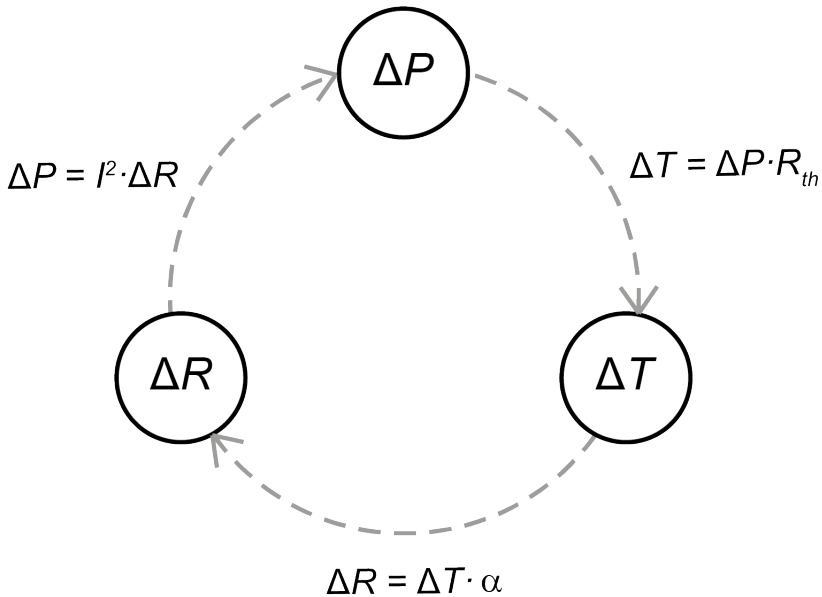


Figure 3.14. Feedback loop in the heating of the TC-based transducer.

While the micro-heaters used can support higher power levels (the temperature rise at 2.5 mA bias current is about 20°C), only a very modest improvement in resolution was found when the bias current was further increased from 2.5 mA to 3 mA. This is probably due to the fact that, while a higher power level gives a higher signal amplitude, it also reduces the sensitivity of the thermal conductivity of air to CO₂ concentration, due to the temperature dependency of this sensitivity. In addition, a positive feedback loop may exist in the structure of a TC-based resistive transducer biased by a constant current source, which also limits the maximum current levels. If the transducer has a positive temperature coefficient, then its self-heating will increase its electrical resistance due to its temperature dependency. As illustrated in Figure 3.14, an increase in bias current leads to an increase in power dissipation (ΔP), which then leads to an increase in transducer temperature (ΔT). Due to its positive temperature coefficient, the transducer's resistance increases (ΔR), and this again increases its power dissipation (ΔP), thus resulting in a positive feedback loop. The loop gain is equal to $R_{th} \cdot \alpha \cdot I^2$, where R_{th} is the thermal resistance, α the temperature dependence of the resistance, I the level

of the bias current. Thus, to mitigate the influence of this feedback loop, the bias current should be chosen such that the loop gain is far from unity.

Table 3.1. Performance of the proposed sensor compared to the prior art

Parameter	This work			[3]	[2]	IR11BD [23]
Method	TC			TC	TC	NDIR
Technology	CMOS			SOI MEMS	SOI MEMS	–
Readout IC	Yes			No	No	No
Die size	3 mm ²			16 mm ²	9 mm ²	–
Supply voltage	1.8 V			–	–	3 - 15 V
Power (sensor)	10.8 mW			3 mW	7 mW	180 mW
Power (readout)	0.4 mW			–	–	–
Version of readout	1 st version	1 st version	2 nd version	–	–	–
Meas. time	70 s	30 s	30 s	60 s	–	20 s
CO ₂ resolution (1 σ)	228 ppm [*]	400 ppm [†]	202 ppm [†]	456 ppm	<1%	<100 ppm

* In combination with CMOS-compatible tungsten-wire transducers

† In combination with discrete micro-heaters (Figaro TGS 8100) [10]

A performance summary and comparison with other CO₂ sensors reported in literature as well as with a commercial product is shown in Table 3.1. Compared with other TC-based CO₂ sensors, the CO₂ transducer (tungsten wire) and readout circuit in this work are both implemented in standard CMOS technology with minimum post-processing steps, unlike the special MEMS processes required to fabricate the other transducers. The active die area of the sensor including readout circuit is about 3 mm² which is much smaller than that of the sensor in [2] or [3]. The first version of the chip in combination with the CMOS tungsten-wire transducers achieves 228 ppm CO₂ resolution in 70 s in the indoor CO₂ range (at 500 ppm level), which is 2 \times better than the resolution reported in [3]. In combination with the commercial heaters (Figaro TGS-8100), the same readout achieves 400 ppm resolution in 30 s. The second version of the chip (with double sampling) in combination with commercial heaters (Figaro TGS-8100) achieves 202 ppm resolution in 30 s. As most of the power is used for heating the transducer, reducing the power consumption of readout circuit would only lead to a minor

improvement. To optimize the design for energy efficiency, further improvement can be made in decreasing the measurement time, which can be done by increasing the size of the switches and operating the modulator at a higher clock frequency. Alternatively, the capacitor size can be further increased to reduce the circuit noise, at the cost of increased die size. Note that in the latter case, the size of switches should also be increased in order to meet the settling requirement of the switched-capacitor circuit.

3.5 Conclusions

In this chapter, a novel readout circuit for ratiometric thermal-conductivity measurement has been reported. The circuit digitizes both the temperature rise and the power dissipation of CO₂-sensitive transducers relative to that of reference transducers, from which their thermal-resistance ratio can be calculated, thus circumventing an accurate power reference. Experimental results have shown that for a $\pm 10\%$ change in bias current, the measured power ratio between sensitive and reference transducers only changes by about ± 10 ppm. A pair of gas-sensitive transducers is combined with a pair of reference transducers to cancel baseline resistance, thus greatly relaxing the dynamic range requirement of the ADC. The transducers are dynamically swapped during a conversion to dynamically cancel out the errors due to transducer mismatch. An accurate current ratio between ‘hot’ and ‘cold’ states is generated by dynamically-matched current sources, and furthermore, a 6-bit current DAC is used to trim the transducers to ensure that the residual mismatch will not overload the $\Delta\Sigma$ modulator. Experimental results show that the applied techniques are effective, and using this ratiometric readout circuit, a CMOS-compatible thermal-conductivity-based CO₂ sensor achieves 228 ppm (1σ) CO₂ resolution. To further evaluate the capability of the readout circuit, we use micro-heaters in Figaro TGS 8100 as a substitute for tungsten-wire transducers. The second version of the design achieves 200 ppm resolution over a CO₂ range of 500 to 9000 ppm, which indicates that high-resolution TC-based CO₂ sensing is attainable even with on-chip electronics, thus facilitating the realization of fully-integrated CO₂ sensors for air-quality monitoring, which are much smaller and less expensive than current CO₂ sensors.

References

- [1] I. Simon and M. Arndt, "Thermal and gas-sensing properties of a micromachined thermal conductivity sensor for the detection of hydrogen in automotive applications," *Sens. Actuators A: Phys.*, vol. 97–98, pp. 104-108, Apr. 2002.
- [2] K. Kliche, et al., "Sensor for gas analysis based on thermal conductivity, specific heat capacity and thermal diffusivity," in *Proc. IEEE Int. Conf. on MEMS*, 2011, pp. 1189-1192.
- [3] K. Kliche, et al., "Sensor for thermal gas analysis based on micromachined silicon-microwires," *IEEE Sensors J.*, vol. 13, pp. 2626-2635, Jul. 2013.
- [4] N. Tadic, M. Zogovic, and D. Gobovic, "A CMOS controllable constant-power source for variable resistive loads using resistive mirror with large load resistance dynamic range," *IEEE Sensors J.*, vol. 14, pp. 1988-1996, Jun. 2014.
- [5] S. Chan and P. C. Chan, "A resistance-variation-tolerant constant-power heating circuit for integrated sensor applications," *IEEE J. Solid-State Circuits*, vol. 34, no. 4, pp. 432–439, Apr. 1999.
- [6] C.A. Leme, R. Lenggenhager, I. Filanovsky, H. Baltes, "Linear CMOS power controller for precision sensor applications," in *Proc. IEEE Int. Symp. Circuits Syst.*, 1992, pp. 1844-1846.
- [7] S. Sarfraz, R. V. Kumar, and F. Udea, "A high temperature and low power SOI CMOS MEMS based thermal conductivity gas sensor," in *Proc. IEEE Int. Semiconductor Conf.*, 2013, pp. 51-54.
- [8] S. Z. Ali, et al., "Tungsten-based SOI microhotplates for smart gas sensors," *J. Microelectromech. Syst.*, vol. 17, pp. 1408-1417, Dec. 2008.
- [9] Z. Cai, et al., "An integrated carbon dioxide sensor based on ratiometric thermal-conductivity measurement," in *Proc. IEEE Int. Conf. on Solid-State Sensors, Actuators and Microsystems (Transducers '15)*, 2015, pp. 622-625.
- [10] FIGARO TGS8100 datasheet (rev06), FIGARO [Online]. Available: <http://www.figaro.co.jp>.
- [11] Z. Cai, et al., "A ratiometric readout circuit for thermal-conductivity-based resistive gas sensors," in *Proc. ESSCIRC*, 2015, pp. 275-278.
- [12] N.M. Mohan, B. George and V.J. Kumar, "A novel dual-slope resistance-to-digital converter," *IEEE Trans. Instrum. Meas.*, vol. 59, no. 5, pp. 1013-1018, May 2010.
- [13] C. K. Leung and D. M. Wilson, "Integrated interface circuits for chemiresistor arrays," in *Proc. IEEE Int. Symp. Circuits Syst.*, 2005, pp. 5914-5917.
- [14] X. Mu, et al., "CMOS monolithic nanoparticle-coated chemiresistor array for micro-scale gas chromatography," *IEEE Sensors J.*, vol. 12, no. 7, pp. 2444-2452, Jul. 2012.

- [15] M. Grassi, P. Malcovati, and A. Baschiroto, "A 160 dB equivalent dynamic range auto-scaling interface for resistive gas sensors arrays," *IEEE J. Solid-State Circuits*, vol. 42, no. 3, pp. 518-528, Mar. 2007.
- [16] A. K. Basu, H. Sarkar, S. Bhattacharya, "Fabrication and resilience measurement of thin aluminium cantilevers using scanning probe microscopy," in *Proc. Int. Conf. C2E2 in foundations and frontiers in computer, communication and electrical engineering*, Taylor and Francis, Mankundu, pp 457-460, 2016.
- [17] D. B. Knorr, K. P. Rodbell, "The role of texture in the electromigration behavior of pure aluminum lines," *J. Applied Physics*, vol 79, issue 5, pp. 2409-2417, Mar. 1, 1996.
- [18] K. Bult and G. J. G. M. Geelen, "A fast-settling CMOS op amp for SC circuits with 90-dB DC gain," *IEEE J. Solid-State Circuits*, vol. 25, no. 6, pp. 1379-1384, Dec 1990.
- [19] H. Fiedler, et al., "A 5-bit building block for 20 MHz A/D converters," *IEEE J. Solid-State Circuits*, vol. 16, no. 3, pp. 151-155, Jun. 1981.
- [20] R. Schreier, J. Silva, J. Steensgaard and G. C. Temes, "Design-oriented estimation of thermal noise in switched-capacitor circuits," *IEEE Trans. Circuits Syst., I, Regular papers*, vol. 52, no. 11, pp. 2358-2368, Nov. 2005.
- [21] J. Markus, J. Silva, and G. C. Temes, "Theory and applications of incremental $\Delta\Sigma$ converters," *IEEE Trans. Circuits Syst. I, Fundam. Theory Applicat.*, vol. 51, no. 4, pp. 678-690, Apr. 2004.
- [22] K. Seetharaman, et al., "A robust thin-film wafer-level packaging approach for MEMS devices." *J. Microelectronics and Electronic Packaging*, vol. 7, pp. 175-180, Jul. 2010.
- [23] SGX IR11BD datasheet, SGX Sensortech [Online]. Available: <http://www.sgxsensortech.com/>.

Chapter 4

ALGORITHMIC AMPLITUDE-DOMAIN READOUT

This chapter is based on the publication “A CMOS Readout Circuit for Resistive Transducers Based on Algorithmic Resistance and Power Measurement,” in IEEE Sensors Journal, vol. 17, no. 23, pp. 7917-7927, Dec.1, 2017.

4.1 Introduction

Thermal-conductivity (TC)-based CO₂ sensors rely on accurate measurements of the temperature and power dissipation of the resistive transducer. When implementing a high-resolution sensor this can become quite challenging because an accurate power reference is difficult to realize.

The main problem with previous constant (reference) power circuits implemented in CMOS technology is their lack of accuracy (especially over temperature). Their reported inaccuracy typically exceeds 1% over load (resistance) variations, while their temperature dependency is often not specified [1][2][3]. Furthermore, most of them rely on external voltages and current (or resistance) references. In TC-based CO₂ sensors, however, variations in heater power will be caused not only by resistance changes but also by ambient temperature variations, due to the temperature dependence of the heater's resistance. Instead of stabilizing the dissipated power, one alternative is to directly measure both the heater's resistance and power dissipation, allowing their impact to be factored into the final measurement results. However, accurately measuring power dissipation requires an accurate power reference, which, in turn, requires accurate voltage and resistance references.

In CMOS processes, bandgap voltage references are best-in-class. They combine a voltage that is proportional to absolute temperature (PTAT) with a voltage that is complementary to absolute temperature (CTAT), both generated

using the parasitic BJTs available in any CMOS process, to obtain a temperature-independent reference voltage [4]. Using precision circuit design techniques as well as appropriate calibration and correction schemes, bandgap references can achieve high accuracy over a wide temperature range with low chip-to-chip variations [5][6][7][8]. For instance, in [7] a temperature dependency of 5-12 ppm/°C over the temperature range of -40°C to 125°C has been achieved after a single room-temperature trim. A key limiting factor are the offset and gain errors added by the analog circuitry that combines the PTAT and CTAT voltages, since both errors cannot be removed by a single trim [8]. Alternatively, the PTAT and CTAT voltages can also be combined in the charge domain by using a switched-capacitor integrator, resulting in very accurate voltage references [9]. In addition, accurate voltage measurements with algorithmic curvature correction have also been proposed, resulting in 12-bit accuracy from -40°C to 125°C [10].

Compared to voltage references, on-chip reference resistors are even more difficult to realize, since on-chip resistors typically suffer from significant process variation and temperature drift. Especially the latter results in errors which cannot be easily removed by calibration and trimming. Polysilicon resistors are relatively stable over temperature, but still exhibit temperature coefficients ranging from $\pm 0.1\%/^{\circ}\text{C}$ to $\pm 1\%/^{\circ}\text{C}$ [8][11][12][13]. By combining resistors and/or linear MOSFETs with positive and negative temperature coefficients, a near-zero temperature coefficient of resistance (TCR) can be achieved [11][12][13]. However, the exact composition of such combinations will be process-dependent, typically resulting in residual TCRs of at least 100 ppm/°C. In consequence, the accuracy of reported on-chip power references [1][2][3] is usually much lower than that of voltage references [5][6][7][8]. In systems that require a stable resistance reference, such as current references [14] or resistor-based temperature sensors [15], the use of switched-capacitor resistors has been investigated. However, this requires stable capacitors and a stable clock. The latter is typically an off-chip quartz crystal, since on-chip oscillators typically exhibit temperature coefficients of about 30 ppm/°C [16][17], i.e., several times higher than that of voltage references. This makes this approach less attractive from a cost point of view.

This chapter presents a circuit capable of accurately measuring resistance and power dissipation without relying on off-chip references. It operates algorithmically, by successively digitizing the voltage drop across a resistive transducer (V_{load}), the voltage drop across an on-chip reference resistor carrying the same current (V_{ref}), and the base-emitter voltages of a single BJT (V_{be}) biased at different current levels, and then processing the results in the digital domain. The

ratio of V_{load} and V_{ref} provides information about the transducer resistance R_{load} relative to the reference resistance R_{ref} . Rather than using an analog bandgap reference circuit, the reference voltage needed to calculate the power dissipation is obtained by combining the digitized base-emitter voltages to construct an equivalent reference voltage in the digital domain. To obtain the temperature information needed to compensate for the temperature dependence of R_{ref} , the same digitized base-emitter voltages are used to construct a digital PTAT voltage, which, combined with the reference voltage, provides accurate information about die temperature. The precision of the circuit is determined by the BJT and its bias circuit, and by the linearity and resolution of the ADC. It is independent of the analog reference voltage of the ADC, which, as will be shown, cancels out. The result is a measurement system that processes the signals as much as possible in the digital domain, and thus circumvents the errors associated with analog signal processing.

Experimental results obtained from a CMOS prototype combined with an external ADC show that the proposed architecture works as expected. After a 1-point trim, the resulting algorithmic temperature sensor achieves an inaccuracy of $\pm 0.25^\circ\text{C}$ (min-max) over a temperature range of -40°C to 125°C , while the algorithmic bandgap reference achieves a temperature coefficient of $18 \text{ ppm}/^\circ\text{C}$, results which both approach the state-of-the-art. The inaccuracy of the power measurements (including load variations and the same temperature range) is better than $\pm 0.8\%$ after trimming each sample at a single temperature. Compared to prior work [1][2][3], it achieves similar accuracy, but across a wide temperature range and without using external voltage and/or current references. When used in a TC-based CO_2 sensor, the proposed system would result in an estimated inaccuracy of 7500 ppm .

The chapter is organized as follows. In Section 4.2, details of the measurement principle are presented. Section 4.3 is devoted to the circuit implementation of the readout circuit. Experimental results and discussions are presented in Section 4.4, and the chapter ends with conclusions.

4.2 Operating Principle

4.2.1 Algorithmic Resistance and Power Measurement

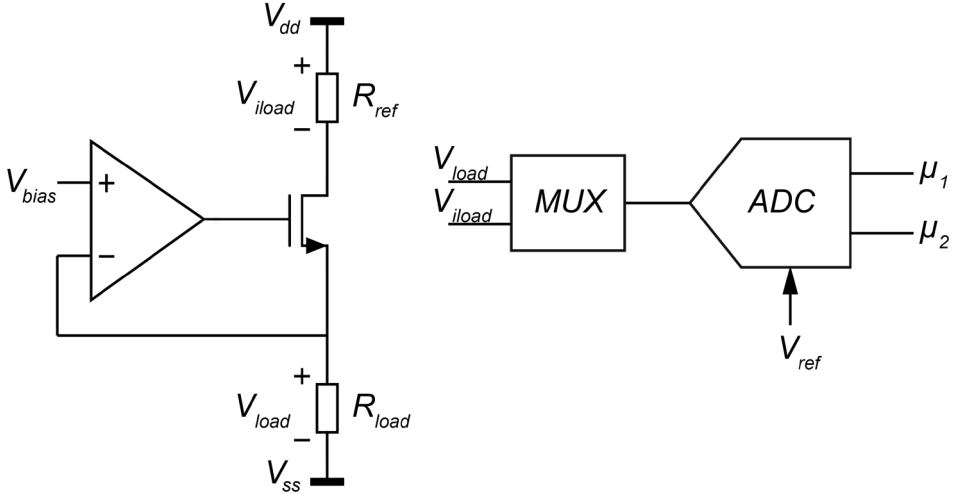


Figure 4.1. Transducer front-end for resistance and power measurement.

Measuring resistance and/or power involves both voltage and current measurements. As shown in Figure 4.1, a transducer R_{load} is biased at a desired voltage V_{bias} by an opamp, while a reference resistor R_{ref} is used to sense the resulting current. The voltages across the transducer and the reference resistor can be measured sequentially by a multiplexed precision ADC, giving two digital outputs:

$$\mu_1 = \frac{V_{load}}{V_{ref}} \quad (4.1)$$

$$\mu_2 = \frac{V_{iload}}{V_{ref}} \quad (4.2)$$

where V_{ref} is the reference voltage of the ADC. This needs to be stable during the measurement, but does not have to be accurate, as it will later be replaced by an accurate reference voltage constructed in the digital domain. These consecutive voltage and current measurements should be taken fast enough to obtain an

accurate power measurement. This is not very difficult to meet in practice, since the variables to be measured (temperature or gas composition) change slowly.

From these results, the transducer's resistance and power dissipation can be calculated:

$$R_{load} = \frac{V_{load}}{I_{load}} = \frac{V_{load}}{V_{iload}} \cdot R_{ref} = \frac{\mu_1}{\mu_2} \cdot R_{ref} \quad (4.3)$$

$$P_{load} = V_{load} \cdot I_{load} = V_{load} \cdot \frac{V_{iload}}{R_{ref}} = \mu_1 \mu_2 \frac{V_{ref}^2}{R_{ref}} \quad (4.4)$$

These results depend on the ADC's reference voltage V_{ref} and on accurate knowledge of the value of R_{ref} . As detailed below, to eliminate the dependence on V_{ref} , we algorithmically construct an accurate bandgap voltage reference, by digitizing several base-emitter voltages. The temperature information contained in these voltages can then be used to compensate for the temperature dependency of R_{ref} .

With the capability to measure resistance and power, the thermal resistance of a TC transducer can also be measured, since thermal resistance can be expressed in terms of electrical resistance and power. As explained in Chapter 2, thermal resistance can be expressed as:

$$R_{th} = \frac{\Delta T}{P_{load}} = \frac{T - T_{amb}}{P_{load}} \quad (4.5)$$

where ΔT is the temperature rise of the TC transducer relative to ambient temperature. If the resistance of the transducer is a linear function of temperature, then:

$$R_{load} = R_{load0} \left\{ 1 + \alpha_{Rload} (T - T_{amb}) \right\} \quad (4.6)$$

where R_{load0} is the value of R_{load} at ambient temperature T_{amb} and α_{Rload} is the resistor's TCR. Combining these two equations results in the following expression for thermal resistance:

$$R_{th} = \frac{R_{load} - R_{load0}}{R_{load0} \cdot \alpha_{Rload} \cdot P} \tag{4.7}$$

The sensitivity of the measured thermal resistance to various sources of error can also be derived from the expressions above:

$$\begin{aligned} \frac{\partial R_{th}}{R_{th}} &\approx \frac{\partial(\Delta T)}{\Delta T} + \frac{\partial P_{load}}{P_{load}} = \frac{1}{\Delta T} \left(\frac{\partial R_{load}}{R_{load0} \alpha_{Rload}} + \partial T_{amb} \right) + \frac{\partial P_{load}}{P_{load}} \\ &= \frac{\partial R_{load}}{R_{load} - R_{load0}} + \frac{\partial T_{amb}}{\Delta T} + \frac{\partial P_{load}}{P_{load}} \end{aligned} \tag{4.8}$$

For the case of a TC-based CO₂ sensor, the equivalent error in thermal resistance (and thus in CO₂ concentration) can then be estimated.

4.2.2 An Algorithmic Bandgap Voltage Reference

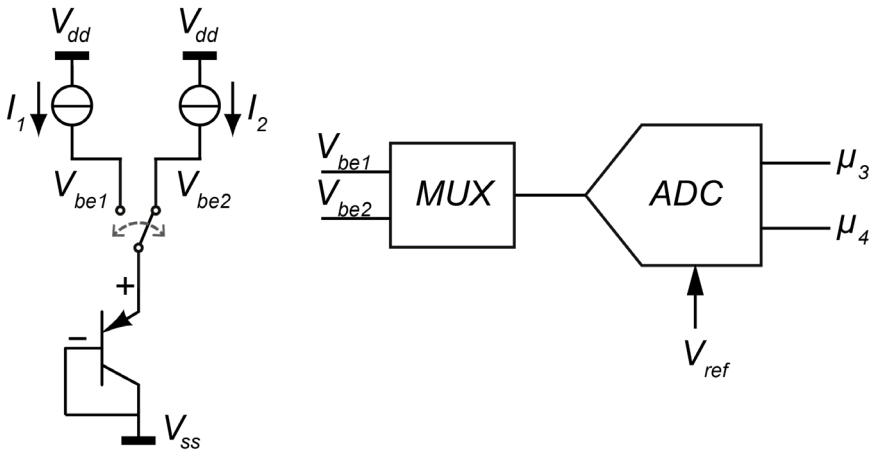


Figure 4.2. BJT front-end for algorithmic voltage measurement.

To obtain an accurate bandgap voltage reference, we use the same ADC to digitize the base-emitter voltage V_{be} of a single BJT that is successively biased at two different collector currents I_1 and I_2 , as shown in Figure 4.2:

$$V_{be1,2} = \frac{nkT}{q} \ln \left(\frac{I_{1,2}}{I_S} \right) \quad (4.9)$$

in which n is the BJT's non-ideality factor, k is Boltzmann's constant, q is the electron charge, T is absolute temperature, and I_S is the BJT's saturation current ($I_S \ll I_{1,2}$) [18]. Note that this is a simplified expression; the impact of the non-idealities of the BJT will be discussed in Section 4.2.4. These base-emitter voltages are approximately linear functions of temperature, with an extrapolated value at 0 K that is equal to the bandgap voltage of Silicon (about 1.2 V), and a negative temperature coefficient of about 2 mV/K, as illustrated in Figure 4.3 [18]. The difference of the two base-emitter voltages is a PTAT voltage that depends, to first order, only on the current ratio $p = I_1 / I_2$:

$$\Delta V_{be} = V_{be1} - V_{be2} = \frac{kT}{q} \cdot \ln(p) \quad (4.10)$$

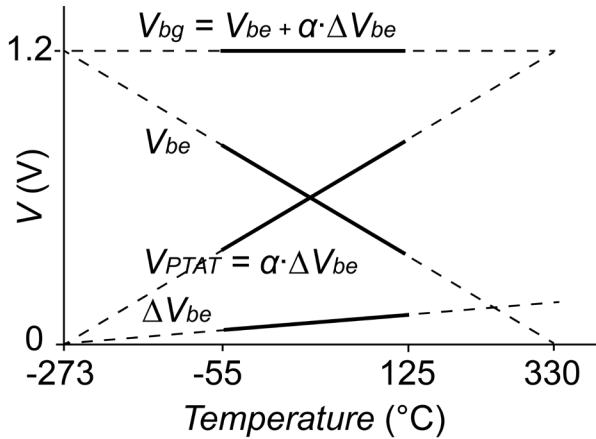


Figure 4.3. Temperature dependency of the key voltages for constructing a bandgap reference.

In a conventional bandgap reference, a temperature-independent reference voltage is obtained by adding a scaled ΔV_{be} to V_{be} :

$$V_{bg} = V_{be1} + \alpha \cdot \Delta V_{be} = a_1 V_{be1} + a_2 V_{be2}, \quad (4.11)$$

where $a_1 = 1 + \alpha$, $a_2 = -\alpha$, and the optimal coefficient α is subject to tolerances on the BJT's saturation current and collector current, and can be determined after a single-temperature calibration [8].

Rather than generating a bandgap reference voltage in the analog domain, we successively digitize $V_{be1,2}$ in two additional conversions, giving:

$$\mu_3 = \frac{V_{be1}}{V_{ref}}, \quad \mu_4 = \frac{V_{be2}}{V_{ref}}, \quad (4.12)$$

These results are then combined digitally to obtain the equivalent of (4.11):

$$V_{bg} = V_{ref} \cdot (a_1 \mu_3 + a_2 \mu_4) \quad (4.13)$$

which allows us to express the (inaccurate) analog reference of the ADC V_{ref} in terms of the (accurate) bandgap reference V_{bg} . Note that the coefficients a_1 and a_2 in (4.13) can in principle be defined with arbitrary precision, which is not possible in a conventional analog implementation.

The voltage drop across the transducer can now be found independently of V_{ref} by combining (4.1) and (4.13):

$$V_{load} = \frac{\mu_1}{a_1 \mu_3 + a_2 \mu_4} \cdot V_{bg} \quad (4.14)$$

Similarly, the power dissipated in the transducer can be found by combining (4.4) and (4.13):

$$P_{load} = \frac{\mu_1 \mu_2}{(a_1 \mu_3 + a_2 \mu_4)^2} \cdot \frac{V_{bg}^2}{R_{ref}} \quad (4.15)$$

4.2.3 Algorithmic Temperature Measurement

Expressions (4.3) and (4.15) still depend on R_{ref} , which will generally be subject to process tolerances and temperature drift:

$$R_{ref} = R_{ref0} \left\{ 1 + \alpha_{Rref} (T - T_0) \right\} \quad (4.16)$$

where R_{ref0} is the value of R_{ref} at temperature T_0 and α_{Rref} is the resistor's TCR. The

tolerances of R_{ref0} can be compensated for by a single-temperature calibration, which is done by replacing the transducer by an off-chip precision resistor in the calibration setup.

To compensate for the resistor's temperature drift, information about the die temperature T is needed. Fortunately, this can readily be obtained from the PTAT voltage given by (4.10):

$$\begin{aligned} T &= \frac{q\Delta V_{be}}{k \cdot \ln(p)} = (\mu_3 - \mu_4) \frac{qV_{ref}}{k \cdot \ln(p)} \\ &= \frac{\mu_3 - \mu_4}{a_1\mu_3 + a_2\mu_4} \cdot \frac{qV_{bg}}{k \cdot \ln(p)} \end{aligned} \quad (4.17)$$

where the relation (4.13) between V_{ref} and V_{bg} is again used to obtain an expression independent of V_{ref} . The result only depends on the current ratio p , the bandgap scale factors $a_{1,2}$, the bandgap voltage V_{bg} and physical constants k and q . The temperature reading thus obtained is substituted into (4.16) to calculate the value of R_{ref} so as to obtain a temperature-compensated resistance and power measurement.

4.2.4 Compensation of BJT Non-Idealities

As mentioned, equation (4.9) for the base-emitter voltage ignores the various non-idealities of the BJT [8]. First, the non-linear temperature dependence of I_S will lead to a (slightly) non-linear temperature dependence of V_{be} , which leads to a small non-linear temperature dependence of the bandgap reference voltage, also referred to as curvature [18]. Since it is quite deterministic, it can be corrected in the digital domain by using the temperature information obtained from (4.17).

Second, the BJT's finite current gain causes its collector current to deviate from the bias current applied to its emitter. We will assume that the BJT is operated at current levels at which its current gain is only a weak function of current level, and so this effect only causes a small gain error in the bias current that can be compensated for by using an appropriate bias circuit [19], as will be shown in Section 4.3.2.

Further non-idealities associated with the BJT can be captured by replacing (4.9) by

$$V_{be} = \frac{nkT}{q} \ln\left(\frac{pI - I_{leak}}{I_s}\right) + pIR_s \tag{4.18}$$

where the BJT is assumed to be biased at a multiple p of the bias current I , and in which I_{leak} accounts for leakage currents (including the transistor’s own saturation current), and R_s accounts for the voltage drop across the BJT’s emitter (series) resistance, as illustrated in Figure 4.4. Leakage current and series resistance lead to errors in the bandgap reference and the temperature measurement that cannot be corrected by a single-temperature calibration [7]. However, they can be made negligible by appropriately choosing the bias current level.

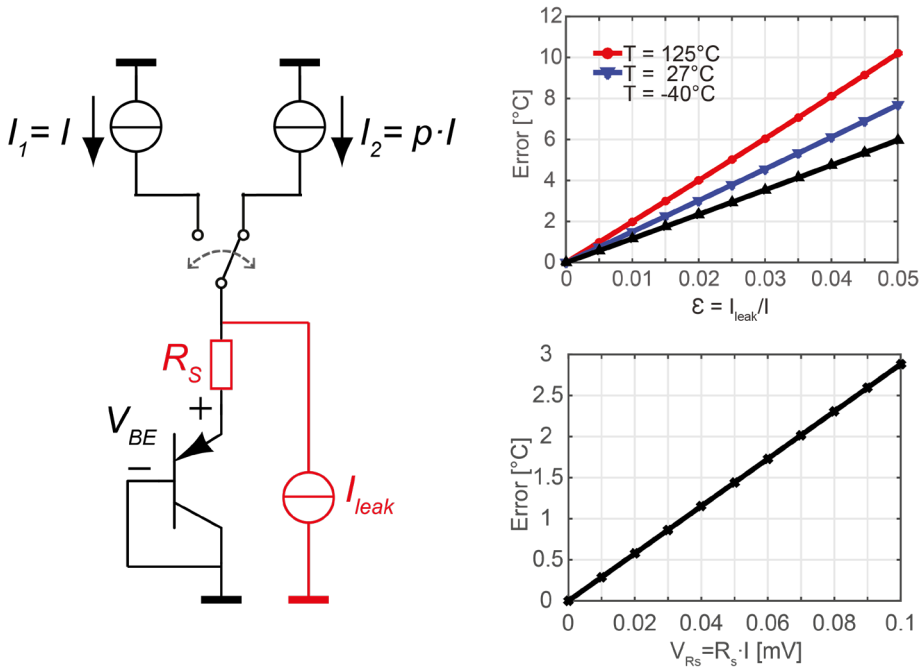


Figure 4.4. (a) BJT front-end with series resistance R_s and leakage current I_{leak} ; (b) temperature errors due to I_{leak} ; (c) temperature errors due to R_s .

Our algorithmic approach offers the unique possibility to correct for leakage and series resistance by combining more than two base-emitter voltages digitally. Equation (4.18) can be rewritten as:

$$V_{be} = V_{be,ideal} + \Delta V_{be,ideal} \frac{\ln(p - I_{leak} / I_S)}{\ln(p)} + pIR_s \quad (4.19)$$

where $V_{be,ideal}$ and $\Delta V_{be,ideal}$ are the ideal voltages given by (4.9) and (4.10). From the base-emitter voltages measured at a minimum of four different values of p , $V_{be,ideal}$ and $\Delta V_{be,ideal}$ can be found by curve fitting to (4.19). These values can then be used, as before, to construct the voltage reference and measure temperature, without errors due to series resistance or leakage current.

4.3 Circuit Implementation

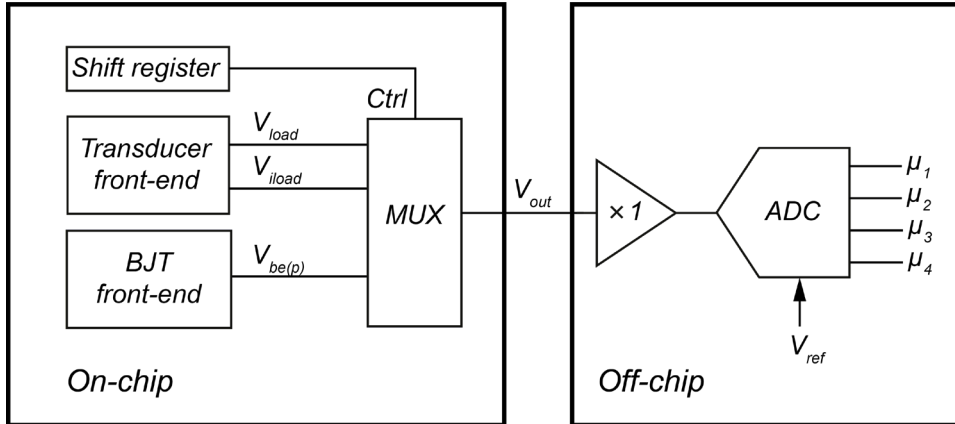


Figure 4.5. Block diagram of the entire readout circuit (on-chip and off-chip).

The block diagram of the readout circuit is shown in Figure 4.5. The on-chip circuits, including the transducer front-end for resistance and power measurement, the BJT front-end for the construction of the algorithmic voltage reference and temperature sensor, and the multiplexer to select the desired voltage for measurement, have been designed and fabricated in a 0.16 μm CMOS technology.

Since the algorithmic readout relies on the accuracy and resolution of the ADC, its non-idealities must be taken into account when selecting or designing the ADC. First, the ADC's quantization noise and thermal noise should be non-dominant compared with the noise from the front-end circuits. Second, the non-

Chopping is mainly applied to reduce the impact of the amplifier's $1/f$ noise on the measurement.

Compared with Figure 4.1, an additional cascode transistor M_{0b} is added. Simulation shows that leakage current due to Hot Carrier Injection to the bulk of the transistor M_{0a} becomes non-negligible when the supply voltage increases 10% above its nominal value (1.8 V). This is because some of the carriers (electrons and holes) in the channel are excited by the high drain-source electric field and escape into the substrate. The added cascode transistor M_{0b} decreases the drain-source voltage of the main transistor M_{0a} , effectively reducing this leakage current. The capacitor C_1 helps to stabilize the feedback loop and also reduces the output integrated noise contributed by the OTA.

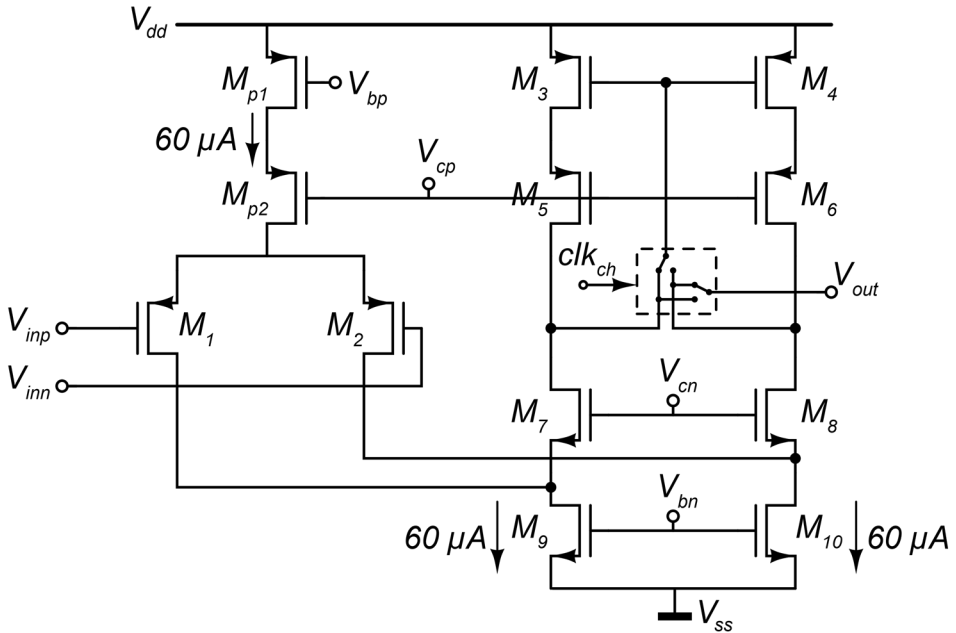


Figure 4.7. Schematic of the operational transconductance amplifier (OTA) used in both bandgap core and transducer front-end.

Figure 4.7 shows the schematic of the OTA, which is a PMOS-input, folded-cascode amplifier. PMOS transistors are chosen for the input pair as the voltage across the transducer is relatively low (about 0.3 V). The output chopper switch is integrated in the output current mirror.

4.3.2 Circuit Implementation of the BJT Front-End

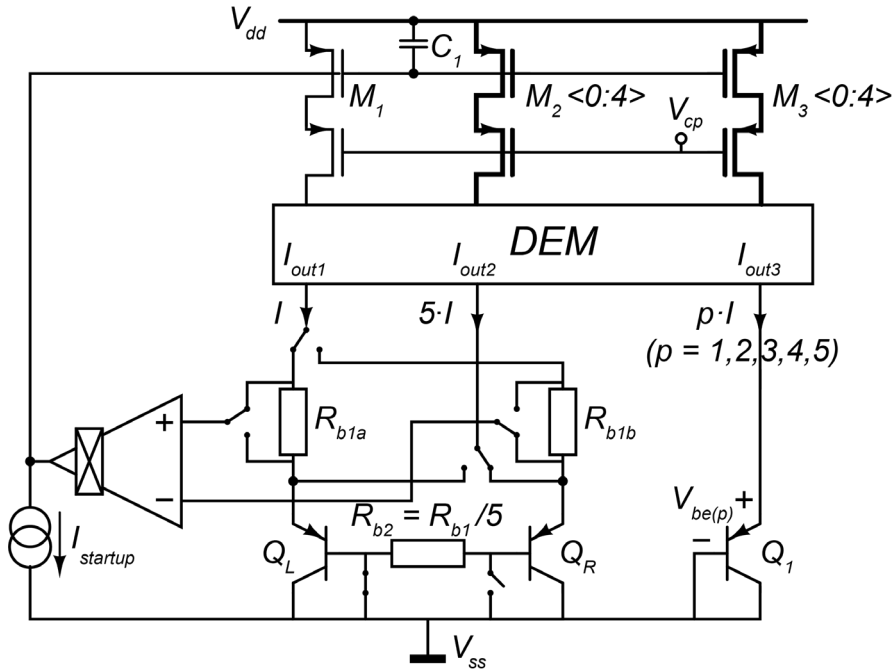


Figure 4.8. Circuit diagram of the proposed bandgap core including bias generation.

The BJT front-end circuit shown in Figure 4.8 generates the base-emitter voltages needed for the construction of the voltage reference and temperature sensor. A PTAT bias generation circuit is used to provide a well-defined bias current that is an integer multiple p of a unit bias current of nominally $6 \mu\text{A}$ [18]. Resistor R_{b2} is used to remove the current-gain dependence of the base-emitter voltage by making the generated bias current dependent on the base current in such a way that the collector current of Q_1 is PTAT and independent of the current gain, provided the current gains of Q_1 , Q_L and Q_R are matched [19].

The OTA used in the BJT front-end is the same as the one used in the transducer front-end (as shown in Figure 4.7). It needs to have low offset and high open-loop gain to minimize errors in the bias current [19]. As before, this is

achieved by chopping and the use of a folded-cascode topology that achieves more than 60 dB open-loop gain over all corners.

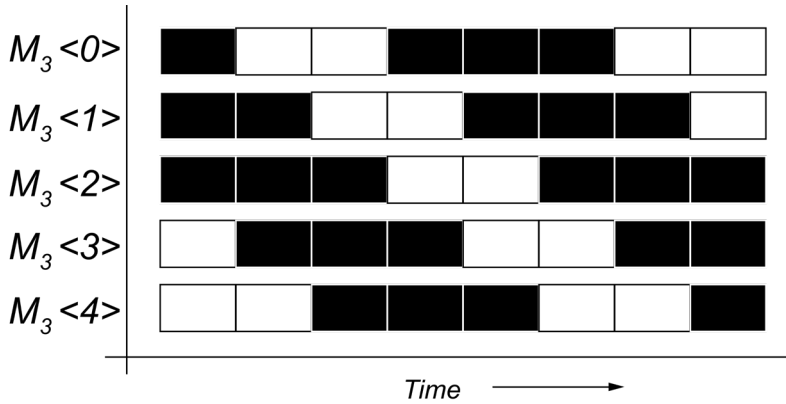


Figure 4.9. DEM algorithm ($p = 3$ current sources are selected in this example).

As indicated in (4.10), an accurate PTAT voltage ΔV_{be} requires a well-defined current ratio p that is stable over time and temperature. This is achieved by applying dynamic element matching (DEM) to the current mirror shown in Figure 4.8. The DEM algorithm is illustrated in Figure 4.9. To generate a current of p times the unit bias current I , p unit current sources are selected in every DEM step and then shifted in a cyclic manner during successive DEM steps. Thus, the mismatch of the current sources is modulated by the DEM clock, and the resulting average current is close to p times the average unit current. Since the following signal processing is done by an oversampled ADC, the voltage ripple associated with the modulated current mismatches is averaged out by the digital filtering of the ADC.

4.4 Experimental Results and Discussion

The layout (highlighting the main circuit blocks) and micrograph of the chip are shown in Figure 4.10. A block diagram of the experimental setup is shown in Figure 4.11. The chip (DUT), mounted on a PCB (PCB_1), is placed inside a climate chamber (Vötsch VTM 7004) and characterized over a -40°C to 125°C temperature range. A Pt100 resistive temperature detector with a nominal resistance of $100\ \Omega$ at

0 °C and a temperature coefficient of 0.39%/K, is used as the transducer (R_{load}), whose resistance and power dissipation are to be measured. For calibration purposes, a switch allows R_{load} to be replaced by a precision resistor $R_{loadREF}$. Another Pt100 resistor is used as a reference temperature sensor (T_{REF}). A second PCB (PCB₂) with the ADC [20] is placed outside the oven. Control signals for the on-chip MUX and DEM switches and the ADC are generated by an FPGA, and the ADC's output data is transferred to a PC via an RS-232 connection and processed in MATLAB. A precision multimeter (Keithley 2002) is used to measure the resistance of the transducer and the voltage drop across the transducer when it is biased by the chip, so that power dissipation of the transducer can be independently determined for comparison.

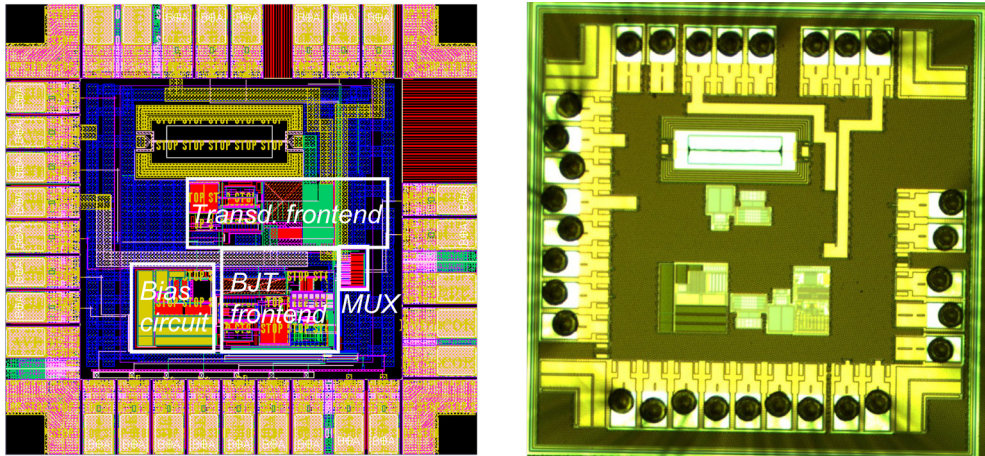


Figure 4.10. Chip layout and micrograph.

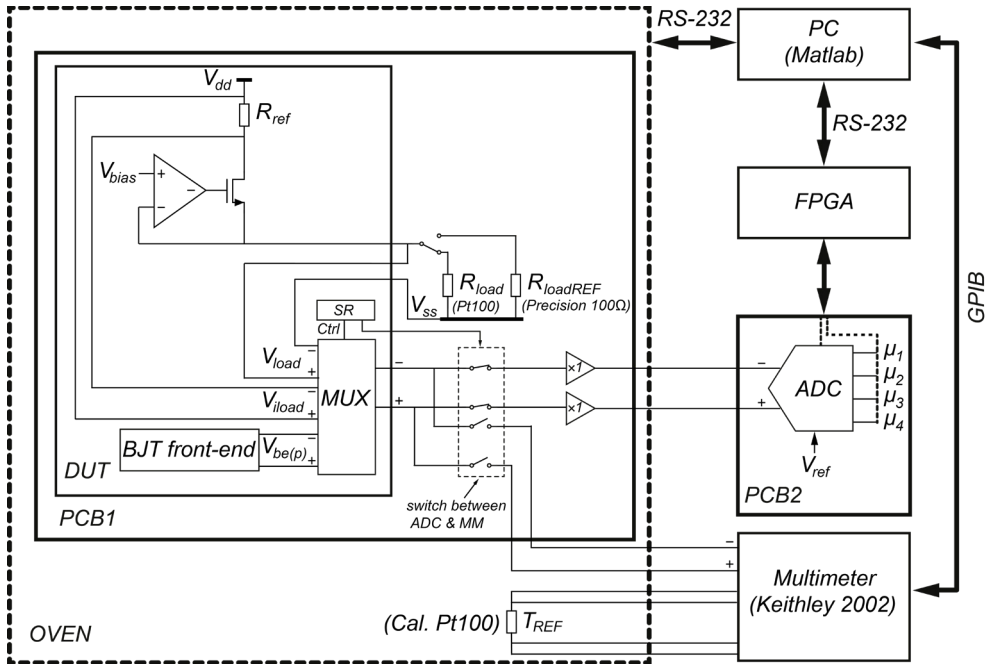


Figure 4.11. Experimental setup.

4.4.1 Voltage Reference

To evaluate the accuracy of the algorithmic voltage reference, the digitized base-emitter voltages as well as the voltage drop across the transducer V_{load} were measured sequentially by the ADC, and the value of V_{load} was calculated relative to the algorithmic voltage reference using (4.14), including compensation for series resistance, leakage and curvature using the techniques described in Section 4.2.4. Figure 4.12 compares the result, for 5 samples of the chip, with a direct measurement of V_{load} using the precision multimeter. The results show good agreement, with errors below ± 1.1 mV.

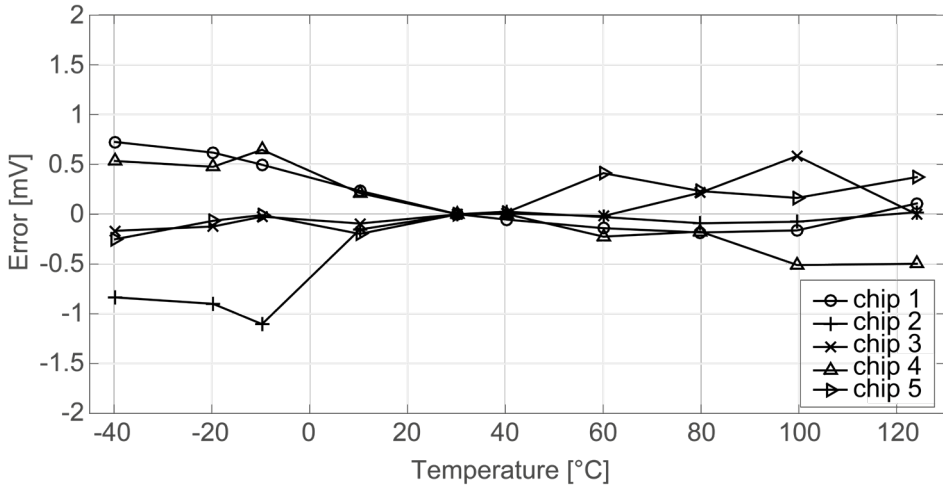
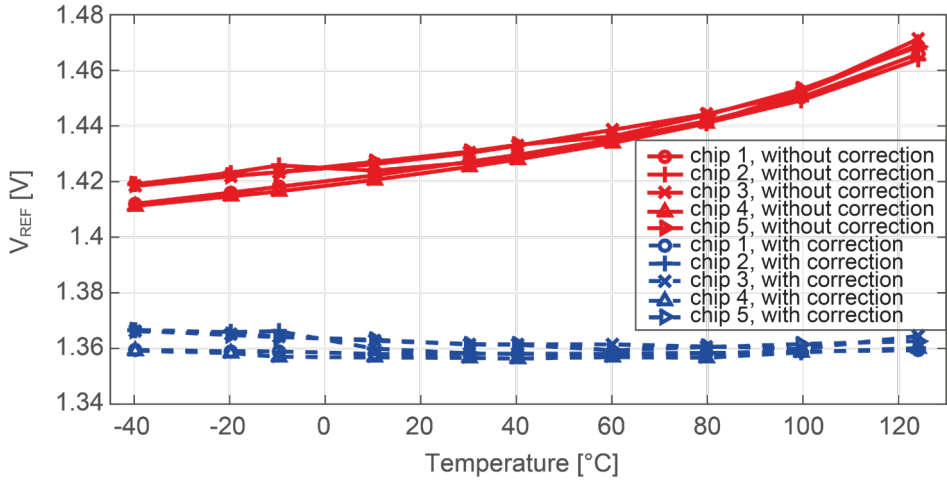


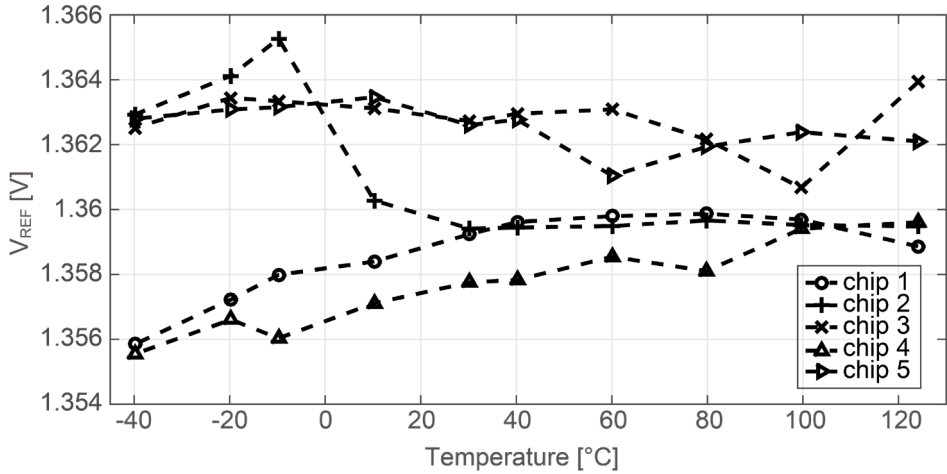
Figure 4.12. Measured voltage error of the transducer by the algorithmic reference voltage (compared with the measurements by the multimeter).

To obtain the result shown in Figure 4.12, the value of V_{bg} in (4.13) was determined iteratively so as to obtain the smallest temperature dependence. This is a batch calibration [8], leading to an optimum value of V_{bg} that is the same for all samples. To correct for the sample-to-sample spread of the base-emitter voltages, the optimum values of the coefficients a_1 and a_2 in (4.13) were determined by calibrating each sample at room temperature (27°C). This is done by adjusting the coefficients a_1 and a_2 such that the calculated V_{load} is equal to the value measured by the precision multimeter at room temperature.

From the same data set, the value of the algorithmic reference voltage is calculated using (4.13), where the value of the ADC’s reference voltage V_{ref} is obtained from (4.1), by dividing the value of V_{load} as measured using the precision multimeter by μ_1 . The result is shown in Figure 4.13. To illustrate the impact of the series resistance, leakage current and curvature, results are shown with and without compensation for these non-idealities. The temperature coefficient without compensation for any of these non-idealities is about 220 ppm/°C, mainly due to the impact of leakage current, which is rather large in our design due to the sizing of the MOS transistors in the on-chip multiplexer. This improves to about 24 ppm/°C after compensation for series resistance and leakage using the method described in Section 4.2.4. After compensation for the systematic quadratic curvature, a further improvement to 18 ppm/°C is achieved (Figure 4.13b).



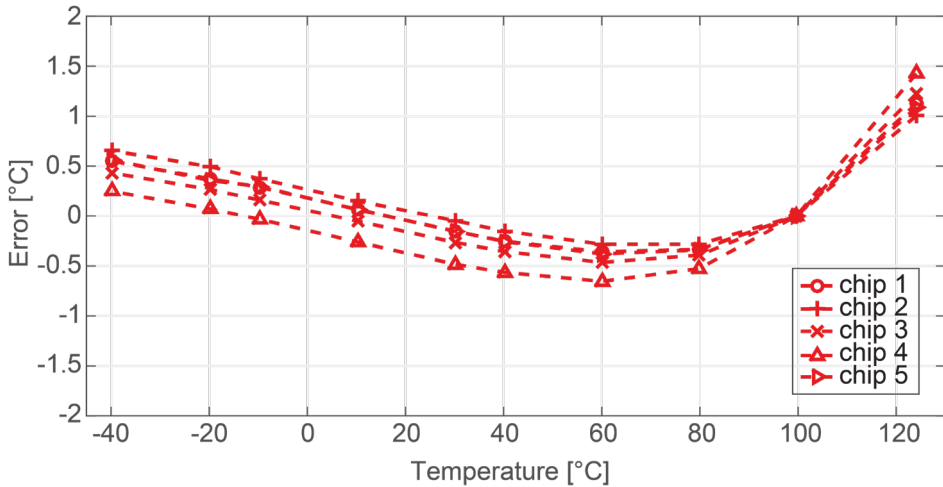
(a)



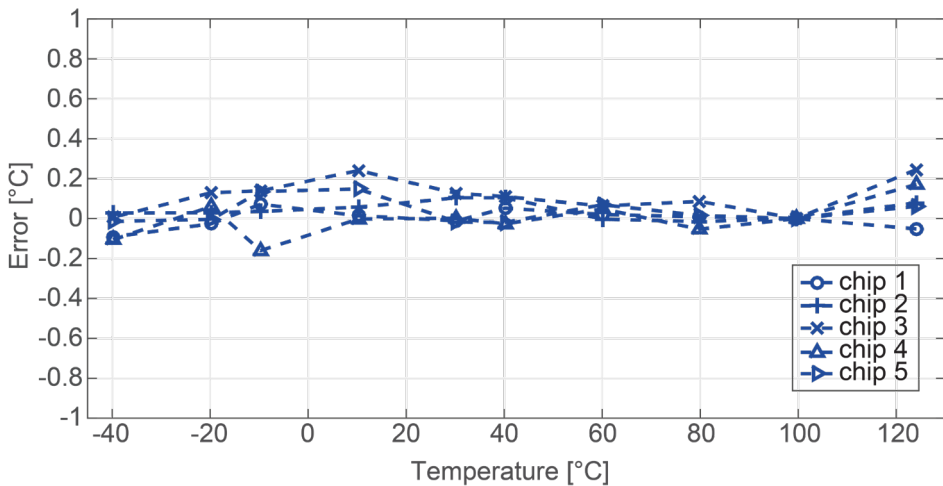
(b)

Figure 4.13. Algorithmic reference voltage (a) without and with compensation and correction for series resistance and leakage; (b) with compensation and correction for series resistance and leakage as well as curvature.

4.4.2 Temperature Measurement



(a)



(b)

Figure 4.14. Measured temperature error of the algorithmic temperature sensor (a) without and (b) with correction for leakage and series resistance.

Figure 4.14 shows the error in the temperature measured using the method described in Section 4.2.3, relative to the reference temperature sensor, for 5 samples of the chip. When ΔV_{be} is directly measured without any compensation, significant errors occur at high temperatures due to leakage currents of the

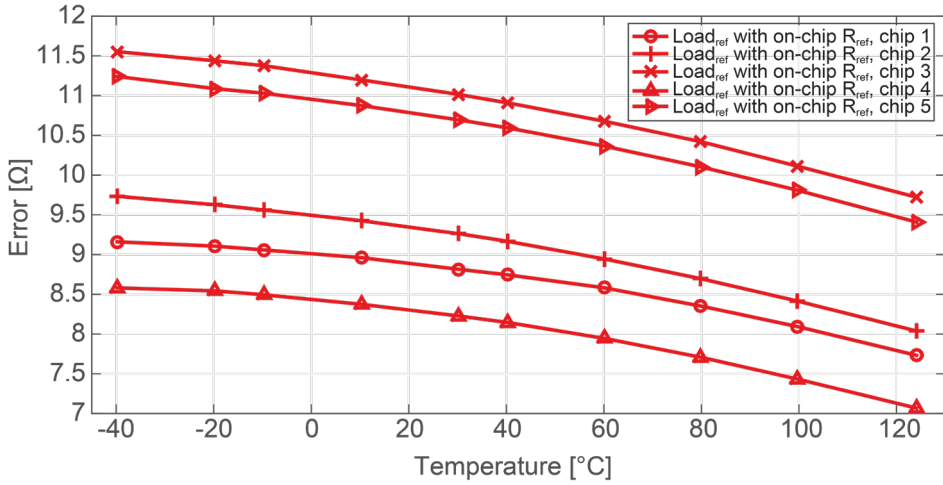
multiplexer switches (up to 180 nA in this design). By applying the algorithmic approach described by (4.17) and (4.18), a leakage-free PTAT voltage $\Delta V_{be,ideal}$ can be obtained, which can then be converted to temperature by linear scaling. Thus, the residual errors are reduced to $\pm 0.25^\circ\text{C}$ (min-max) after a 1-point trim at 100°C (Figure 4.14b). The trimming, to cancel the PTAT error due to V_{be} spread, was done in the digital domain [8]. These errors are relatively large compared to the state of the art [19], which can be attributed to the large initial errors caused by the leakage currents of the large multiplexer switches (i.e. $50\ \mu\text{m}$ in width), which can be reduced in a re-design by reducing the transistor sizes.

4.4.3 Resistance Measurement

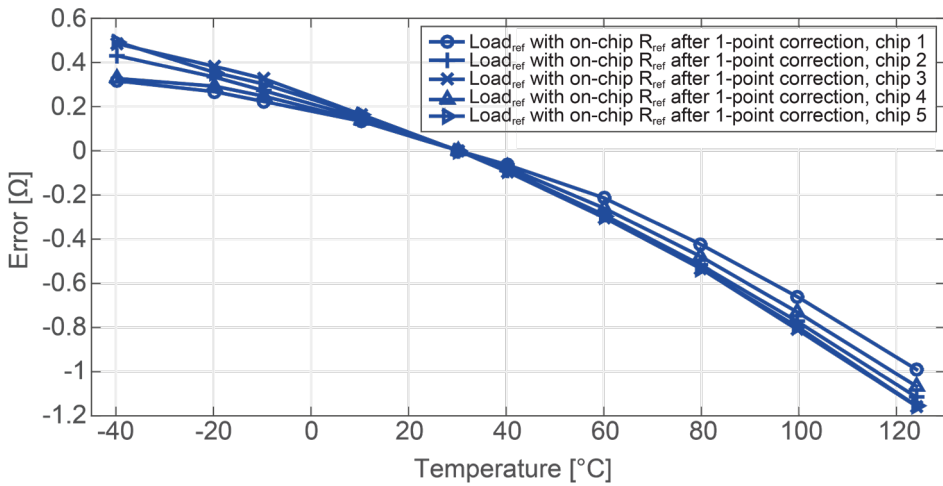
As described in II-A, the resistance of the transducer is measured relative to an on-chip reference resistor R_{ref} in series with the transducer (Figure 4.6). Since R_{ref} is subject to process tolerances, it is first calibrated by connecting a precision resistor ($R_{loadREF}$ in Figure 4.11) instead of the transducer. Figure 4.15a shows the error in the measured resistance of this precision resistor as a function of temperature relative to the resistance measured using the precision multi-meter.

First, a one-point correction is performed by using the error at 27°C to determine the nominal resistance of R_{ref} , i.e. R_{ref0} in eq. (4.16), while assuming its temperature coefficient $\alpha_{R_{ref}}$ is zero. The error in the measurement of the precision resistor then reduces significantly, as shown in Figure 4.15b. The resistance of the Pt100 is then measured using this same correction. The error in this measurement relative to the multimeter is less than $\pm 1.6\ \Omega$, as shown in Figure 4.16a. A substantial temperature drift is observed due to the fact that the temperature dependence of R_{ref} is not compensated for.

Second, the temperature coefficient $\alpha_{R_{ref}}$ is determined by a two-point batch correction (at 27°C and 100°C) in the calibration result of Figure 4.15a. When measuring the Pt100, these coefficients and the temperature information obtained from the algorithmic temperature measurement are used to compensate for the temperature dependence of R_{ref} , as discussed in Section 4.2.3. This reduces the error to less than $\pm 0.55\ \Omega$, as shown in Figure 4.16b. A further reduction could be achieved by also compensating for the higher-order temperature dependence of R_{ref} .

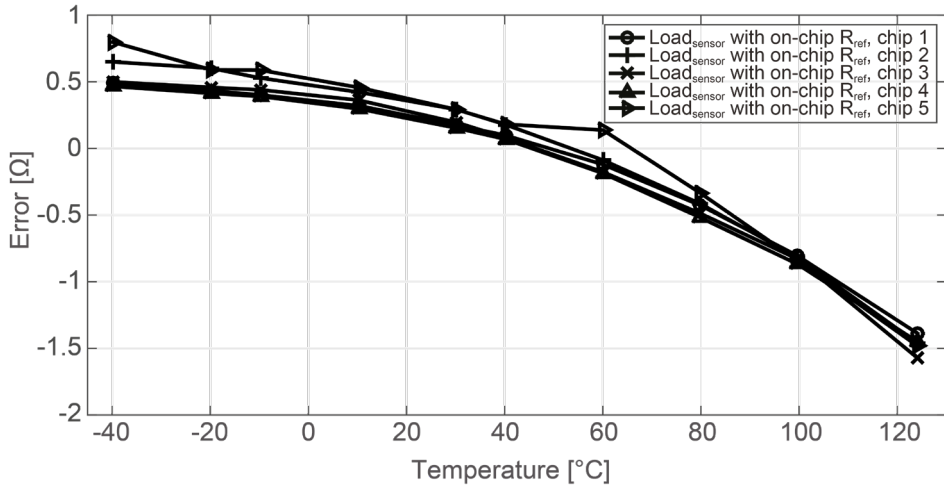


(a)

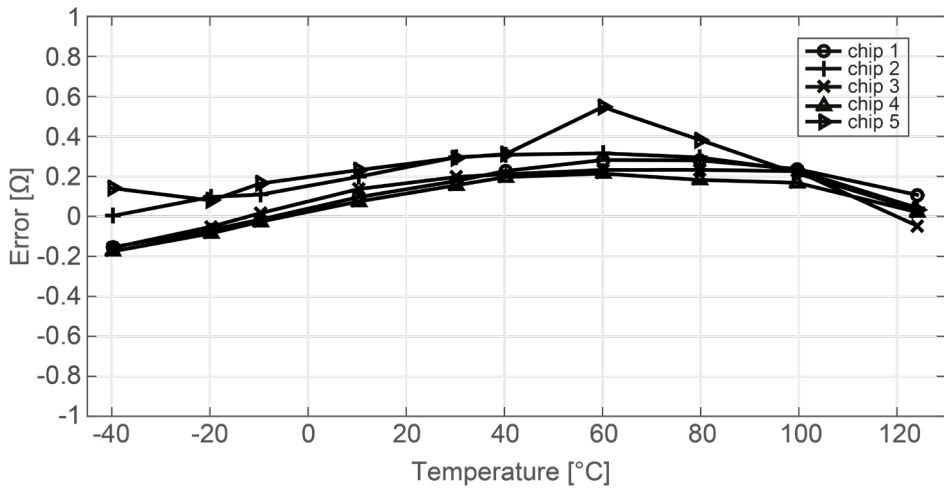


(b)

Figure 4.15. Measured resistance error of a precision resistor as a function of temperature; (a) without calibration; (b) with calibration and correction at one-temperature point (27 $^{\circ}\text{C}$).



(a)

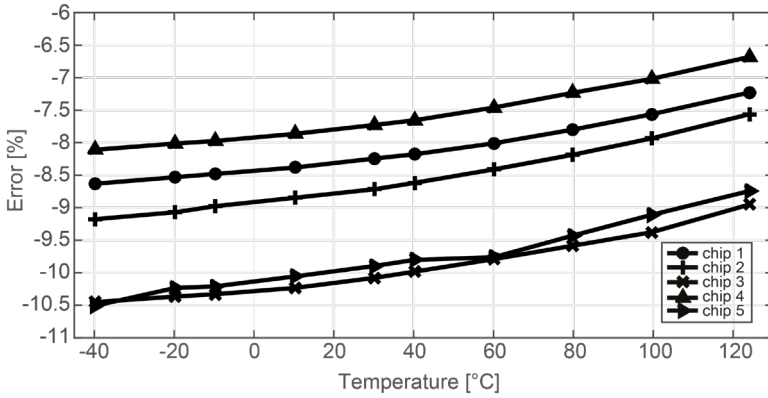


(b)

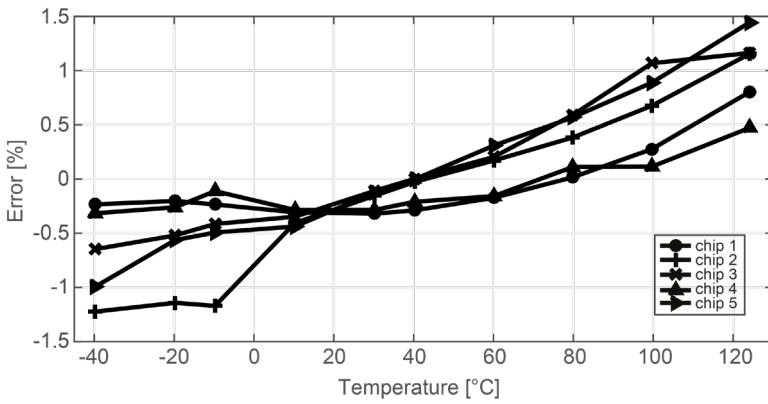
Figure 4.16. Measured resistance error of the Pt100 sensor resistor as a function of temperature; (a) with calibration and correction at one-temperature point (27°C); (b) with calibration and correction at two-temperature points (27°C and 100°C).

4.4.4 Power Measurement

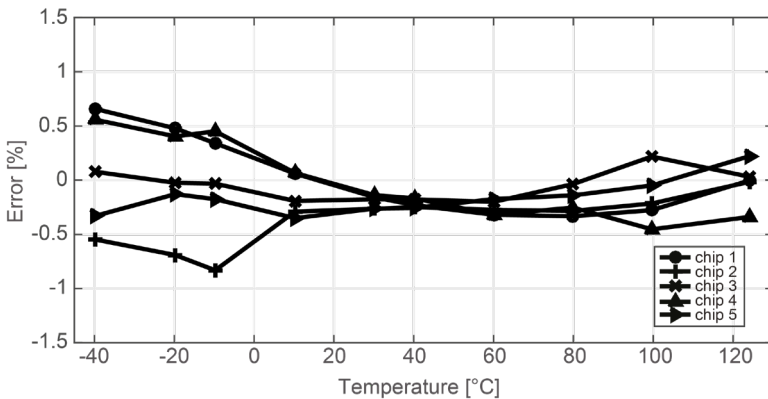
The power consumption of the transducer was measured using the method described in Section 4.2, eq. (4.15). Figure 4.17a shows the results of the power dissipation in the transducer without compensating for the tolerance and temperature drift of the on-chip reference resistor R_{ref} , and Figure 4.17b shows the results when a one-point calibration at 27°C is performed to compensate for spread in the nominal resistance of R_{ref} , i.e. R_{ref0} in eq. (4.16), in a similar way as described above. With this calibration, the errors are less than $\pm 1.5\%$. As described above, the accuracy of the on-chip reference resistance can be further improved by a room-temperature individual trim and a two-point batch calibration (27°C and 100°C) to find R_{ref0} and α_{Rref} . This reduces the errors in the power dissipation measurement to $\pm 0.8\%$ as shown in Figure 4.17c.



(a)



(b)



(c)

Figure 4.17. Measured power error as a function of temperature; (a) without calibration; (b) with 1-point calibration and correction of the resistance measurement; (c) with 2-point calibration and correction of the resistance measurement.

4.4.5 Equivalent Error in Thermal Resistance

As this readout has not been used for TC sensors, data for CO₂ measurements are not available. However, the equivalent measurement error of thermal resistance (and thus CO₂ concentration), can be estimated by substituting the measurement errors of temperature, resistance and power into (4.8). The equivalent error of thermal resistance over the military temperature range is about 1.8%, which could be reduced to about 3000 ppm within the indoor temperature range (10°C – 40°C) [23]. This translates to a CO₂ accuracy of about 7500 ppm (assuming a 200-ppm change in CO₂ leads to an 80-ppm change in TC). The error was mainly contributed by the temperature measurement. Further improvement in temperature accuracy can also reduce errors in resistance and power measurements.

4.5 Conclusions

Table 4.1. Performance Summary

Temperature range	-40°C – 125°C
Temperature inaccuracy	±0.25°C (min-max)
Temperature dependence of voltage reference	18 ppm/°C
Resistance inaccuracy	±0.55 Ω [†]
Power inaccuracy	±0.8% [†]

[†]after a single temperature calibration for the on-chip reference resistor, 5 samples.

In this chapter, we have reported a readout architecture for resistive transducers, which is capable of accurately measuring their resistance and power dissipation. Its performance is summarized in Table 4.1. The key idea is to avoid analog signal processing as much as possible, by first digitizing the analog signals and then combining the results in the digital domain. This algorithmic approach greatly improves the flexibility of the signal processing and facilitates the removal of errors such as leakage current, series resistance, and systematic nonlinearity in the digital domain. In addition, the accuracy of the analog reference voltage of the ADC does not impact the measurement accuracy, as it is replaced by an algorithmically constructed bandgap reference voltage in further data processing. Experimental results have shown that the resistance and power dissipation of a

Pt100 resistor can be measured with inaccuracies of $\pm 0.55 \Omega$ and $\pm 0.8\%$, respectively, from -40°C to 125°C , showing the effectiveness of the applied techniques. The algorithmic bandgap reference and temperature sensor achieve performance that approaches the state-of-the-art. Although our proof-of-concept prototype uses an off-chip ADC, making it more costly and power hungry than previous solutions, suitable ADCs implemented in standard CMOS technology have been reported [21], which can readily be co-integrated to realize a fully-integrated low-cost solution. The ability to accurately measure the resistance and power dissipation of a resistive transducer as well as ambient temperature makes this readout architecture well-suited, for instance, to the interfacing of TC-based gas sensors.

References

- [1] N. Tadic, M. Zogovic, and D. Gobovic, "A CMOS controllable constant-power source for variable resistive loads using resistive mirror with large load resistance dynamic range," *IEEE Sensors J.*, vol. 14, pp. 1988-1996, Jun. 2014.
- [2] S. Chan and P. C. Chan, "A resistance-variation-tolerant constant-power heating circuit for integrated sensor applications," *IEEE J. Solid-State Circuits*, vol. 34, no. 4, pp. 432-439, Apr. 1999.
- [3] C.A. Leme, R. Lenggenhager, I. Filanovsky, H. Baltes, "Linear CMOS power controller for precision sensor applications," in *Proc. IEEE Int. Symp. Circuits Syst.*, 1992, pp. 1844-1846.
- [4] D. F. Hilbiber, "A new semiconductor voltage standard," in *Dig. Techn. Papers ISSCC*, Feb. 1964, pp. 32-33.
- [5] G. Maderbacher et al., "A digitally assisted single-point-calibration CMOS bandgap voltage reference with a 3σ inaccuracy of $\pm 0.08\%$ for fuel-gauge applications," in *Dig. Techn. Papers ISSCC*, Feb. 2015, pp. 102-103.
- [6] C. M. Andreou, S. Koudounas and J. Georgiou, "A novel wide-temperature-range, $3.9 \text{ ppm}/^\circ\text{C}$ CMOS bandgap reference circuit," *IEEE J. Solid-State Circuits*, vol. 47, no. 2, pp. 574-581, Feb. 2012.
- [7] G. Ge, et al., "A single-trim CMOS bandgap reference with a 3σ inaccuracy of $\pm 0.15\%$ from -40°C to 125°C ," *IEEE J. Solid-State Circuits*, vol. 46, no. 11, pp. 2693-2701, Nov. 2011.
- [8] M. A. P. Pertijs and J. H. Huijsing, *Precision Temperature Sensors in CMOS Technology*. Dordrecht, The Netherlands: Springer-Verlag, 2006.

- [9] S. H. Shalmany, D. Draxelmayr and K. A. A. Makinwa, "A ± 5 A integrated current-sensing system with $\pm 0.3\%$ gain error and 16 μA offset from -55°C to $+85^\circ\text{C}$," *IEEE J. Solid-State Circuits*, vol. 51, no. 4, pp. 800-808, Apr. 2016.
- [10] N. Saputra, M. A. P. Pertijs, K. A. A. Makinwa and J. H. Huijsing, "Sigma delta ADC with a dynamic reference for accurate temperature and voltage sensing," in *Proc. IEEE Int. Symp. Circuits Syst.*, 2008, pp. 1208-1211.
- [11] M. de Wit, "Temperature independent resistor," U.S. Patent 5,448,103, Sep. 5, 1995.
- [12] B. R. Gregoire and U. K. Moon, "Process-independent resistor temperature-coefficients using series/parallel and parallel/series composite resistors," in *Proc. IEEE Int. Symp. Circuits Syst.*, 2007, pp. 2826-2829.
- [13] G. Serrano and P. Hasler, "A precision low-TC wide-range CMOS current reference," *IEEE J. Solid-State Circuits*, vol. 43, no. 2, pp. 558-565, Feb. 2008.
- [14] B. R. Gregoire and U. K. Moon, "A sub 1-V constant Gm-C switched-capacitor current source," *IEEE Trans. Circuits Syst. II*, vol. 54, no. 3, pp. 222-226, Mar. 2007.
- [15] M. H. Perrott et al., "A temperature-to-digital converter for a MEMS-based programmable oscillator with $<\pm 0.5$ ppm frequency stability and <1 -ps integrated jitter," *IEEE J. Solid-State Circuits*, vol. 48, no. 1, pp. 276 - 291, Jan. 2013.
- [16] M. Choi, et al., "A 99nW 70.4kHz resistive frequency locking on-chip oscillator with 27.4 ppm/ $^\circ\text{C}$ temperature stability," in *2015 Symposium on VLSI Circuits (VLSI Circuits) Digest of Technical Papers*, Kyoto, 2015, pp. C238-C239.
- [17] D. Griffith, P. T. Roine, J. Murdock and R. Smith, "A 190nW 33kHz RC oscillator with $\pm 0.21\%$ temperature stability and 4ppm long-term stability," in *Dig. Techn. Papers ISSCC*, Feb. 2014, pp. 300-301.
- [18] G. Meijer, "Thermal sensors based on transistors," *Sens. Actuators*, vol. 10, no. 1, pp. 103-125, 1986.
- [19] M. A. P. Pertijs, K. A. A. Makinwa, and J. H. Huijsing, "A CMOS smart temperature sensor with a 3σ inaccuracy of $\pm 0.1^\circ\text{C}$ from -55°C to 125°C ," *IEEE J. Solid-State Circuits*, vol. 40, no. 12, pp. 2805-2815, Dec. 2005.
- [20] Texas Instruments. ADS1232 Datasheet. [Online]. Available: <http://www.ti.com/>.
- [21] Y. Chae, K. Souri, and K. Makinwa, "A 6.3 μW 20 bit incremental zoom-ADC with 6ppm INL and 1 μV offset," *IEEE J. Solid-State Circuits*, vol. 48, no. 12, pp. 3019-3027, Dec. 2013.
- [22] Analog Devices. AD8629 Datasheet. [Online]. Available: <http://www.analog.com/>
- [23] L. Rueda Guerrero, "An algorithmic readout approach for thermal conductivity based CO_2 sensors," M.Sc. thesis. Delft University of Technology, 2014.

Chapter 5

TIME-DOMAIN READOUT

This chapter is based on the publication “A Phase-Domain Readout Circuit for a CMOS-Compatible Hot-Wire CO₂ Sensor,” in IEEE Journal of Solid State Circuits, vol. 53, no. 11, pp. 3303-3313, Nov. 2018.

5.1 Introduction

Sensing thermal conductivity (TC) conventionally requires a steady-state measurement of a transducer’s TC-dependent thermal resistance to ambient (R_{th}). Alternatively, TC can also be derived from a transient measurement of the transducer’s thermal time constant τ_{th} , i.e. the product of its R_{th} and its thermal capacitance (C_{th}), since these both depend on the TC of the surrounding air [1][2][3]. Compared to measuring R_{th} , measuring τ_{th} has the important advantage that it only requires a time reference, and hence absolute temperature and power levels do not need to be accurately stabilized or measured. In prior work, τ_{th} was determined by periodically generating heat pulses in a resistive transducer, and then measuring the phase shift of the temperature transients with a separate temperature sensor: either a similar transducer [2] or a thermopile [4][5]. In these designs, the heating and sensing elements are separate devices, and hence the thermal signal to be sensed is naturally separated from the electrical driving signal, which simplifies the process of signal conditioning. However, this inevitably results in a more complex fabrication process, in contrast with the use of simple CMOS-compatible single-wire transducers [6].

In this chapter, we present a readout circuit that allows the functions of heating and temperature-sensing to be combined in a single resistive transducer [7][8]. This greatly simplifies fabrication, since only a single extra etch step is required to realize a tungsten hot-wire transducer in the via layer of a standard CMOS process [6]. The readout circuit is based on a continuous-time phase-domain $\Delta\Sigma$ modulator (PD $\Delta\Sigma$ M), thus circumventing the kT/C noise limitations associated with switched-

capacitor readout circuits. To reduce the required dynamic range of the modulator, the large transients associated with the periodic heating pulses, and the offset associated with the baseline resistance of the resistive transducer are canceled by employing two transducers in a novel bridge-type architecture. Experimental results show that the proposed CO₂ sensor achieves a resolution of 94 ppm in a conversion time of 1.8 s while dissipating only 12 mJ per measurement, or 2× more resolution than the state-of-the-art [6], at an energy consumption that is >10× lower.

The chapter is organized as follows. In Section 5.2, the operation of transient thermal-conductivity sensing is presented, followed by a review of the principles of phase-domain $\Delta\Sigma$ modulation. Section 5.3 is devoted to the circuit implementation of the readout circuit, including the design of the PD $\Delta\Sigma$ M and the techniques used to reduce its dynamic range requirements. Experimental results and discussions are presented in Section 5.4, and the chapter concludes in Section 5.5.

5.2 Operating Principle

5.2.1 Time-Domain Thermal-Conductivity Sensing

The measurement principle of transient TC measurement is shown in Figure 5.1. A hot-wire transducer is driven by a current pulse I_d at a frequency f_{drive} , and is thus periodically heated, however, the resulting temperature transients are delayed relative to the driving pulses. The delay is determined by the thermal time constant τ_{th} , which in turn depends on the TC of the surrounding air (Figure 5.1).

Such a TC sensor can be modeled as a first-order low-pass filter. Using a fixed driving frequency will then result in phase-delayed temperature transients relative to the driving pulses, from which τ_{th} can be derived. The optimal driving frequency equals the filter's pole frequency, i.e. $1/2\pi\tau_{th}$, at which the sensitivity of the filter's phase shift to the changes of τ_{th} is maximal. For our devices, $\tau_{th} \approx 17 \mu\text{s}$, leading to an optimal f_{drive} around 9-10 kHz.

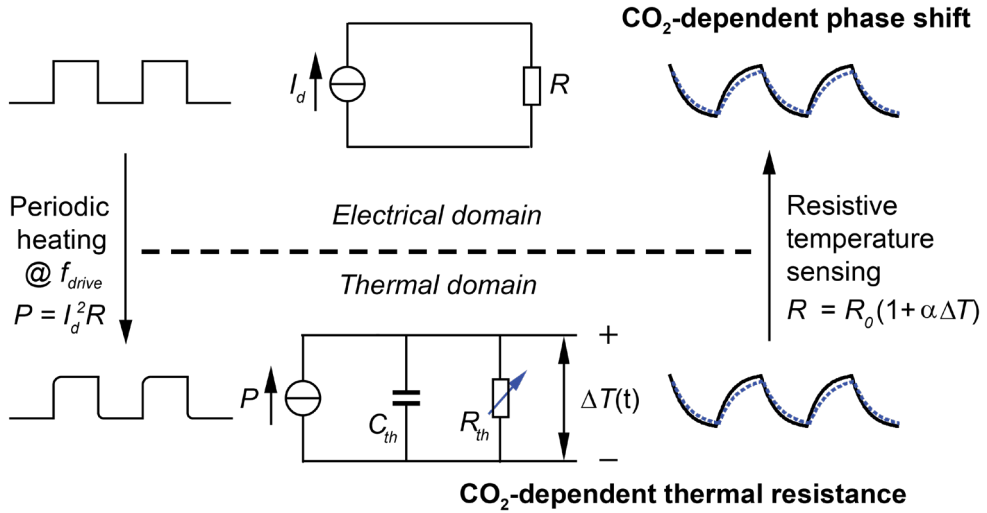
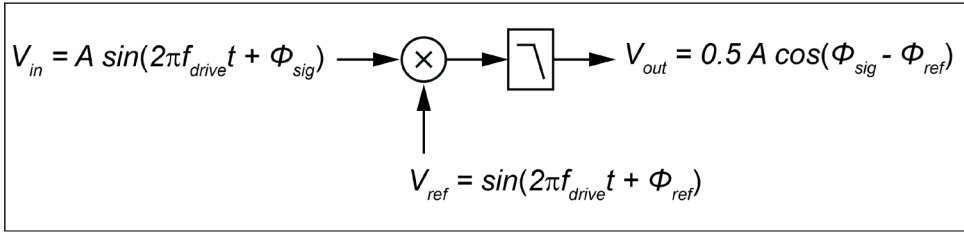


Figure 5.1. Transient thermal-resistance (thermal delay) measurement principle.

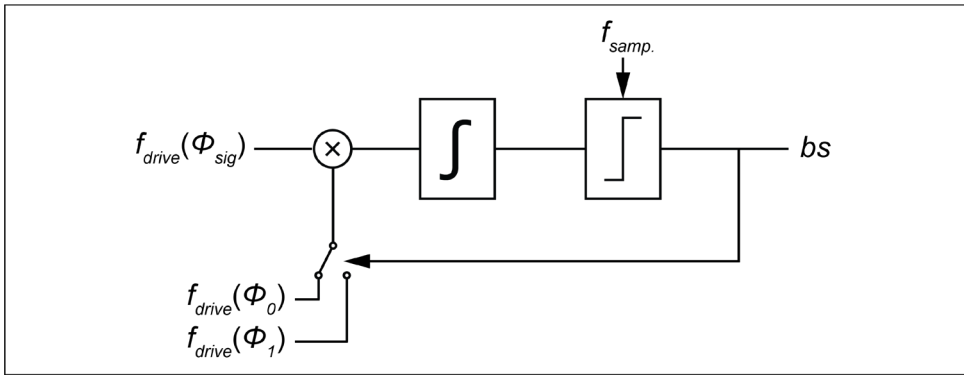
Both sine waves [2] and square waves [4] can be used to drive the heater. In terms of circuit implementation, a square wave is much easier to generate than a sine wave. The advantage of a sine wave is that it has no harmonics, and thus the phase shift of the temperature signal can be determined by filtering and zero-crossing detection [2]. In contrast, a square-wave consists of a series of harmonics. In this case, the phase shift of the fundamental can best be detected by synchronous detection [4]. By employing a synchronous detector as the summing node of a delta-sigma modulator, a phase-domain delta-sigma modulator (PD $\Delta\Sigma$ M) can be realized with which this phase shift can be digitized with high resolution [9][10].

Since resistive transducers can be used both as a heater and a temperature sensor, the heating and sensing functions can, in principle, be combined in a single resistor, provided an appropriate readout scheme is devised. This will be discussed in Section 5.3.1.

5.2.2 Phase-Domain Delta-Sigma Modulator



(a)



(b)

Figure 5.2. (a) Phase detection by means of synchronous detection. (b) Phase detection using a delta-sigma feedback loop.

When driven at f_{drive} , the phase shift ϕ_{sig} of the transducer’s temperature transients can be found by synchronous detection, i.e. by multiplying the transients by a reference signal at the same frequency and with a phase ϕ_{ref} , as illustrated in Figure 5.2a. Assuming sine waves for simplicity, the result is a DC component proportional to the cosine of the phase difference ($\phi_{sig} - \phi_{ref}$), and a component at $2 f_{drive}$ that can be removed by a low-pass filter:

$$\begin{aligned}
 &A \cdot \sin(2\pi f_{drive} t + \phi_{sig}) \cdot \sin(2\pi f_{drive} t + \phi_{ref}) = \\
 &0.5 \cdot A \cdot \left[\cos(\phi_{sig} - \phi_{ref}) - \cos(4\pi f_{drive} t + \phi_{sig} + \phi_{ref}) \right]
 \end{aligned}
 \tag{5.1}$$

As shown in Figure 5.2b, a phase domain delta-sigma modulator (PD $\Delta\Sigma$ M) can be realized by embedding the synchronous detector in a delta-sigma ($\Delta\Sigma$) loop [9][10]. The loop’s integrator serves as a low-pass filter and feedback is applied in

the phase domain, by toggling ϕ_{ref} between two phase references ϕ_0 and ϕ_1 depending on the bit-stream output bs . The feedback loop, on average, nulls the input of the integrator and thus ensures that the average phase reference tracks the phase of the input signal, which can therefore be derived from the average value of the bit-stream.

From (5.1) it can be seen that in order to allow the $\Delta\Sigma$ modulator to track ϕ_{sig} , the reference phase ϕ_{ref} should toggle between two values such that the term $\cos(\phi_{sig} - \phi_{ref})$ changes polarity. This implies that the two reference phases (ϕ_0 and ϕ_1) should be located on both sides of the 90° phase-shift of the input signal. The resolution with which the phase shift can be determined depends on the OSR, i.e. the number of clock cycles N that the $\Delta\Sigma$ modulator is operated per measurement, and equals $(\phi_1 - \phi_0) / N$ for a first-order $\Delta\Sigma$ modulator (given that the cosine nonlinearity can be neglected over the relatively small range $\phi_1 - \phi_0$) [10].

Simulation shows that the phase shift induced by a 1 ppm change in CO_2 concentration is roughly $7 \mu^\circ$. The required OSR to arrive at a desired CO_2 resolution can thus be estimated from this. For example, for a full scale $\phi_0 - \phi_1 = 4^\circ$, the required OSR for a quantization step equivalent to 100 ppm CO_2 is about 6000. Although this number could be reduced by using a second-order modulator, this would have little benefit, because an even higher OSR is needed to reduce the effects of the sensor's thermal noise to the 100-ppm level, as will be shown in Section 5.3.4.

5.3 Circuit Implementation

5.3.1 Front-End Dynamic Range Reduction Technique

While the voltage across the transducer contains temperature information, its sensitivity to temperature will change with the current level. To mitigate this, an additional sense current I_s , switched at a much faster rate f_{sense} , produces a modulated voltage proportional to $R(t)$ with a fixed sensitivity to temperature, independent of the drive current (Figure 5.3a).

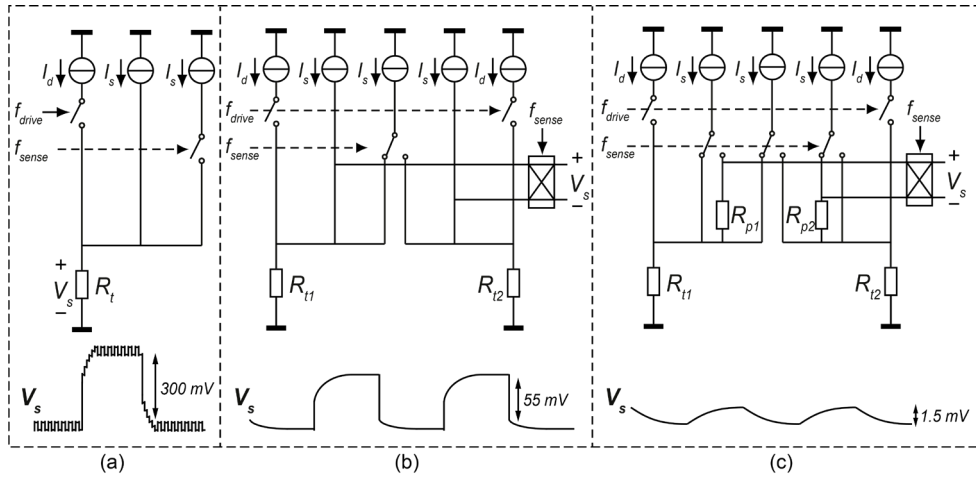


Figure 5.3. Sensing the temperature-induced resistance changes using (a) current modulation, (b) differential sensing, and (c) baseline cancellation.

To ease the detection of this voltage in the presence of the large voltage transients (about 300 mV peak-to-peak) caused by the pulsed current I_d , a pair of transducers are both driven by I_d ($=2$ mA), and read out differentially via an extra sense current I_s ($=0.5$ mA), switched at $f_{sense} = 15 \times f_{drive}$ (Figure 5.3b). Thus, the signal at f_{drive} is converted into a common-mode signal and can be rejected, while the differential signal is demodulated using a chopper switch, resulting in an output voltage V_s that contains the temperature transients at f_{drive} . Each transducer is also biased by an additional constant sense current I_s ($=0.5$ mA) to provide a voltage signal to be sensed when I_d is switched off.

An odd ratio of 15 between the f_{sense} and f_{drive} is chosen here to prevent errors due to the down-conversion of harmonics of the drive signal. This is because any mismatch between the drive signals will cause a fraction of the common-mode drive signal to be converted into a differential-mode signal. If f_{sense} is an even multiple of f_{drive} , the odd harmonics of this differential-mode signal will be down-converted to f_{drive} by the chopper demodulation at f_{sense} , and then detected by the PDAEM, affecting the decimated results. If f_{sense} is chosen to be an odd multiple of f_{drive} , any down-converted harmonics will end up at DC, and will be rejected by the PDAEM.

Even with this arrangement, a large dynamic range is still required, since the temperature-induced resistance increase ($\Delta R \approx 3\Omega$) is small compared to the

baseline resistance ($R_0 = 110 \Omega$), while the changes in ΔR due to changes in CO_2 concentration are even smaller (about $1.5 \mu\Omega$ per ppm CO_2). To cancel the voltage steps associated with R_0 , two poly resistors $R_{p1,2} (= R_0)$ are connected in series with the transducers, and the sense currents are routed such that the additional voltage drop $I_s R_p$ cancels out $I_s R_0$ (Figure 5.3c). The remaining differential signal V_s is ideally equal to $I_s \Delta R$, and reflects the transient temperature change, which is about 1.5 mV , $200\times$ smaller than the initial 300 mV transients.

5.3.2 Current Trimming DACs

In practice, however, mismatch between the transducers and the poly resistors leads to AC ripple, which reduces the modulator's effective resolution and increases the requirements on its dynamic range. To minimize the ripple, three current DACs are used to trim the drive and sense currents. As shown in Figure 5.4, one 6-bit drive-current DAC (I_{DACd} , $LSB = 0.1\% I_{REF} = 0.025\% I_d$) is used to trim the two drive current sources and thus compensate for the mismatch between the two transducers R_{t1} and R_{t2} . Two 6-bit sense-current DACs (I_{DACs1} and I_{DACs2} , $LSB = 0.4\% I_s$) can be connected to two of the three sense current sources through a 2-to-3 multiplexer, to compensate for the mismatch between the two poly resistors, and between the poly resistors and the nominal resistance of the transducers.

If there would be no mismatch, the following would hold:

$$I_{d1}R_{t1} = I_{d2}R_{t2} \quad (5.2)$$

$$(I_{s1} + I_{s2})R_{t1} = I_{s3}(R_{t2} + R_{p2}) \quad (5.3)$$

$$I_{s1}(R_{t1} + R_{p1}) = (I_{s2} + I_{s3})R_{t2} \quad (5.4)$$

Hence the target of the current trimming is to configure the trimming DACs such that these conditions are reached.

The procedure used to find the proper trimming settings is shown in Figure 5.5. First, only the two drive current sources are used to bias the transducers R_{t1} and R_{t2} . Due to mismatch, V_s can be non-zero. The drive-current DAC is then used to compensate for this mismatch such that $V_s \approx 0$ and hence (5.2) holds. Second, only the sense current sources are switched on. When the switches are configured as shown, V_s is the voltage difference between the left and right branches, which ideally should be zero as demonstrated by (5.3). Due to the variation of poly

resistor R_{p2} , this voltage can be above or below zero. Here it is assumed that $V_s > 0$ as an example to demonstrate the trimming procedure. To reduce V_s to zero, I_{DACs1} is connected as shown to add current to I_{s3} and thus null V_s , so that (5.3) holds. Thirdly, the switches for the sense current sources are changed to the other state. Again, due to mismatch, $V_s \neq 0$. Here it is again assumed that $V_s > 0$. To reduce V_s to zero, I_{DACs2} is connected as shown to add current into I_{s2} and thus V_s , so that (5.4) holds.

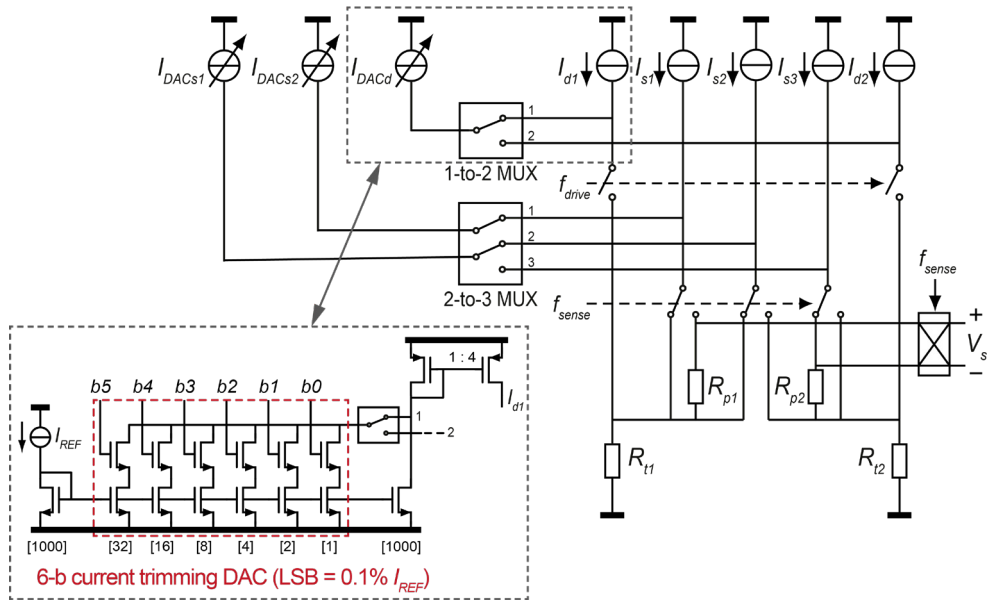


Figure 5.4. Current trimming DACs to compensate for the mismatch between the resistive transducers as well as the poly resistors (one of the total three DACs is shown as example).

In summary, current trimming is used to modify the sense currents I_{s1} , I_{s2} , and I_{s3} so as to compensate for the mismatch of the resistors and drive the steady-state voltage difference between the left and right branches to zero. The example shown here is for $V_s > 0$ in both steps 2 and 3. For other cases, the proper settings of the DACs can be found in a similar way. By analyzing all possible cases, it is found that two multiplexed DACs for the three sense currents are sufficient, though three DACs may simplify the trimming procedure. To save die area, this design uses one trimming DAC for drive current and two trimming DACs for sense current.

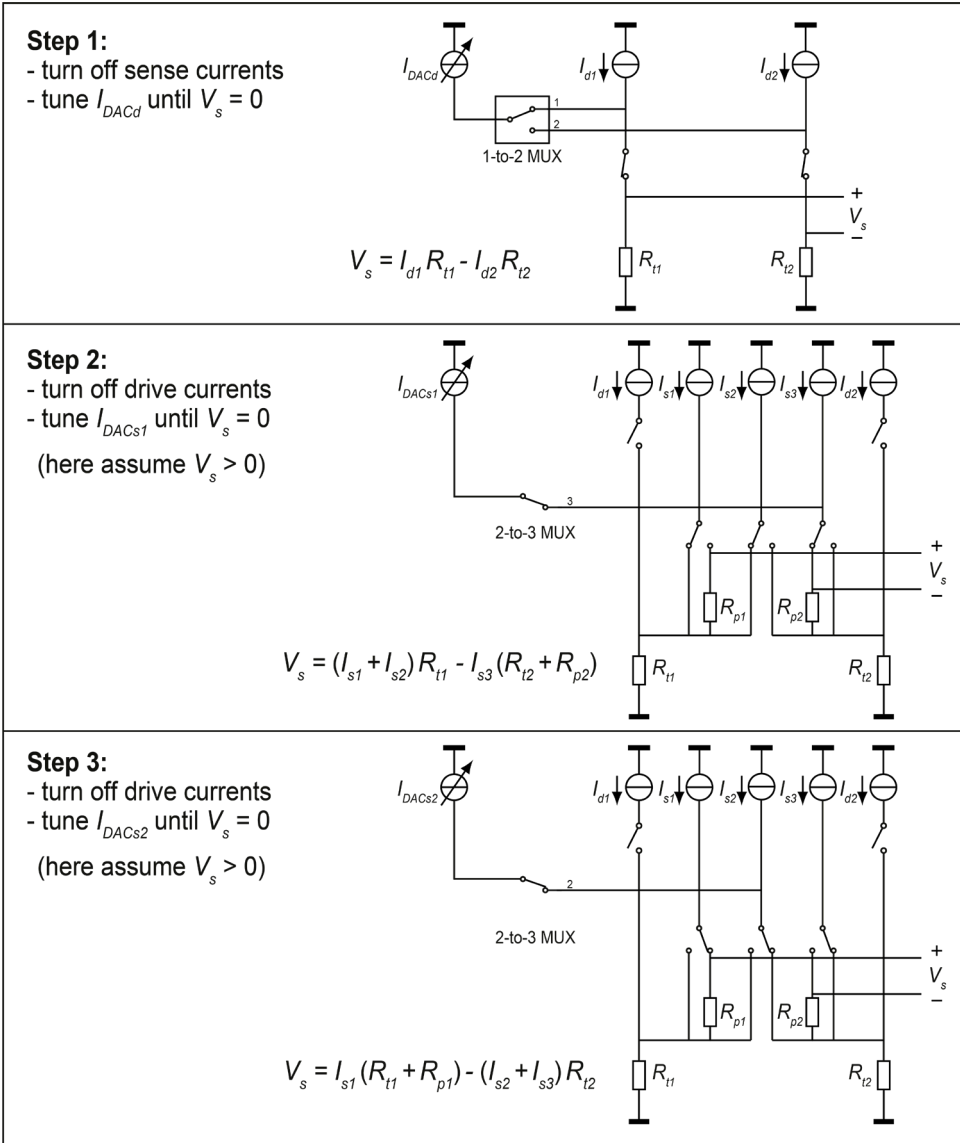


Figure 5.5. Procedure to find the proper settings for the current trimming DACs.

5.3.3 Phase-Domain Delta-Sigma Modulator

The phase shift of the temperature-related differential signal $V_s (\approx I_s \Delta R)$ is digitized by a low-noise phase-domain $\Delta\Sigma$ modulator similar to that described in [5]. As shown in Figure 5.6, before demodulation by f_{sense} , a low-noise transconductor g_m converts the differential voltage V_s into a current. This current passes through a chopper switch, which serves to dual purpose of demodulation by f_{sense} (like the chopper switch in Figure 5.3), and multiplication with the phase-shifted versions of f_{drive} as a function of the bit-stream (as in Figure 5.2b). This combination is realized by multiplying the phase-shifted versions of f_{drive} with f_{sense} by means of XOR gates. The resulting demodulated current is proportional to the phase difference between $V_s(t)$ and the selected phase reference. This difference is integrated on capacitors C_{int} of an active integrator and quantized using a clocked comparator, to form a $\Delta\Sigma$ loop which nulls the input of the integrator and thus ensures that the average phase reference tracks the phase of $V_s(t)$, which can therefore be derived from the average value of the bit-stream.

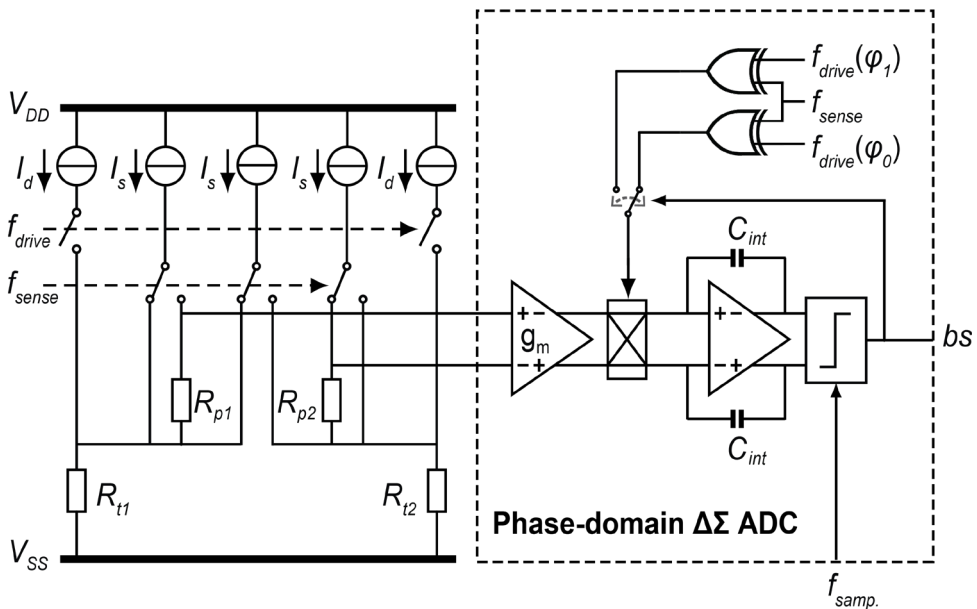


Figure 5.6. Circuit diagram of the proposed readout circuit.

To ensure that the noise from the transconductor is lower than that from the transducer and its bias circuit, the g_m of the transconductor should be at least 400 μS . The transconductance of the g_m stage is about 560 μS . The sampling frequency is chosen the same as f_{drive} . Both f_{drive} and f_{sense} , including the feedback signals at f_{drive} with reference phases ϕ_0 and ϕ_1 , are derived from a single off-chip master clock. The capacitor C_{int} in the integrator is 50 pF.

5.3.4 Noise Analysis

The noise of the phase-domain $\Delta\Sigma$ ADC can be analyzed using a charge-balancing analysis similar to that described in [11]. During a complete $\Delta\Sigma$ conversion, the total charge accumulated in the integrator is approximately zero. This includes all signal charge accumulated in the $\Delta\Sigma$ cycles when $bs = 0$ and when $bs = 1$, as well as the noise charge:

$$Q_{acc} = Q_{sig} + q_{n,acc} = N[(1 - \mu)Q_0 + \mu Q_1] + q_{n,acc} = 0 \quad (5.5)$$

in which Q_{sig} is the total signal charge and $q_{n,acc}$ is the total noise charge, N is the total number of $\Delta\Sigma$ cycles during one conversion, μ is the average value of the bitstream, Q_0 is the accumulated signal charge in one $\Delta\Sigma$ cycle when $bs = 0$, and Q_1 is the accumulated signal charge in one $\Delta\Sigma$ cycle when $bs = 1$.

Rearranging (5.5) results in the expression for μ :

$$\mu = \frac{Q_0}{Q_0 - Q_1} + \frac{q_{n,acc}}{N(Q_0 - Q_1)} \quad (5.6)$$

in which the first part is the average value of the bitstream in the noise-free case, and the second part represents the noise contribution. The total accumulated noise charge is related to the noise charge q_n accumulated in one cycle as $q_{n,acc}^2 = N q_n^2$. By substituting this in (5.6), the standard deviation of μ can be expressed as:

$$\sigma_\mu = \frac{1}{Q_0 - Q_1} \sqrt{\frac{q_n^2}{N}} \quad (5.7)$$

Referring to Figure 5.2, the signal charge difference $Q_0 - Q_1$ can be approximated as:

$$\begin{aligned} Q_0 - Q_1 &= I_{\text{int}} \cdot t_{\text{clk}} \left[\cos(\phi_{\text{sig}} - \phi_0) - \cos(\phi_{\text{sig}} - \phi_1) \right] \\ &\approx I_{\text{int}} \cdot t_{\text{clk}} (\phi_0 - \phi_1) \end{aligned} \quad (5.8)$$

in which I_{int} is the output current of the transconductor g_m , t_{clk} is the inverse of the sampling frequency, and the approximation is justified as both $(\phi_{\text{sig}} - \phi_0)$ and $(\phi_{\text{sig}} - \phi_1)$ are close to $\pi/2$.

Noise charge accumulated in every cycle includes noise from the current source, the transducers, the transconductor g_m and the chopper switches:

$$q_n^2 = q_{n,cs}^2 + q_{n,R_t}^2 + q_{n,ch}^2 + q_{n,g_m}^2 = 4kTR_n \cdot g_m^2 \cdot t_{\text{clk}}^2 \cdot B \quad (5.9)$$

in which $q_{n,cs}$ is the noise charge due to the current source, q_{n,R_t} is the noise charge due to the transducers (including the poly resistors), $q_{n,ch}$ is the noise charge generated by the chopper switches, q_{n,g_m} is the noise from the transconductor g_m , k is Boltzmann's constant, T is absolute temperature, B is the equivalent noise bandwidth ($= 1/2t_{\text{clk}}$), and R_n is the equivalent noise resistance. The latter is given by:

$$R_n = \gamma_1 g_{m,cs} R_t^2 + R_t + R_{on,ch} + \frac{\gamma_2}{g_m} \quad (5.10)$$

in which γ_1 and $g_{m,cs}$ are the excess noise factor and the transconductance of the current source, respectively, R_t is the resistance of the transducers, $R_{on,ch}$ is the on-resistance of the chopper switches, γ_2 is the excess noise factor of the transconductor g_m . Substituting (5.8) and (5.9) into (5.7) results in an expression for the standard deviation of the output-referred noise:

$$\sigma_\mu = \frac{g_m}{I_{\text{int}} (\phi_0 - \phi_1)} \sqrt{\frac{2kTR_n}{N \cdot t_{\text{clk}}}} = \frac{16}{I_s \cdot \Delta R \cdot (\phi_0 - \phi_1)} \sqrt{\frac{2kTR_n}{N \cdot t_{\text{clk}}}} \quad (5.11)$$

in which $I_{int} = (1/16) I_s \cdot \Delta R \cdot g_m$. Note that this derivation approximates the drive and sense currents, as well as the feedback signals as sinusoidal signals.

This expression shows that the standard deviation of μ and hence the resolution can be improved by decreasing the equivalent noise resistance, by increasing the total conversion time, or by increasing the signal amplitude ($I_s \Delta R$). Note that the latter also requires an increase in the size of the integration capacitors, as the sampling frequency of the PD $\Delta\Sigma$ should not be higher than the drive frequency (f_{drive}). System-level simulations show that a 50-pF integration capacitor can handle a signal amplitude of about 1.5 mV. The resistance of the transducer is 110 Ω in this work. We have chosen the drive current (2.5 mA) such that the temperature-induced resistance ΔR is limited to 3 Ω , and the sensing current I_s is 0.5 mA. The resulting calculated resolution, expressed in terms of an equivalent CO₂ concentration, is shown in Figure 5.9 as a function of the number of $\Delta\Sigma$ cycles N (i.e., the OSR).

5.4 Experimental Results and Discussion

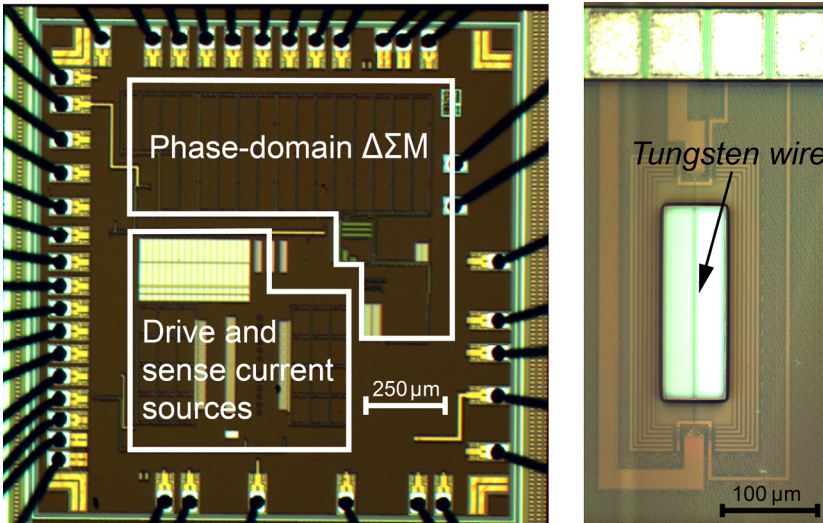


Figure 5.7. Micrograph of the readout circuit and the transducer.

TIME-DOMAIN READOUT

Both the transducers and the readout circuit have been implemented in the same $0.16\ \mu\text{m}$ CMOS technology (Figure 5.7), with an active area of $0.3\ \text{mm}^2$ and $3.14\ \text{mm}^2$, respectively. For flexibility, they have been realized on separate chips and connected on the PCB, and hence they can readily be co-integrated. Control signals for the $\Delta\Sigma$ modulator and the current DACs are generated using an FPGA. The readout circuit consumes $6.8\ \text{mW}$ from a $1.8\ \text{V}$ supply, $6.3\ \text{mW}$ of which is dissipated in the transducers.

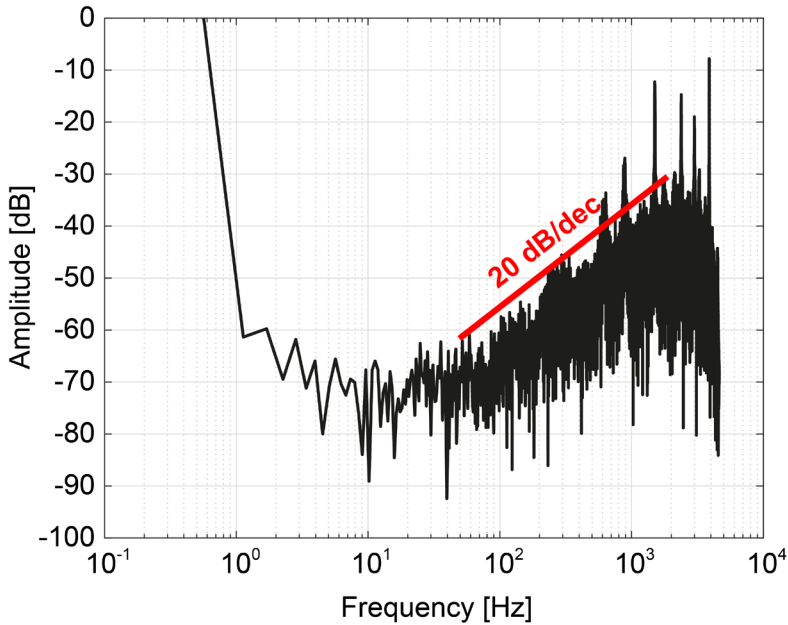


Figure 5.8. Measured spectrum of the bitstream (FFT of 2^{14} points).

Figure 5.8 shows the measured bitstream spectrum of the $\text{PD}\Delta\Sigma\text{M}$, demonstrating a first-order noise shaping similar to that of a conventional amplitude-domain 1st-order $\Delta\Sigma$ modulator.

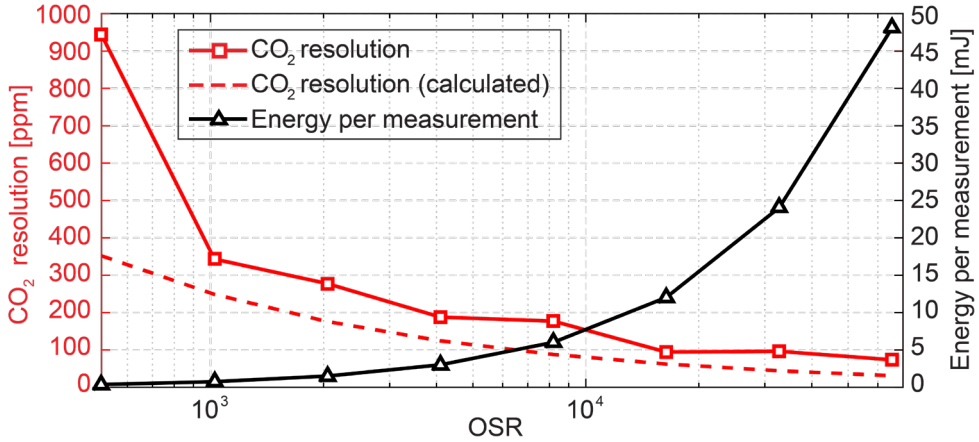


Figure 5.9. Measured resolution (standard deviation of 20 consecutive measurements) and energy per measurement as a function of OSR.

Figure 5.9 shows the measured resolution (standard deviation of 20 consecutive measurements) as well as corresponding energy per measurement at different oversampling ratios. The calculated CO₂ resolution (dashed curve) is derived from (5.11) and the measured sensitivity of decimated results to CO₂ concentration (1.6 ppm in μ per ppm CO₂). The measured resolution is in good agreement with the calculation in the thermal-noise-limited region where OSR > 1000. At lower OSR, the performance is dominated by quantization errors. A resolution equivalent to 94 ppm CO₂ is reached at an OSR of 16384, which corresponds to a measurement time of 1.8 s ($f_{\text{samp}} = f_{\text{drive}} = 9.26$ kHz), and an energy consumption of 12 mJ per measurement.

The thermal delay, or equivalently the measured phase shift, caused by the thermal resistance and thermal capacitance, should present a first-order behavior as a function of the driving frequency, like a first-order electrical low-pass filter. This is confirmed by measurements, as shown in Figure 5.10. The measured phase shift as a function of the drive frequency shows a good agreement with the ideal first-order behavior associated with the hot-wire's thermal time constant (measured using a larger full scale $\phi_0 - \phi_1 = 12^\circ$ for clarity).

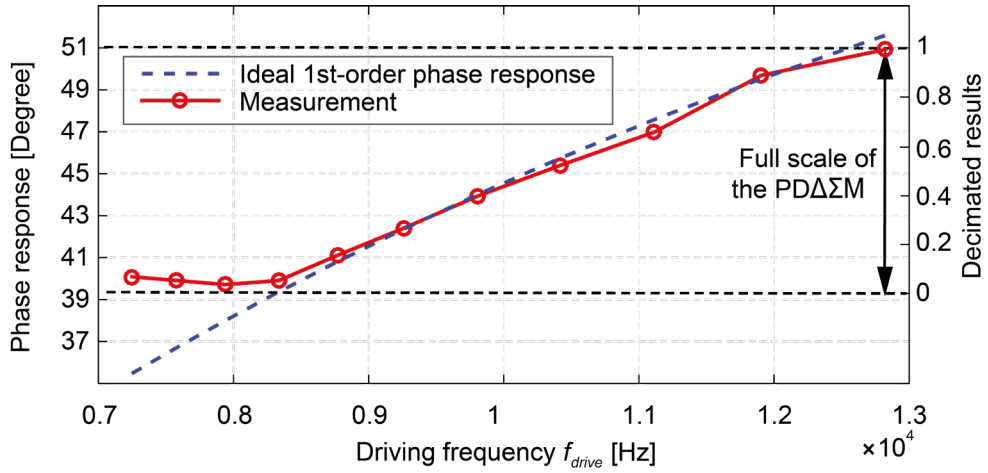


Figure 5.10. Measured phase shift as a function of the drive frequency.

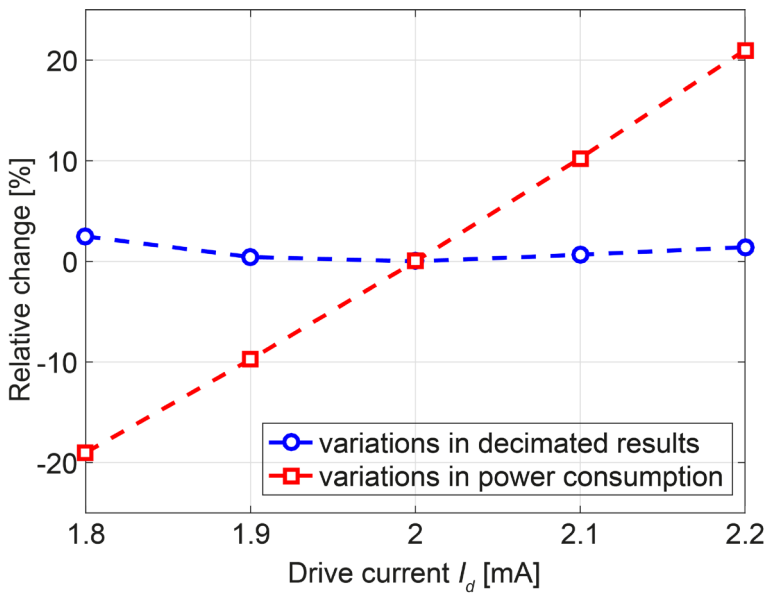


Figure 5.11. Relative changes in the decimated results as well as in power consumption as a function of drive current.

To demonstrate the sensitivity of the sensor's output to variations in power consumption, Figure 5.11 shows the decimated results and the power consumption as a function of the drive current I_d . With $\pm 10\%$ change in current, the power consumption changes by $\pm 20\%$, while the decimated results change by 2.5%, equivalent to a variation of about 1.5% in CO_2 concentration (given the sensitivity of 1.6 ppm per ppm CO_2). For 200-ppm accuracy in CO_2 measurement, this implies that variations in the power dissipation should be less than ± 2600 ppm. Compared to steady-state TC sensing, for which the required stability of the power dissipation would be < 80 ppm when measuring in amplitude domain, the time-domain readout reduces the sensitivity to power level by 30-50 \times . The residual dependency could come from two possible sources. One is the temperature-dependent sensitivity [6]. Due to the change in power dissipation, the temperature of the hot-wire changes. It has been found in the previous work that the sensitivity of the thermal conductivity of air to CO_2 concentration is not constant but temperature-dependent. This could lead to power (temperature)-dependent measurement results. A second possible source of the residual current dependence is residual mismatch after trimming. This mismatch will appear as a DC input to the $\text{PD}\Delta\Sigma\text{M}$, which causes ripple at the output of the integrator. Since the $\text{PD}\Delta\Sigma\text{M}$ has a finite ability to reject this ripple, and the amplitude of the ripple is proportional to the current level, the output of the $\text{PD}\Delta\Sigma\text{M}$ will depend on the current level.

To measure the CO_2 response, the sensor was placed in a sealed box along with an NDIR reference CO_2 sensor [12]. Like other TC-based sensors [2], the sensor is cross-sensitive to ambient variations, such as temperature, humidity, and pressure, which therefore need to be compensated for in a final product. In our experiment, ambient temperature, humidity and pressure sensors were placed in the sealed box to facilitate cross-sensitivity compensation. The results after compensation are shown in Figure 5.12, demonstrating a good agreement between the readings of our sensor and the CO_2 concentration measured by the reference CO_2 sensor K30.

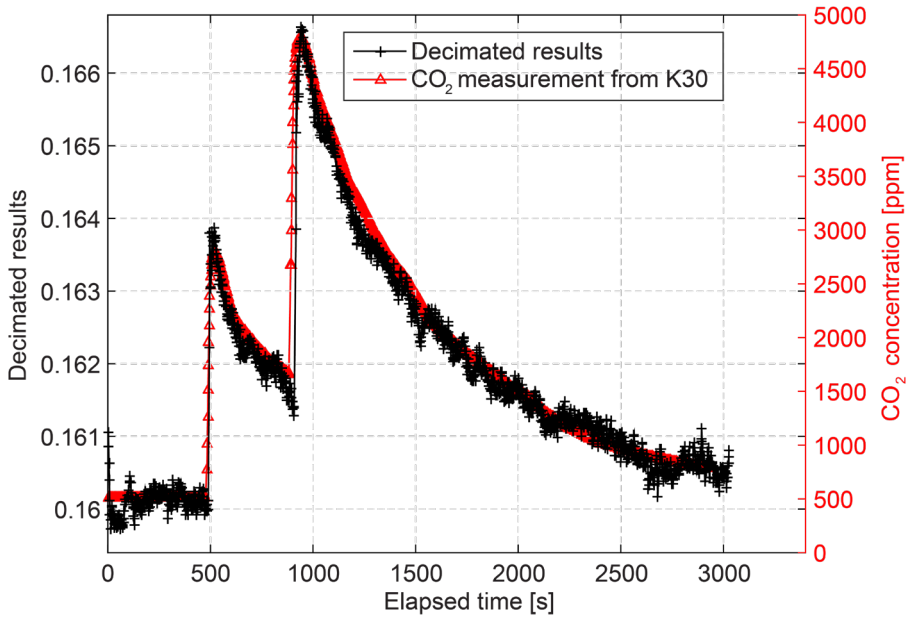


Figure 5.12. Transient CO₂ response of the CO₂ sensor and an NDIR-based reference sensor (K30).

Table 5.1 summarizes the performance of the chip and compares it with the prior art. The proposed TC-based CO₂ sensor achieves a resolution of 94 ppm while dissipating only 12 mJ per measurement, which represents a significant improvement in energy efficiency compared to the state-of-the-art for TC-based CO₂ sensors. Compared with the NDIR-based counterpart, the proposed sensor has advantages in cost (>10×) and volume (>100×) due to its CMOS-compatibility, and also consumes less energy.

Table 5.1. Performance summary and benchmarking

Parameter	This work	[6]	[2]	[12]	[13]
Method	TC	TC	TC	NDIR	NDIR
Technology	CMOS (0.16 μm)	CMOS (0.16 μm)	SOI MEMS	Module	SOI MEMS
On-chip readout	Y	Y	N	N	N
Area (sensor)	0.3 mm ²	0.6 mm ²	16 mm ²	-	†0.3 mm ²
Area (readout)	3 mm ²	3 mm ²	-	-	-
Supply voltage	1.8 V	1.8 V	-	5-14 V	-
Power consumption	6.8 mW	11.2 mW	3 mW	200 mW	200 mW
Meas. time	1.8 s	30 s	60 s	2 s	2.4 s
CO ₂ resolution	94 ppm	202 ppm	456 ppm	20 ppm	250 ppm
Energy / meas.	12 mJ	336 mJ	180 mJ	400 mJ	480 mJ

†Area of the IR emitter only, excluding 80-mm light tube and an infrared detector

5.5 Conclusions

In this chapter, we have presented a CMOS-compatible CO₂ sensor that senses the CO₂-dependent variations in the thermal conductivity (TC) of ambient air. Rather than measuring the steady-state temperature rise of a hot-wire transducer, we detect its thermal time constant τ_{th} , thus obviating the need for heating-power stabilization and accurate temperature sensing. The thermal time constant is the product of the wire's thermal capacitance and its thermal resistance to ambient, which in turn depends on the TC of the surrounding air. It is sensed by periodically heating up the wire and digitizing the phase shift in the resulting temperature transients by means of a low-noise phase-domain $\Delta\Sigma$ modulator. The temperature transients are sensed through the resistance changes of the heater resistor, greatly simplifying the fabrication process compared to prior designs that employ separate resistive or thermopile-based temperature sensors closely integrated with the heater. In order to reduce energy consumption, the required dynamic range of the readout circuit is substantially reduced by cancelling the baseline resistance and by removing the impact of the large electrical driving signals. The sensor achieves a CO₂ resolution of 94 ppm at only 12 mJ energy consumption per measurement, the best reported resolution in TC-based CO₂ sensors and the lowest energy consumption compared to the prior art. This makes this design a promising candidate for CO₂ sensing in cost- and energy-constrained applications.

References

- [1] A. MahdaviFar et al., "Transient thermal response of micro-thermal conductivity detector (μ TCD) for the identification of gas mixtures: An ultra-fast and low power method," *Microsystems & Nanoengineering*, 1(2015) 15025.
- [2] K. Kliche et al., "Sensor for thermal gas analysis based on micromachined silicon-microwires," *IEEE Sensors J.*, vol. 13, no. 7, pp. 2626–2635, Jul. 2013.
- [3] K. Kliche et al., "Sensor for gas analysis based on thermal conductivity, specific heat capacity and thermal diffusivity," in *Proc. IEEE Int. Conf. on MEMS*, 2011, pp. 1189-1192.
- [4] C. van Vroonhoven, G. de Graaf and K. A. A. Makinwa, "Phase readout of thermal conductivity-based gas sensors," in *Proc. IEEE Int. Workshop on Advances in Sensors and Interfaces (IWASI)*, 2011, pp. 199-202.

- [5] S. M. Kashmiri, K. Souiri and K. A. A. Makinwa, "A scaled thermal-diffusivity-based 16 MHz frequency reference in 0.16 μm CMOS," *IEEE J. Solid-State Circuits*, vol. 47, no. 7, pp. 1535-1545, Jul. 2012.
- [6] Z. Cai et al., "A ratiometric readout circuit for thermal-conductivity-based resistive CO₂ sensors," *IEEE J. Solid-State Circuits*, vol. 51, no. 10, pp. 2463-2474, Oct. 2016.
- [7] Z. Cai et al., "A phase-domain readout circuit for a CMOS-compatible thermal-conductivity-based carbon dioxide sensor," in *Dig. Techn. Papers ISSCC Feb. 2018*, pp. 332-334.
- [8] Z. Cai et al., "An integrated carbon dioxide sensor based on ratiometric thermal-conductivity measurement," in *Proc. IEEE Int. Conf. on Solid-State Sensors, Actuators and Microsystems (Transducers '15)*, 2015, pp. 622-625.
- [9] C.P.L. van Vroonhoven and K.A.A. Makinwa, "A thermal-diffusivity-based temperature sensor with an untrimmed inaccuracy of $\pm 0.5^\circ\text{C}$ (3σ) from -40 to 105°C ," *Digest ISSCC*, pp. 576 – 577, Feb. 2008.
- [10] M. Kashmiri, S. Xia and K.A.A. Makinwa, "A temperature-to-digital converter based on an optimized electrothermal filter," *IEEE J. Solid-State Circuits*, vol. 44, no. 7, pp. 2026 – 2035, Jul. 2009.
- [11] M. A. P. Pertijs and J. Huijsing, *Precision Temperature Sensors in CMOS Technology*. Dordrecht, The Netherlands: Springer-Verlag, 2006.
- [12] SenseAir K30 datasheet, SenseAir [Online]. Available: <http://www.senseair.com/>.
- [13] T.A. Vincent and J.W. Gardner, "A low cost MEMS based NDIR system for the monitoring of carbon dioxide in breath analysis at ppm levels," *Sens. and Actuators B, Chem.*, vol. 236, pp. 954-964, Nov. 2016.

Chapter 6

CONCLUSIONS

This last chapter summarizes the original contributions and main findings in this thesis. It also provides recommendations for the future research on smart carbon dioxide sensors in CMOS technology.

6.1 Main Contributions

- **First fully-integrated CO₂ sensor in standard CMOS technology for indoor air-quality (IAQ) sensing (Chapter 3)**

This design demonstrated that hot-wire transducers realized in the Tungsten VIA layer of a standard CMOS process can be used as the basis of a fully-integrated CO₂ sensor. The proposed sensor employs two such transducers: a sensing transducer and a reference (non-sensing) transducer. By making ratiometric measurements of the temperature and power dissipation of both transducers, the readout electronics obviates the need for an accurate power reference. The proposed sensor achieved a resolution of about 200 ppm, and compared with conventional optical-based solutions, offers significant advantages in terms of cost and volume.

- **Algorithmic bandgap voltage reference and temperature sensor constructed in digital domain (Chapter 4)**

This design demonstrated that an algorithmic BJT-based voltage reference and temperature sensor can be realized with a minimum of analog signal processing. It consists of a single BJT that can be biased at a number of well-defined current levels, and a high-resolution ADC that digitizes the resulting base-emitter voltages. The results are then combined in the digital domain, thus facilitating the correction of several sources of deterministic error: leakage current, series resistance, ADC offset and non-linearity. The

CONCLUSIONS

effectiveness of the design was verified by incorporating it in an algorithmic readout system that measures the power dissipation of a resistive transducer, which requires a reference voltage and a temperature-compensated reference resistor. The proposed system achieved an inaccuracy of $\pm 0.8\%$ in the measured power over the automotive temperature range (-40°C to 125°C). Compared with prior power-sensing circuits, this algorithmic approach offers accurate measurement over both load and temperature variations.

- **First sub 100-ppm resolution CO₂ sensor in standard CMOS technology with record energy efficiency (Chapter 5)**

This design demonstrated that an integrated CO₂ sensor with <100 ppm resolution can be realized in a standard CMOS process. The readout electronics employed a phase-domain $\Delta\Sigma$ modulator to measure the thermal time constant of the Tungsten hot-wire transducer. Sensor fabrication was simplified by using a single transducer both as a heater and as a temperature sensor. In addition, a novel differentially-driven bridge enabled the extraction of the temperature information in the presence of large heating currents. The realized sensor achieved a resolution of 94 ppm while dissipating only 12 mJ per measurement, which represents the best reported performance for a CMOS CO₂ sensor in terms of both resolution and energy consumption.

6.2 Main Findings

System-level:

- TC sensing using a hot-wire transducer requires precise control or measurement of the power dissipated in the transducer. This is particularly important when designing high-precision (e.g. 100-ppm level) TC-based CO₂ sensors, which require the accurate detection of very small (sub-microwatt-level) changes in heat dissipation (Chapter 3).
- CO₂ sensors based on ratiometric measurements of a sensing and reference transducer have a relatively relaxed requirement on the stability of their power dissipation. This is because such measurements translate a

requirement for absolute accuracy into a requirement on the matching of the sensor and reference transducers (Chapter 3).

- Digitizing analog signals at an early stage in the signal chain and moving signal processing fully to the digital domain is a promising direction for sensor design, as digital signal processing has superior flexibility and accuracy compared to analog signal processing (Chapter 4).
- For TC sensors, time-domain readout based on a continuous-time phase-domain $\Delta\Sigma$ modulator (PD $\Delta\Sigma$ M) results in improved resolution and energy efficiency compared to amplitude-domain readout based on a conventional discrete-time $\Delta\Sigma$ modulator (Chapter 5).
- Compensation for the cross-sensitivities of hot-wire transducers to ambient temperature, humidity and pressure, as well as measures to limit their sensitivity to airflow, is crucial for the practical implementation of TC-based CO₂ sensors. By using state-of-the-art integrated temperature and humidity sensors, however, the resulting CO₂-sensing errors can be limited to 200 ppm (Chapter 2).

Circuit-level:

- For hot-wire transducers, the choice of bias current level should depend not only on the required SNR requirements, but also on the required sensitivity to TC changes and on the required reliability. From the point of view of maximizing SNR, increasing bias current may seem good. However, the relationship between power and SNR is more complicated for TC-based gas sensors, and only a modest improvement in resolution may be obtained if the bias current is increased beyond a certain level. In addition, when biased by a constant current source, the maximum bias current may be limited due to the positive feedback loop created by the transducer's positive temperature-coefficient. To mitigate this, the bias current (I) should be chosen such that the loop gain ($\sim I^2$) is far from unity (Chapter 3).
- Baseline resistance compensation is critical in realizing energy-efficient and high-precision resistive CO₂ sensors. It effectively relaxes the dynamic range (DR) requirement of the readout circuit, thus reducing its power consumption. This is particularly effective for TC-based CO₂ sensors, as

CONCLUSIONS

the temperature-induced resistance change (ΔR) of a hot-wire transducer is small compared to the baseline resistance, while the change in ΔR due to changes in CO₂ concentration ($\Delta\Delta R$) is even smaller (Chapters 3 & 5).

- The algorithmic readout approach requires an ADC with high resolution as well as high speed. This is because several measurements, of the targeted measurands (e.g. resistance, current or power) and various base-emitter voltages, are required to generate the final result. In principle, the accuracy of this result is only limited by ADC resolution, as long as the ADC's reference voltage remains stable over one complete set of measurements. The ADC must then make these measurements fast enough to ensure that the effect of temperature drift on this voltage and on the other measurands is negligible (Chapter 4).
- If a phase-domain readout scheme is employed, the optimal frequency at which a TC transducer should be driven is approximately equal to its thermal cut-off frequency, as this gives the maximum sensitivity of the detected phase shift to the thermal time constant (τ_{th}). In addition, the sampling rate of the phase-domain ADC is limited by the driving frequency of the transducer. Sampling at a faster rate does not improve resolution, because the reference signals are simply phase-shifted versions of the driving signal, and thus have the same frequency (Chapter 5).

6.3 Future Work

- **Further optimization and improvement on the hot-wire transducers**

The tungsten hot-wire sensor realized in the VIA layer can be further optimized for sensitivity and reliability. To improve its sensitivity, thermal losses to the substrate need to be reduced. In addition, the measured temperature coefficient of the hot-wire (0.17%/°C) is lower than that for pure tungsten (0.45%/°C) [1], which requires further investigation. In practice, we have seen that the transducer hot-wire may break after long-term heating at relatively high currents (i.e. a couple of milliamperes). This might be due to electro-migration or to an uneven heat distribution in the transducer. The robustness of the hot-wire sensor can undoubtedly be

further improved, since commercial products with similar resistive heaters already exist [2].

- **Further optimization of the noise performance for the ratiometric amplitude-domain readout approach**

The design of the ratiometric readout approach is presently limited by the thermal noise of the readout circuit. From a system-level point of view, reducing this noise will improve the energy efficiency of the system. This can be done by increasing the size of the sampling capacitors to reduce the kT/C noise, and/or by clocking the $\Delta\Sigma$ modulator at a faster rate.

- **Incorporation of an on-chip ADC for the algorithmic readout circuit**

The algorithmic sensor prototype uses an off-chip ADC for an initial proof-of-concept, which worked, but came at the expense of cost and power consumption. A suitable ADC implemented in standard CMOS technology has been reported [3], which can be co-integrated with the algorithmic sensor to realize a fully-integrated low-cost solution.

- **Further investigation into the low-frequency noise performance for the time-domain readout approach**

A close look at the transient CO₂ response shown in Chapter 5 indicates that the resolution of the TC-based sensor is not purely white. This indicates that there may be a flicker noise mechanism present in the circuit or in the experimental system. There seems to be a low-frequency noise component (i.e. with the period of a couple of minutes) masked by the transient measurement results. Investigations have been made extensively to understand this behavior, but satisfactory answers have not been found yet. One finding is that this low-frequency noise seems to be sensitive to the position of the chopper demodulator: it becomes much more manifest if the chopper demodulator is placed in front of the transconductor instead of the current place at the output of the transconductor. Further improvement on this could result in better CO₂-sensing resolution.

- **Further investigation of the cross-sensitivity compensation scheme**

Although the measurement results obtained from the sensor prototypes have been compensated for cross-sensitivities to ambient variations, it would be interesting to see the repeatability and reproducibility of the compensation on multiple chips and from there a repeatable compensation scheme can be further investigated. This would be a very important step towards final products.

- **Incorporation of in-package or on-chip temperature, humidity, pressure sensors to compensate for cross-sensitivities to ambient variations**

As explained in Chapters 1 and 2, cross-sensitivity compensation is very critical to achieve accurate CO₂ measurement. Instead of the discrete temperature, humidity and pressure sensors used in the experiments presented in this thesis, it would be very interesting to integrate CMOS-compatible environmental sensors into the same package as the CO₂ sensor as a multi-die solution, or even on the same die [8][9]. This will greatly improve the level of integration of the complete sensor system, resulting in a self-contained, independent CO₂ sensor module. With the integrated environmental sensors, a systematic and reliable cross-sensitivity compensation scheme can be developed.

- **Further investigation of packaging solutions to flow dependency**

Flow dependency can be compensated for by co-integrating a flow sensor, but a simpler approach would involve improved packaging, the effect and cost of which can be further investigated.

- **Development of a compact smart CO₂ sensing SOC**

After incorporating the sensors for ambient variation compensation, the final step would be to develop a compact smart CO₂ sensor in a small package. For flexibility and ease-of-use, the current prototypes are packaged in a ceramic dual-in-line (DIL) package, which is larger than strictly necessary. Implementing the sensor chip in a compact package (e.g., a flat package or a small outline package) will allow the sensor to be integrated in mobile devices, which could open up many new applications for CO₂ sensing.

References

- [1] Douglas C. Giancoli, *Physics: Principles with Applications* (4th Edition). Prentice Hall, 1995.
- [2] FIGARO TGS8100 Datasheet, FIGARO [Online]. Available: <http://www.figaro.co.jp/>
- [3] Y. Chae, K. Souri, and K. A. A. Makinwa, "A 6.3 μ W 20 bit incremental zoom-ADC with 6 ppm INL and 1 μ V offset," *IEEE J. Solid-State Circuits*, vol. 48, no. 12, pp. 3019–3027, Dec. 2013.
- [4] B. Yousefzadeh, S. Heidary Shalmany and K. A. A. Makinwa, "A BJT-based temperature-to-digital converter with ± 60 mK (3σ) inaccuracy from -55 $^{\circ}$ C to $+125$ $^{\circ}$ C in 0.16- μ m CMOS," *IEEE J. Solid-State Circuits*, vol. 52, no. 4, pp. 1044-1052, Apr. 2017.
- [5] Z. Tan, R. Daamen, A. Humbert, Y. V. Ponomarev, Y. Chae, and M. A. P. Pertijs, "A 1.2-V 8.3-nJ CMOS humidity sensor for RFID applications," *IEEE J. Solid-State Circuits*, vol. 48, no. 10, pp. 2469–2477, Oct. 2013.

CONCLUSIONS

SUMMARY

This thesis describes the design and realization of CMOS-compatible CO₂ sensors based on thermal conductivity (TC) measurement for indoor air-quality sensing. The goal of this work is to investigate the advantages and limitations of sensing CO₂ based on TC measurement, and to exploit its potential to achieve the best possible performance in terms of both CO₂ resolution and energy efficiency. Both system-level and circuit-level techniques have been explored, resulting in three prototypes that demonstrate the effectiveness of the proposed techniques. The final prototype, using a time-domain readout approach, achieves a CO₂ resolution better than 100 ppm while consuming only 12 mJ per measurement, representing the best-reported performance for a CMOS CO₂ sensor in terms of both resolution and energy consumption.

Chapter 1 – Introduction

Chapter 1 presents an introduction to this thesis and describes the research problem of this work: the lack of cost-effective and energy-efficient CO₂ sensors for air-quality monitoring in home and building automation. To better understand the significance of the problem, the role of CO₂ sensors in Smart Buildings is described, and the limitations of the existing methods are discussed. Next, a review of the three most commonly used ways to measure CO₂ concentration in air is presented. This analysis reveals that sensing CO₂ based on TC measurement has unique advantages for the system integration in CMOS technology, which means a significant reduction in cost and size. In view of electrical and mechanical properties, a hot-wire transducer realized in the VIA layer of a standard CMOS process is proposed as CO₂ transducer. To identify possible areas for improvement, the limitations of prior TC-based sensors are discussed, and as a result, three readout approaches are proposed to address these limitations: (1) readout based on ratiometric measurements in the amplitude domain; (2) readout based on algorithmic resistance and power measurement in the amplitude domain; (3) readout in the time domain.

Chapter 2 – System-Level Analysis of Thermal-Conductivity-Based Sensing

Chapter 2 presents a system-level analysis of TC-based CO₂ sensing. This serves as the basis for the design and implementation of the readout circuits discussed in the following chapters. TC sensors measure the heat loss of a suspended heated transducer through the transducer's temperature rise relative to ambient temperature. This heat loss depends on the TC of the surrounding gas, which in turn is a function of the CO₂ concentration. To achieve accurate TC measurements, the power dissipated in the transducer and its temperature rise must be accurately known, which becomes the main challenge in realizing a CO₂ sensor in CMOS technology.

A fundamental limitation of sensors based on TC measurement is the lack of selectivity among different gases. As it only measures the overall TC of the gas mixture, a TC sensor will give incorrect results if the concentration of a different gas component than the targeted component changes. This non-selectivity nature has to be taken into account when determining the use cases of sensors based on this method. For the measurement of the CO₂ concentration in indoor air, however, this is not a limiting issue since the composition of indoor air is relatively well-defined, and the main variations are changes in CO₂ concentration due to exhalation.

Another limitation of TC measurement is the cross-sensitivity to ambient variations, such as ambient temperature, humidity, pressure, and flow. To design an accurate CO₂ sensor, these variables must be carefully dealt with. The solution to this problem is to integrate environmental sensors with the CO₂ sensor. The requirements of these sensors for the targeted CO₂ accuracy are also provided.

To be able to simulate the interaction between the electrical and thermal domains, an equivalent circuit model for a TC-based CO₂ sensor is proposed. With parametrized input variables, a system-level analysis can be performed and the specifications of the readout circuits can be derived.

To meet the stringent requirements on the readout of the sensor, the system-level architectures of three different readout approaches are presented. The first approach uses ratiometric measurements to alleviate the critical requirement of the stability of the power dissipation in the transducer. The second approach uses a self-contained, indirect power reference constructed algorithmically in digital domain for the accurate power measurement required for high-precision TC

sensing. The third approach changes from the amplitude domain to the time domain, and uses a novel bridge-type sensor frontend and a high-resolution phase-domain delta-sigma analog-to-digital converter (PD Δ Σ ADC) to measure the CO₂-dependent thermal delay. A custom signal modulation scheme is used to extract the tiny signals corresponding to the temperature-induced changes in sensor resistance in the presence of large pulses due to electrical driving signals.

Chapter 3 – Ratiometric Amplitude-Domain Readout

Chapter 3 discusses the readout approach of ratiometrically measuring the temperature and power dissipation (and thus the thermal conductivity) of a CO₂-sensitive transducer relative to an isolated transducer that acts as a thermal-conductivity reference. This reference transducer has similar thermal properties to the sensitive transducer, but it is shielded from the ambient air by packaging solutions. The readout circuit digitizes the sensor's temperature and power dissipation ratiometrically relative to those of the reference. Hence external voltage, power or temperature references are not needed. To measure the temperature rise, the transducers are biased at two different current levels. To avoid long settling time in sequential measurements due to the thermal time constant, a pair of transducers (both for the sensor and for the reference) are used to generate these two states simultaneously. The dynamic element matching (DEM) technique is used for the current sources to provide an accurate current ratio for the transducers. The readout circuit employs an incremental delta-sigma ADC that can be configured to measure both the temperature and power dissipation of the CO₂ sensor. The prototype sensor, realized in a 0.16 μ m standard CMOS process, achieves a CO₂ resolution of 200 ppm and represents the first fully-integrated CO₂ sensor in standard CMOS technology, offering great advantages in cost and volume.

Chapter 4 – Algorithmic Amplitude-Domain Readout

Chapter 4 discusses the readout approach of algorithmic resistance and power measurement. High-precision CO₂ sensors based on TC measurement require a very stable power reference to define the power dissipated in the transducer, or a readout circuit that is capable of accurately measuring this power dissipation,

SUMMARY

without relying on external references. To accurately measure power, an accurate power reference is still needed. This is constructed using a bandgap voltage reference and a polysilicon reference resistor of which the temperature dependence is compensated by a temperature sensor. To do so, the algorithmic readout approach measures the voltage and current of the resistive transducer and of the reference resistor, and the base-emitter voltages of a single BJT (V_{be}) biased at different current levels, and then processes the results in the digital domain. The algorithmically-constructed bandgap reference and temperature sensor facilitate the correction of deterministic errors, such as leakage current, series resistance, and offset and non-linearity of the ADC. The effectiveness of this algorithmic readout approach has been verified by measuring the resistance and power dissipation of a Platinum resistor (Pt100). A resistance measurement inaccuracy of $\pm 0.55 \Omega$ and a power inaccuracy of $\pm 0.8\%$ have been achieved over the automotive temperature range (from -40°C to 125°C).

Chapter 5 – Time-Domain Readout

Chapter 5 discusses the approach of sensing CO_2 by means of a time-domain TC measurement. Instead of measuring the CO_2 -dependent TC in the amplitude-domain, this approach uses a high-resolution phase-domain $\Delta\Sigma$ modulator to measure the CO_2 -dependent thermal time constant (τ_{th}) of a hot-wire transducer. The time constant can be approximated by the product of the transducer's thermal capacitance (C_{th}) and its thermal resistance to ambient (R_{th}). Due to this finite thermal time constant, driving the hot-wire transducer with periodic heat pulses will result in phase-shifted temperature variations $\Delta T(t)$, which are digitized by the $\text{PD}\Delta\Sigma\text{M}$, and from which τ_{th} can be derived. To maximize the sensitivity of the detected phase shift to τ_{th} , the wire is driven at $f_{drive} = 1/2\pi\tau_{th}$, i.e. at the pole of the thermal filter. Compared to the amplitude-domain approaches presented earlier, this approach has the important advantage that the absolute temperature and power levels of the transducer do not need to be accurately stabilized or measured. The transducer is used as both a heater and a temperature sensor, which simplifies the fabrication of the sensor system. In addition, a novel differentially-driven bridge allows the extraction of the relatively small temperature information in the presence of large driving signals. The realized sensor achieves a CO_2 resolution of 94 ppm while dissipating only 12 mJ per measurement, which represents the best-reported CO_2 resolution and energy consumption for a CMOS CO_2 sensor.

Chapter 6 – Conclusions

Chapter 6 summarizes the achieved results and the original contributions in this thesis. The main findings at both system-level and circuit-level are discussed. Finally, some recommendations on future work are presented, such as further optimization of the hot-wire transducers, further optimization of the noise performance of the ratiometric amplitude-domain readout approach, incorporation of an on-chip ADC for the algorithmic readout approach, and further investigation of cross-sensitivity compensation and packaging solutions.

SUMMARY

SAMENVATTING

Dit proefschrift beschrijft het ontwerp en de realisatie van CMOS-compatibele CO₂-sensoren op basis van de meting van thermische geleidbaarheid (thermal conductivity - TC) voor het meten van de luchtkwaliteit binnenshuis. Het doel van dit werk is om de voordelen en beperkingen van CO₂-detectie op basis van TC-meting te onderzoeken en het potentieel ervan te benutten om de best mogelijke prestaties te behalen op het gebied van zowel CO₂-resolutie als energie-efficiëntie. Zowel technieken op systeemniveau als op circuitniveau zijn onderzocht, resulterend in drie prototypes die de effectiviteit van de voorgestelde technieken aantonen. Het laatste prototype bereikt met behulp van een tijdsdomeinuitlesing een CO₂-resolutie beter dan 100 ppm en verbruikt slechts 12 mJ per meting, wat de best gerapporteerde prestaties voor een CMOS CO₂-sensor vertegenwoordigt, zowel qua resolutie als energieverbruik.

Hoofdstuk 1 - Inleiding

Hoofdstuk 1 vormt de inleiding tot dit proefschrift en beschrijft het onderzoeksprobleem van dit werk: het ontbreken van kosteneffectieve en energiezuinige CO₂-sensoren voor luchtkwaliteitsbewaking in huis- en gebouwautomatisering. Om het belang van het probleem beter te begrijpen, wordt de rol van CO₂-sensoren in slimme gebouwen beschreven en worden de beperkingen van de bestaande methodes besproken. Vervolgens wordt een overzicht gepresenteerd van de drie meest gebruikte manieren om de CO₂-concentratie in lucht te meten. Deze analyse laat zien dat CO₂-detectie op basis van TC-meting unieke voordelen biedt voor de systeemintegratie in CMOS-technologie, wat een aanzienlijke vermindering van de kosten en de afmetingen betekent. Met het oog op elektrische en mechanische eigenschappen wordt een hot-wire transducent in de VIA-laag van een standaard CMOS-proces voorgesteld als CO₂-transducent. Om mogelijke verbeterpunten te identificeren, worden de beperkingen van eerdere TC-gebaseerde sensoren besproken en als resultaat worden drie uitleesmethodes voorgesteld om deze beperkingen aan te pakken: (1) uitlezing op basis van ratiometrische metingen in het amplitudedomein; (2) uitlezing op basis

van algoritmische weerstands- en vermogensmeting in het amplitudedomein; (3) uitlezing in het tijdsdomein.

Hoofdstuk 2 – Systemniveau analyse van meting op basis van thermische geleidbaarheid

Hoofdstuk 2 presenteert een systeemniveau analyse van CO₂ meting op basis van TC. Dit dient als basis voor het ontwerp en de implementatie van de uitleescircuits die in de volgende hoofdstukken worden besproken. TC sensoren meten het warmteverlies van een vrijhangende transducent middels de temperatuursteging van deze transducent ten opzichte van zijn omgeving. Dit warmteverlies hangt af van de TC van het omringende gas, wat een functie is van de CO₂ concentratie. Voor nauwkeurige TC-metingen moeten de vermogensdissipatie en de temperatuurstijging van de transducent nauwkeurig worden vastgesteld, wat de belangrijkste uitdaging wordt bij het realiseren van een CO₂-sensor in CMOS-technologie.

Een fundamentele beperking van sensoren op basis van TC-meting is het gebrek aan selectiviteit tussen verschillende gassen. Als de concentratie van een andere gascomponent dan het beoogde gas verandert, zal de TC-sensor onjuiste resultaten geven, omdat hij alleen de totale TC van het gasmengsel meet. Met deze niet-selectiviteit moet rekening worden gehouden bij het bepalen van de toepassing van sensoren op basis van deze methode. Voor de meting van de CO₂-concentratie in binnenlucht is dit echter geen beperkend probleem, omdat de samenstelling van binnenlucht relatief goed is gedefinieerd en de belangrijkste variaties in de CO₂-concentratie het gevolg zijn van uitademing.

Een andere beperking van TC-meting is de gevoeligheid voor omgevingsvariaties, zoals omgevingstemperatuur, vochtigheid, druk en luchtstroming. Om een nauwkeurige CO₂-sensor te ontwerpen, moeten deze variabelen zorgvuldig worden behandeld. De oplossing voor dit probleem is het integreren van omgevingssensoren met de CO₂-sensor. De vereisten van deze sensoren voor de beoogde CO₂-nauwkeurigheid worden ook gegeven.

Om de interactie tussen het elektrische en het thermische domein te kunnen simuleren, wordt een equivalent circuitmodel voor een TC-gebaseerde CO₂-sensor voorgesteld. Met geparametriseerde ingangsvariabelen kan een systeemniveau

analyse worden uitgevoerd en de specificaties van de uitleescircuits worden afgeleid.

Om aan de strenge eisen voor de uitlezing van de sensor te voldoen, worden de systeemniveau-architecturen van drie verschillende uitleesmethodes gepresenteerd. De eerste methode maakt gebruik van ratiometrische metingen om de kritische eis van de stabiliteit van de vermogensdissipatie in de transducent te verlichten. De tweede methode maakt gebruik van een onafhankelijke, indirecte vermogensreferentie, die algoritmisch in het digitale domein wordt geconstrueerd voor de nauwkeurige vermogensmeting die vereist is voor nauwkeurige TC-detectie. De derde methode schakelt over van het amplitude domein naar het tijd domein, en maakt gebruik van een nieuw brug-type sensor frontend en een hoge resolutie fase-domein delta-sigma analoog-naar-digitaal converter (PD Δ Σ ADC) om de CO₂-afhankelijke thermische vertraging te meten. Een speciaal ontworpen signaalmodulatietechniek wordt gebruikt om de kleine signalen te extraheren die horen bij door temperatuur veroorzaakte veranderingen in de weerstand van de sensor, in aanwezigheid van de benodigde grote elektrische aanstuurpuls.

Hoofdstuk 3 – Ratiometrische uitlezing in het amplitude domein

Hoofdstuk 3 bespreekt de uitleesmethode van het ratiometrisch meten van de temperatuur en de vermogensdissipatie (en daarmee de thermische geleidbaarheid) van een CO₂-gevoelige transducent relatief ten opzichte van een geïsoleerde transducent die fungeert als een warmtegeleidingsreferentie. Deze referentietransducent heeft vergelijkbare thermische eigenschappen als de gevoelige transducent, maar wordt in de behuizing afgeschermd van de omgevingslucht. Het uitleescircuit digitaliseert de temperatuur en vermogensdissipatie van de sensor ratiometrisch ten opzichte van die van de referentie. Daarom zijn externe referenties voor spanning, vermogen of temperatuur niet nodig. Om de temperatuurstijging te meten, worden de transducenten ingesteld op verschillende stroomniveaus. Om lange insteltijd in openvolgende metingen als gevolg van de thermische tijdconstante te voorkomen, wordt een tweetal transducenten (zowel voor de sensor als voor de referentie) gebruikt om deze twee toestanden tegelijkertijd te genereren. De Dynamic Element Matching (DEM) techniek wordt gebruikt voor de stroombronnen om een nauwkeurige stroomverhouding voor de transducenten te genereren. Het uitleescircuit maakt gebruik van een incrementele delta-sigma ADC die kan

worden geconfigureerd om zowel de temperatuur als de vermogensdissipatie van de CO₂-sensor te meten. Het prototype, gerealiseerd in een standaard 0,16 μm CMOS-proces, bereikt een CO₂-resolutie van 200 ppm en is de eerste volledig geïntegreerde CO₂-sensor in standaard CMOS-technologie, hetgeen grote voordelen biedt in kosten en volume.

Hoofdstuk 4 – Algoritmische uitlezing in het amplitude domein

Hoofdstuk 4 bespreekt de uitleesmethode van algoritmische weerstands- en vermogensmeting. Nauwkeurige CO₂-sensoren op basis van TC meting vereisen een zeer stabiele vermogensreferentie om het vermogen dat in de transducent wordt gedissipeerd vast te leggen, of een uitleescircuit dat in staat is om deze vermogensdissipatie nauwkeurig te meten, zonder te vertrouwen op externe referenties. Om het vermogen nauwkeurig te meten, is nog steeds een nauwkeurige vermogensreferentie nodig. Deze wordt geconstrueerd met behulp van een bandgap spanningsreferentie en een polysilicium referentieweerstand waarvan de temperatuurafhankelijkheid wordt gecompenseerd door een temperatuursensor. Daartoe meet de algoritmische uitleesmethode de spanning en stroom van de resistieve transducent en van de referentieweerstand, en de basis-emitterspanningen van een enkele BJT (V_{be}) ingesteld op verschillende stroomniveaus, en verwerkt vervolgens de resultaten in het digitale domein. De algoritmisch geconstrueerde bandgap referentie en temperatuursensor vergemakkelijken de correctie van deterministische fouten, zoals lekstroom, serieweerstand en offset en niet-lineariteit van de ADC. De effectiviteit van deze algoritmische uitleesmethode is geverifieerd door het meten van de weerstand en vermogensdissipatie van een platina-weerstand (Pt100). Een onnauwkeurigheid van de weerstandsmeting van $\pm 0,55 \Omega$ en een onnauwkeurigheid van het vermogen van $\pm 0,8\%$ zijn bereikt over het automotieve temperatuurbereik (van -40°C tot 125°C).

Hoofdstuk 5 – Uitlezing in het tijdsdomein

Hoofdstuk 5 bespreekt de CO₂-detectie methode op basis van TC meting in het tijdsdomein. In plaats van de CO₂-afhankelijke TC in het amplitudedomein te meten, gebruikt deze benadering een fase-domein $\Delta\Sigma$ -modulator met hoge resolutie

om de CO₂-afhankelijke thermische tijdconstante (τ_{th}) van een hot-wire transducent te meten. De tijdconstante kan worden benaderd als het product van de thermische capaciteit (C_{th}) en de thermische weerstand (R_{th}). Vanwege deze eindige thermische tijdconstante, zal het aansturen van de hete draadomvormer met periodieke warmtepulsen resulteren in fase-verschoven temperatuurvariaties $\Delta T(t)$, die worden gedigitaliseerd door de PDD Σ M, waaruit τ_{th} kan worden afgeleid. Om de gevoeligheid van de gedetecteerde faseverschuiving voor τ_{th} te maximaliseren, wordt de transducent aangedreven met $f_{drive}=1/2\pi\tau_{th}$, d.w.z. de pool van het thermische filter. In vergelijking met de eerder gepresenteerde amplitude-domein methodes heeft deze methode het belangrijke voordeel dat de absolute temperatuur- en vermogensniveaus van de transducent niet nauwkeurig hoeven te worden gestabiliseerd of gemeten. De transducent wordt gebruikt als verwarmingselement en temperatuursensor, wat de fabricage van het sensorsysteem vereenvoudigt. Bovendien maakt een nieuwe differentieel aangestuurde brugschakeling het mogelijk om de relatief kleine temperatuurinformatie te extraheren in aanwezigheid van grote stuursignalen. De gerealiseerde sensor behaalt een CO₂-resolutie van 94 ppm terwijl slechts 12 mJ per meting wordt gedissipeerd, wat de best gerapporteerde CO₂-resolutie en het laagste energieverbruik voor een CMOS CO₂-sensor vertegenwoordigt.

Hoofdstuk 6 - Conclusies

Hoofdstuk 6 vat de behaalde resultaten en de oorspronkelijke bijdragen in dit proefschrift samen. De belangrijkste bevindingen op zowel systeemniveau als circuitniveau worden besproken. Ten slotte worden enkele aanbevelingen voor toekomstig werk gepresenteerd, zoals verdere optimalisatie van de hot-wire transducenten, verdere optimalisatie van de ruisprestaties van de ratiometrische amplitude-domein uitleesmethode, integratie van een on-chip ADC voor de algoritmische uitleesmethode, en verder onderzoek naar oplossingen voor compensatie van kruisgevoeligheid en voor packaging.

SAMENVATTING

LIST OF PUBLICATIONS

Book Chapter:

Z. Cai, R. van Veldhoven, H. Suy, G. de Graaf, K.A.A. Makinwa, M.A.P. Pertijs, “CMOS-Compatible Carbon Dioxide Sensors,” in *Low-Power Analog Techniques, Sensors for Mobile Devices, and Energy Efficient Amplifiers - Advances in Analog Circuit Design (AACD) 2018*. Springer International Publishing, 2019, sec. II, pp. 199-219.

Journal Articles:

Z. Cai, R. van Veldhoven, H. Suy, G. de Graaf, K.A.A. Makinwa, M.A.P. Pertijs, “A Phase-Domain Readout Circuit for a CMOS Compatible Hot-wire CO₂ Sensor,” *IEEE Journal of Solid-State Circuits (JSSC)*, vol. 53, no. 11, pp. 3303-3313, Nov. 2018.

Z. Cai, L. Rueda Guerrero, A. Louwarse, H. Suy, R. van Veldhoven, K.A.A. Makinwa, M.A.P. Pertijs, “A CMOS Readout Circuit for Resistive Transducers Based on Algorithmic Resistance and Power Measurement,” *IEEE Sensors Journal*, volume 17, Issue 23, pp. 7917-7927, December 2017.

Z. Cai, R. van Veldhoven, A. Falepin, H. Suy, E. Sterckx, C. Bitterlich, K.A.A. Makinwa, M.A.P. Pertijs, “A Ratiometric Readout Circuit for Thermal-Conductivity-Based Resistive CO₂ Sensors,” *IEEE Journal of Solid-State Circuits (JSSC)*, volume 51, Issue 10, pp. 2453–2474, October 2016.

Conference Proceedings:

Z. Cai, R. van Veldhoven, H. Suy, G. de Graaf, K.A.A. Makinwa, M.A.P. Pertijs, “CMOS-Compatible Carbon Dioxide Sensors,” In *Proc. Workshop on Advances in Analog Circuit Design (AACD)*, April 2018. (invited paper).

Z. Cai, R. van Veldhoven, H. Suy, G. de Graaf, K.A.A. Makinwa, M.A.P. Pertijs, “A Phase-Domain Readout Circuit for a CMOS Compatible Thermal-Conductivity-Based Carbon Dioxide Sensor,” In *Dig. Techn. Papers IEEE International Solid-State Circuits Conference (ISSCC)*, pp. 332-333, February 2018.

Z. Cai, R. van Veldhoven, A. Falepin, H. Suy, E. Sterckx, C. Bitterlich, K.A.A. Makinwa, M.A.P. Pertijs, “An Integrated Carbon Dioxide Sensor for Air-Quality Monitoring,” In *Proc. Conference for ICT-Research in the Netherlands (ICT.OPEN)*, The Netherlands, March 2016.

Z. Cai, R. van Veldhoven, A. Falepin, H. Suy, E. Sterckx, K.A.A. Makinwa, M.A.P. Pertijs, “A Ratiometric Readout Circuit for Thermal-Conductivity-Based Resistive Gas Sensors,” In *Proc. European Solid-State Circuits Conference (ESSCIRC)*, pp. 275–278, September 2015.

Z. Cai, R. van Veldhoven, A. Falepin, H. Suy, E. Sterckx, K.A.A. Makinwa, M.A.P. Pertijs, “An Integrated Carbon Dioxide Sensor Based on Ratiometric Thermal-Conductivity Measurement,” In *Proc. International Conference on Solid-State Sensors, Actuators and Microsystems (TRANSDUCERS)*, pp. 622–625, June 2015.

Patent:

Z. Cai, M.A.P. Pertijs, R. van Veldhoven, K.A.A. Makinwa, “Ratiometric Device,” *United States 9835575B2*, December 2017

ACKNOWLEDGMENT

This thesis is the final outcome of my Ph.D. project at Electronic Instrumentation Laboratory of Delft University of Technology, where I spent an adventurous, fascinating and fulfilling period of about four and a half years. This was a journey full of challenges but certainly also had moments of delight. I would like to thank the people who have helped me through this journey and made it so colorful.

I would like to acknowledge and thank my two promoters, Kofi Makinwa and Michiel Pertijs. To Kofi, I sincerely thank him for his encouragement and confidence in me which began the first time we met. I have benefited and learned a lot from his keen insight on technical questions and his accurate grasp on the big picture, as well as his optimism about the future. I am so fortunate to have the opportunity to work with him. To Michiel, we have worked very closely throughout the entire process, and the experience of working with Michiel is extraordinary. He has a highly analytical mind equipped with deep insight, which made the communication between us always smooth and effortless. I enjoyed every “whiteboard discussion” with Michiel, and our discussions were always so inspiring that we frequently forgot about the time. I was always impressed by Michiel’s deep insight in circuits, which undoubtedly shaped my thoughts and approaches in circuit design. The work could not have been possible without his passionate and persistent support.

This project was supported by NXP Semiconductors, The Netherlands. I would like to thank my collaborators from NXP Semiconductors, Hilco Suy (now with ams AG), Annelies Falepin (now with IMEC), Eric Sterckx, for their support and help. Special thanks go to Robert van Veldhoven for his valuable insight and experience in the design of Delta-Sigma ADCs. I also want to thank Christian Bitterlich from ams AG, Germany, for his help in the chip measurement at the later stage of the project.

Furthermore, I would like to thank all the people in the Electronic Instrumentation Laboratory for making it such a pleasant workplace. I want to thank my former colleagues of the Pertijs group, Chao, Zhao, Mingliang, Eunchul, Douwe, Qing, Yuming, Qilong, Michele, for all the valuable discussions. My special thanks go to Zhichao and Ruimin, for their support and friendship. My gratitude also goes to other fellow researches in the EI lab, Xiaoliang, Fei, Hui,

ACKNOWLEDGMENT

Guijie, Weihan, Saleh, Ugur, Sining, Bahman, Thije, Burak, Pelin, for all the interesting discussions and help. In particular, I would like to thank Ger for the discussions about the gas sensors and measurements. I thank all the technical staff of the laboratory, especially Zu-yao and Lukasz, for helping me with the measurement setup and wire-bonding of the chips. My gratitude goes to Joyce, whose administrative support made the lab run so well.

I am grateful to the Master and Bachelor students who I had the opportunity to work with. I would like to thank Luis E. Rueda Guerrero and Alexander Louwerse, whose efforts in the design and measurement contributed to the work described in Chapter 4.

I thank my current NXP colleagues in the Personal Health group for their support and help. Special thanks to Harry Neuteboom for proofreading the Dutch-version summary of this thesis.

I want to thank my officemates and friends, in particular, Xinyu, Junfeng, Yang, Chao and Long, for sharing the ups and downs of Ph.D. student life, and for making a friendly and open environment. Thanks to my sister-in-law Ziyan for proofreading parts of the thesis. I am grateful to my parents, for their love, and for giving me great freedom to live my own life. I thank Morris (my Dutch cat) for his companionship and trust, and for all the joy and happiness he has brought to our home. Finally, I thank Zhuoling, my wife and best friend, for her unconditional love, encouragement, and understanding.

Zeyu Cai

Utrecht, December, 2019

ABOUT THE AUTHOR



Zeyu Cai received the B.Eng. degree in communication engineering from Nankai University, Tianjin, China, in 2004, and the M.Sc. degree (with distinction) in electronics from The University of Edinburgh, Edinburgh, U.K., in 2011. From 2005 to 2010, he was a Product Engineer with Qorvo, Inc., Beijing, China. From 2012 to 2017, he worked as a Ph.D. candidate in the Electronic Instrumentation Laboratory, Delft University of Technology, Delft, The Netherlands. His Ph.D. project is about next-generation carbon dioxide sensors in CMOS technology, supported by NXP Semiconductors and ams AG, The Netherlands. The research has resulted in patented work, as well as publications in a book chapter, peer-reviewed journals, and conference proceedings in both the areas of sensors and circuits.

Since 2017, he has been a Senior Analog Design Engineer with the Personal Health Group, NXP Semiconductors, Eindhoven, The Netherlands, where he designs ultra-low-power circuits for hearing instruments and IoT applications.

In his spare time, he likes watching and singing musicals. He holds a singing certificate from Complete Vocal Institute, Copenhagen, Denmark.

ABOUT THE AUTHOR